



**CENTRO DE INVESTIGACIONES  
EN OPTICA, A.C.**

**Final Version  
Includes changes suggested by reviewers**

# **“DESIGN AND CHARACTERIZATION OF WAVEGUIDES MANUFACTURED BY LASER WRITING”**



**Thesis to obtain the degree of Master in Optomechatronics**

***By: Astrid Jordana del Socorro Saldaña Sánchez***

*Advisor: Dra. Gloria Verónica Vázquez García*

*León · Guanajuato · México  
February 2025*

## Dedication

*To my mother Ma. Socorro Sánchez Calderon,  
thanks for being the best mom I could ask for.*

*“It’s like everyone tells a story about themselves inside their own head. Always. All the time. That story makes you what you are. We build ourselves out of that story.”*

Patrick Rothfuss

## Acknowledgements

I would like to acknowledge the constant support and encouragement I’ve received from my family, particularly my mother. Mom, your belief in me and your sacrifices throughout my academic journey mean the world to me. I am truly grateful for everything you’ve done, which has enabled me to pursue my dreams.

My friends, your unwavering support throughout my academic journey has been invaluable. Your understanding and encouragement have not only played an instrumental role in my personal and academic growth but have also made my journey more enjoyable. I deeply appreciate your presence in my life.

Special thanks go to Dr. David Monzón Hernández and his student Monserrat Alonso Murias. Their expertise, support, and encouragement have been crucial to the successful completion of this project.

I want to express gratitude to my thesis advisor, Dra. Gloria Verónica Vázquez García, for accepting me in her group, for her patience and for her understanding.

I am deeply grateful to CONAHCYT and CIO for giving me the tools I needed to complete my degree, especially the optics workshop people, for being such amazing people and helping me.

*“The first principle is that you must not fool yourself and you are the easiest person to fool.”*

Richard P. Feynman

## Abstract

Research into the fabrication of buried waveguides using a femtosecond laser is becoming increasingly significant for photonic devices and integrated sensor applications. This study focuses on optimizing fabrication parameters to reduce waveguide losses by aiming for the uniformity of the refractive index change in the laser-modified substrate.

The research evaluates the core-cladding refractive index change using three methods: a numerical approach (*V parameter*), the *inverse Helmholtz technique*, and an interferometric optical sensor based on *Fabry-Pérot*. Factors such as writing speed, laser energy, numerical aperture, and depth of focus are analyzed for their impact on waveguide properties. The study demonstrates the successful design, manufacturing, and characterization of femtosecond laser-written waveguides in soda-lime substrates, leveraging nonlinear absorption from high energy of the laser beam.

The best comparable results show changes in refractive index as small as  $\Delta n = 1.807 \times 10^{-3}$  and as large as  $\Delta n = 5.607 \times 10^{-3}$  for waveguides made by NA=0.40, meanwhile for the NA=0.65, we have the smallest value  $\Delta n = 1.775 \times 10^{-3}$  and the largest  $\Delta n = 5.289 \times 10^{-3}$ , both at  $50\mu m$  depth of focus,  $3\mu J$  of energy and different writing speeds. For the mentioned waveguides, we had the smallest value of propagation losses of  $5.2 dB/cm$ ,  $7.9 dB/cm$  for NA=0.40 and NA=0.65 respectively, both at  $3\mu J$  at  $50\mu m$  showing a symmetrical mode field profile, despite their elliptical physical geometry. The findings highlight the potential of these waveguides for various optical devices, laying the groundwork for the cost-effective fabrication of photonic integrated circuits that merge optical elements with electronics, presenting a valuable research opportunity in optomechatronics.

“El primer principio es que no debes engañarte a ti mismo, y eres la persona más fácil de engañar.”

Richard P. Feynman

## Resumen

La investigación sobre la fabricación de guías de onda enterradas mediante un láser de femtosegundos es cada vez más relevante en dispositivos fotónicos y aplicaciones de sensores integrados. Este estudio se centra en optimizar los parámetros de fabricación para reducir las pérdidas, evaluando la uniformidad en el cambio del índice de refracción del sustrato modificado por el láser.

Se utilizan tres métodos para evaluar el cambio en el índice de refracción: un enfoque numérico basado en el *parámetro V*, la *ecuación inversa de Helmholtz* y un sensor interferométrico de *Fabry-Pérot*. Se analizan factores como la velocidad de escritura, la energía del láser, la apertura numérica (NA) y la profundidad de enfoque. Los mejores resultados muestran cambios en el índice de refracción desde  $\Delta n = 1.807 \times 10^{-3}$  hasta  $\Delta n = 5.607 \times 10^{-3}$  para NA=0.40, y de  $\Delta n = 1.775 \times 10^{-3}$  a  $\Delta n = 5.289 \times 10^{-3}$  para NA=0.65, ambos a una profundidad de  $50 \mu m$  con  $3 \mu J$  de energía y diferentes velocidades de escritura.

Las pérdidas por propagación más bajas fueron de 5.2 dB/cm para NA=0.40 y 7.9 dB/cm para NA=0.65, mostrando un perfil de modo simétrico a pesar de la geometría elíptica de las guías. Estos hallazgos subrayan el potencial de las guías fabricadas con láser de femtosegundo para dispositivos ópticos, sentando las bases para la fabricación de circuitos fotónicos integrados que combinen elementos ópticos y electrónicos.

# Contents

<b>Dedication</b>	<b>i</b>
<b>Acknowledgements</b>	<b>ii</b>
<b>Abstract</b>	<b>iii</b>
<b>Resumen</b>	<b>iv</b>
<b>List of Acronyms</b>	<b>vii</b>
<b>List of Figures</b>	<b>ix</b>
<b>List of Tables</b>	<b>xv</b>
<b>1 Introduction</b>	<b>1</b>
1.1 Overview . . . . .	1
1.2 Background . . . . .	2
1.2.1 Waveguide configurations . . . . .	4
1.2.2 Waveguide writing techniques . . . . .	6
1.2.3 Applications . . . . .	8
1.2.4 Proposed techniques for measuring the RI of 3D waveguides . . .	9
1.3 Objectives . . . . .	10
1.3.1 General objectives . . . . .	10
1.3.2 Specific objectives . . . . .	10

## Contents

1.4	Structural outline . . . . .	11
<b>2</b>	<b>Fundamental theory of light propagation in waveguides</b>	<b>12</b>
2.1	Total internal reflection and Snell's law . . . . .	13
2.1.1	Guided modes in waveguides . . . . .	15
2.2	General wave equation . . . . .	16
2.3	Light propagation in cylindrical waveguides and their propagation modes	19
2.4	Losses in dielectric waveguides . . . . .	23
2.4.1	Efficiency due to multiple reflections . . . . .	26
2.4.2	Mode-size mismatch . . . . .	27
2.4.3	Transmission due to Fresnel reflection . . . . .	29
<b>3</b>	<b>Femtosecond-written waveguide fabrication</b>	<b>30</b>
3.1	Femtosecond direct laser writing technique . . . . .	31
3.1.1	Fundamentals of femtosecond laser writing in glass . . . . .	31
3.1.2	Laser-material interaction . . . . .	35
3.2	Fabrication methodology for buried waveguides . . . . .	39
3.2.1	Substrate preparation . . . . .	39
3.2.2	Steps for making a waveguide . . . . .	40
<b>4</b>	<b>Techniques for refractive index measurement in buried waveguides</b>	<b>45</b>
4.1	End-fire coupling techniques . . . . .	46
4.1.1	Normalized frequency in a waveguide . . . . .	46
4.1.2	Inverse Helmholtz equation . . . . .	48
4.2	Extrinsic Fabry-Pérot interferometer . . . . .	49
<b>5</b>	<b>Results and discussion</b>	<b>52</b>
5.1	Near-field mode characterization . . . . .	54
5.1.1	Experimental arrangement . . . . .	54
5.2	Mode analysis and comparison of buried waveguides . . . . .	57
5.2.1	Mode size of the waveguides . . . . .	60
5.2.2	Physical size of the cross-section of the waveguides . . . . .	64

## Contents

5.3	Core-cladding index change calculation using the normalized frequency technique . . . . .	69
5.4	Core-cladding index change calculation using the inverse Helmholtz technique . . . . .	73
5.4.1	2D Core-cladding index change distribution . . . . .	78
5.5	Core-cladding index change calculation using an interferometric sensor .	80
5.6	Comparing techniques for $\Delta n$ calculation in laser-written waveguides . .	83
5.7	Propagation losses in dielectric waveguides . . . . .	85
<b>6</b>	<b>Conclusions and perspectives</b>	<b>89</b>
6.1	Perspectives . . . . .	91
	<b>Bibliography</b>	<b>91</b>

# Acronyms

**CIO** *Optical Research Center*. vii, 31, 39

**DLW** *Direct Laser Writing*. vii, 1

**EFPI** *Extrinsic Fabry-Pérot Interferometer*. vii, xii, 10, 49–51

**EFPI** *Extrinsic Hybrid Fabry-Pérot Interferometer*. vii, 10

**FDLW** *Femtosecond Direct Laser Writing*. vii, xi, xii, 1, 2, 4–6, 8, 10, 12, 31–33, 43, 52, 85, 91

**FPI** *Fabry-Pérot Interferometer*. vii, 49

**HAZ** *Heat-Affected Zone*. vii, 33

**IFPI** *Intrinsic Fabry-Pérot Interferometer*. vii, xii, 49, 51

**LASER** *Light Amplification by Stimulated Emission of Radiation*. vii, 2

**LOU** *Ultrafast Optics Laboratory*. vii, 31

**MCF** *Multicore Fiber*. vii, 10, 50, 80, 82

**MO** *Microscope Objective*. vii, xii, 7, 40, 41, 54, 55

**NA** *Numerical Aperture*. vii, x, 7, 10, 14, 15, 31, 37, 42, 68, 73, 78, 84

## Acronyms

**NF** *Near Field.* vii, 48

**NIR** *Near Infrared.* vii, 1

**OPL** *Optical Path Length.* vii, 10, 15

**RI** *Refractive Index.* v, vii, 2, 3, 9–11, 29, 38, 46–50, 52, 70, 77, 80, 81, 85

**SMF** *Single Mode Fiber.* vii, 10, 50, 54, 80, 82

**STEs** *Self-trapped excitons.* vii

**TE** *Transverse-Electric.* vii, 16

**TIR** *Total Internal Reflection.* vii, x, 14, 19

**TM** *Transverse-Magnetic.* vii, 16

## List of Figures

1.1	<i>Scheme of an optical waveguide.</i> . . . . .	3
1.2	<i>Basic waveguide structures (a) planar and (b) circular. In red we emphasize the waveguide from the substrate that is represented in white [1].</i>	4
1.3	<i>Types of rectangular (channel) waveguides (a) ridge, (b) embedded and (c) buried. The waveguide is the red part, and substrate is in white.</i> . . . .	4
1.4	<i>Illustration of the cross-section of the types of waveguide configuration depending on their fabrication. The dashed blue lines indicate the spatial locations of the core corresponding to the waveguide, and the more obscure circles indicate the ablated part. (a) Type I, (b) Type II, (c) Type III and (d) Type IV.</i> . . . . .	6
1.5	<i>(a) Transverse and (b) longitudinal writing geometries for femtosecond laser writing waveguide fabrication in bulk transparent materials. The arrows indicate the substrate movement direction.</i> . . . . .	7
2.1	<i>Diagram illustrating the various paths that light can take at the air-glass boundary, with the blue section representing glass and the white section representing air.</i> . . . . .	13
2.2	<i>Representation of a ray of light traveling through a waveguide to illustrate the TIR, the critical angle, its relationship with the NA (<math>\theta_{max}</math>) and the formation of evanescent waves by the refracted rays.</i> . . . . .	14

List of Figures

2.3	<i>Modes of a waveguide. The field patterns are shown correspondingly: Orange is the fundamental mode (<math>m=0</math>), blue is the guided first high-order mode (<math>m=1</math>) and green the second high-order mode (<math>m=2</math>). . . . .</i>	16
2.4	<i>Exemplification of the relationship between <math>\mathbf{E}</math> and <math>\mathbf{H}</math> in a plane wave. . .</i>	17
2.5	<i>Nomenclature and step index representation of a buried cylindrical waveguide, where <math>a</math> is the core radius, <math>n_0</math> the refractive index at the core, and <math>n_1</math> is the refractive index of the medium (substrate). . . . .</i>	20
2.6	<i>Typical distribution of waveguide mode profiles in a transverse propagation.</i>	28
3.1	<i>Diagram of the experimental setup for the FDLW technique. . . . .</i>	32
3.2	<i>Picture of the <math>\mu</math>FAB microfabrication workstation. . . . .</i>	32
3.3	<i>Excitation multiphoton process of electrons in bandgap materials through multiple photons [2]. . . . .</i>	34
3.4	<i>Illustration of the internal modification within the transparent substrate caused by femtosecond laser irradiation through multiphoton absorption.</i>	35
3.5	<i>Representation example of spatial distribution of the laser energy absorbed by transparent materials; One-photon (blue), two-photon (orange), and three-photon (yellow). The green line indicates the required value to exceed in order to induce changes within the glass (3.5e.V for soda-lime).</i>	36
3.6	<i>Nonlinear photoionization processes in glass by femtosecond laser irradiation. (a) Multiphoton absorption, (b) avalanche ionization, made by free carrier absorption, followed by (c) impact ionization or the continuity of avalanche ionization. . . . .</i>	37
3.7	<i>Depiction of the morphological changes produced by femtosecond laser irradiation: (a) When the laser is exposed to a femtosecond laser, there is a (b) nonlinear absorption leading to the creation of a free electron plasma through multiphoton ionization. This process is followed by an avalanche photoionization, resulting in the formation of a (c) hot electron plasma (d) leading to three distinct types of permanent modification. . .</i>	38

List of Figures

3.8	<i>Example of fabrication of buried waveguides. The darker zones indicate the negative <math>\Delta n</math> contrast and the bright zone indicates the positive <math>\Delta n</math> contrast (waveguide).</i>	39
3.9	<i>Picture of the focus of the MO on the surface of the substrate.</i>	41
3.10	<i>Image of the steps described to find the top edge.</i>	41
3.11	<i>Image of the steps described to find the bottom edge.</i>	42
3.12	<i>Example of the location of the P0, P1, P2 points.</i>	42
3.13	<i>Illustration of the technique known as femtosecond laser writing (FDLW) for fabricating optical buried waveguides. The diagram includes variables such as a, which represents the separation between waveguides, b, which denotes the distance from each set of three waveguides, and d, which indicates the distance from the top surface.</i>	43
3.14	<i>Substrates employed in the fabrication of waveguide arrays positioned below the surface. (a) NA=0.40 and (b) NA=0.65.</i>	44
4.1	<i>The diagram illustrates the operation of four types of fibre optics interferometers: (a) Intrinsic Fabry-Pérot Interferometer, (b) Extrinsic Fabry-Pérot Interferometer with one cavity, (c) EFPI with two cavities, (d) Extrinsic hybrid Fabry-Pérot interferometer.</i>	51
5.1	<i>Experimental setup for the analysis of the optical characteristics of buried waveguides.</i>	55
5.2	<i>Example of the alignment of the optical fibre with chosen waveguide through the surface reference.</i>	56
5.3	<i>Modes of the buried waveguides at a depth=50<math>\mu</math>m with an energy=2<math>\mu</math>J and NA=0.40.</i>	58
5.4	<i>Modes of the buried waveguides at a depth=150<math>\mu</math>m with an energy=2<math>\mu</math>J and NA=0.40.</i>	58
5.5	<i>Modes of the buried waveguides at a depth=250<math>\mu</math>m with an energy=2<math>\mu</math>J and NA=0.40.</i>	58

List of Figures

5.6	<i>Modes of the buried waveguides at a depth=50<math>\mu</math>m with an energy=3<math>\mu</math>J and NA=0.40. . . . .</i>	59
5.7	<i>Modes of the buried waveguides at a depth=150<math>\mu</math>m with an energy=3<math>\mu</math>J and NA=0.40. . . . .</i>	59
5.8	<i>Modes of the buried waveguides at a depth=250<math>\mu</math>m with an energy=3<math>\mu</math>J and NA=0.40. . . . .</i>	59
5.9	<i>Modes of the buried waveguides at a depth=50<math>\mu</math>m with an energy=2<math>\mu</math>J and NA=0.65. . . . .</i>	59
5.10	<i>Modes of the buried waveguides at a depth=50<math>\mu</math>m with an energy=3<math>\mu</math>J and NA=0.65. . . . .</i>	59
5.11	<i>Average mode field radius (a) horizontal (<math>\omega_x</math> [<math>\mu</math>m]) and (b) vertical (<math>\omega_y</math> [<math>\mu</math>m]) of the waveguides fabricated at 50<math>\mu</math>m, 150<math>\mu</math>m and 250<math>\mu</math>m within the substrate, NA=0.40 at energy=2<math>\mu</math>J. . . . .</i>	63
5.12	<i>Average mode field radius (a) horizontal (<math>\omega_x</math> [<math>\mu</math>m]) and (b) vertical (<math>\omega_y</math> [<math>\mu</math>m]) of the waveguides fabricated at 50<math>\mu</math>m, 150<math>\mu</math>m and 250<math>\mu</math>m within the substrate, NA=0.40 at energy=3<math>\mu</math>J. . . . .</i>	63
5.13	<i>Average mode field radius of the waveguides horizontal (<math>\omega_x</math> [<math>\mu</math>m]) and vertical (<math>\omega_y</math> [<math>\mu</math>m]) fabricated at 50<math>\mu</math>m within the substrate, NA=0.65 at energies of (a) 2<math>\mu</math>J and (b) 3<math>\mu</math>J. . . . .</i>	64
5.14	<i>Cross-sections obtained from the waveguides made by NA=0.40, (a) energy=2<math>\mu</math>J, (b) energy=3<math>\mu</math>J. . . . .</i>	64
5.15	<i>Cross-section images of the cross-sections of waveguides made by NA=0.65 and energy=2<math>\mu</math>J. . . . .</i>	65
5.16	<i>Cross-section images of the cross-sections of waveguides made by NA=0.65 and energy=3<math>\mu</math>J. . . . .</i>	65
5.17	<i>Physical average size of the cross-section of the waveguides fabricated at 50<math>\mu</math>m, 150<math>\mu</math>m and 250<math>\mu</math>m within the substrate, NA=0.40 at energy=2<math>\mu</math>J, (a) horizontal radius (<math>r_x</math> [<math>\mu</math>m]), (b) vertical radius (<math>r_y</math> [<math>\mu</math>m]). . . . .</i>	68

List of Figures

5.18	<i>Comparison of the physical size of waveguides fabricated at <math>50\mu\text{m}</math>, <math>150\mu\text{m}</math> and <math>250\mu\text{m}</math> within the substrate, for <math>NA=0.40</math> at energy=<math>3\mu\text{J}</math>, (a) horizontal radius (<math>r_x</math> [<math>\mu\text{m}</math>]), (b) vertical radius (<math>r_y</math> [<math>\mu\text{m}</math>]). . . . .</i>	69
5.19	<i>Comparison of the physical average horizontal radius (<math>r_x</math> [<math>\mu\text{m}</math>]) and vertical radius (<math>r_y</math> [<math>\mu\text{m}</math>]), of waveguides fabricated at <math>50\mu\text{m}</math> within the substrate, for <math>NA=0.65</math>, (a) energy=<math>2\mu\text{J}</math>, (b) energy=<math>3\mu\text{J}</math>. . . . .</i>	69
5.20	<i>Comparison of <math>\Delta n</math> at different energies of fabrication, <math>NA=0.40</math> and depth of focus (a) <math>50\mu\text{m}</math>, (b) <math>150\mu\text{m}</math> and (c) <math>250\mu\text{m}</math>. . . . .</i>	72
5.21	<i>Comparison of <math>\Delta n</math> for different energies of fabrication at <math>NA=0.65</math> and depth=<math>50\mu\text{m}</math>. . . . .</i>	72
5.22	<i>(a), (c), (e) Core-cladding index contrast (<math>\Delta n</math>) and (b), (d), (f) refractive index profiles for <math>NA=0.40</math> at an energy of <math>2\mu\text{J}</math>, with depths of focus of <math>50\mu\text{m}</math>, <math>150\mu\text{m}</math>, and <math>250\mu\text{m}</math>. . . . .</i>	75
5.23	<i>(a), (c), (e) Core-cladding index contrast (<math>\Delta n</math>) and (b), (d), (f) refractive index profiles for <math>NA=0.40</math> at an energy of <math>3\mu\text{J}</math>, with depths of focus of <math>50\mu\text{m}</math>, <math>150\mu\text{m}</math>, and <math>250\mu\text{m}</math>. . . . .</i>	76
5.24	<i>(a), (c) Core-cladding index contrast (<math>\Delta n</math>) and (b), (d) refractive index profiles for <math>NA=0.65</math>, with depths of focus of <math>50\mu\text{m}</math> and energies of <math>2\mu\text{J}</math> and <math>3\mu\text{J}</math>. . . . .</i>	77
5.25	<i>2D index profile (<math>\Delta n</math>) of the waveguides at depth=<math>50\mu\text{m}</math>, energy=<math>2\mu\text{J}</math>, with <math>NA=0.40</math>. . . . .</i>	78
5.26	<i>2D index profile (<math>\Delta n</math>) of the waveguides at depth=<math>150\mu\text{m}</math>, energy=<math>2\mu\text{J}</math>, with <math>NA=0.40</math>. . . . .</i>	78
5.27	<i>2D index profile (<math>\Delta n</math>) of the waveguides at depth=<math>250\mu\text{m}</math>, energy=<math>2\mu\text{J}</math>, with <math>NA=0.40</math>. . . . .</i>	79
5.28	<i>2D index profile (<math>\Delta n</math>) of the waveguides at depth=<math>50\mu\text{m}</math>, energy=<math>3\mu\text{J}</math>, with <math>NA=0.40</math>. . . . .</i>	79
5.29	<i>2D index profile (<math>\Delta n</math>) of the waveguides at depth=<math>150\mu\text{m}</math>, energy=<math>3\mu\text{J}</math>, with <math>NA=0.40</math>. . . . .</i>	79

List of Figures

5.30	<i>2D index profile (<math>\Delta n</math>) of the waveguides at depth=250<math>\mu\text{m}</math>, energy=3<math>\mu\text{J}</math>, with NA=0.40. . . . .</i>	79
5.31	<i>2D index profile (<math>\Delta n</math>) of the waveguides at depth=50<math>\mu\text{m}</math>, energy=2<math>\mu\text{J}</math>, with NA=0.65. . . . .</i>	79
5.32	<i>2D index profile (<math>\Delta n</math>) of the waveguides at depth=50<math>\mu\text{m}</math>, energy=3<math>\mu\text{J}</math>, with NA=0.65. . . . .</i>	80
5.33	<i>Core-cladding index contrast for a NA=0.40 and energy=3<math>\mu\text{J}</math>. Measured by (a) SMF, (b) MCF. . . . .</i>	82
5.34	<i>Core-cladding index contrast for a NA=0.65 and energy=3<math>\mu\text{J}</math>. Measured by (a) SMF, (b) MCF. . . . .</i>	83
5.35	<i>Propagation losses (<math>\alpha</math> [dB/cm]) for different energy levels with NA=0.40, (a) energy=2<math>\mu\text{J}</math>, (b) energy=3<math>\mu\text{J}</math>. . . . .</i>	87
5.36	<i>Propagation losses (<math>\alpha</math> [dB/cm]) for different energy levels with NA=0.65, (a) energy=2<math>\mu\text{J}</math>, (b) energy=3<math>\mu\text{J}</math>. . . . .</i>	88

## List of Tables

1.1	<i>Values of <math>\Delta n</math> achieved in different crystals [3] [4]. . . . .</i>	8
5.1	<i>Average horizontal mode field radius (<math>\omega_x</math> [<math>\mu\text{m}</math>]), <math>NA=0.40</math>, energy=<math>2\mu\text{J}</math> . . . . .</i>	61
5.2	<i>Average vertical mode field radius (<math>\omega_y</math> [<math>\mu\text{m}</math>]), <math>NA=0.40</math>, energy=<math>2\mu\text{J}</math>. . . . .</i>	61
5.3	<i>Average horizontal mode field radius (<math>\omega_x</math> [<math>\mu\text{m}</math>]), <math>NA=0.65</math>, energy=<math>2\mu\text{J}</math>. . . . .</i>	61
5.4	<i>Average vertical mode field radius (<math>\omega_y</math> [<math>\mu\text{m}</math>]), <math>NA=0.65</math>, energy=<math>2\mu\text{J}</math>. . . . .</i>	61
5.5	<i>Average horizontal mode field radius (<math>\omega_x</math> [<math>\mu\text{m}</math>]), <math>NA=0.40</math>, energy=<math>3\mu\text{J}</math> . . . . .</i>	62
5.6	<i>Average vertical mode field radius (<math>\omega_y</math> [<math>\mu\text{m}</math>]), <math>NA=0.40</math>, energy=<math>3\mu\text{J}</math>. . . . .</i>	62
5.7	<i>Average horizontal mode field radius (<math>\omega_x</math> [<math>\mu\text{m}</math>]), <math>NA=0.65</math>, energy=<math>3\mu\text{J}</math>. . . . .</i>	62
5.8	<i>Average vertical mode field radius (<math>\omega_y</math> [<math>\mu\text{m}</math>]), <math>NA=0.65</math>, energy=<math>3\mu\text{J}</math>. . . . .</i>	62
5.9	<i>Physical average radius (<math>r_x</math> [<math>\mu\text{m}</math>]), <math>NA=0.40</math>, energy=<math>2\mu\text{J}</math>. . . . .</i>	66
5.10	<i>Physical average radius (<math>r_y</math> [<math>\mu\text{m}</math>]), <math>NA=0.40</math>, energy=<math>2\mu\text{J}</math>. . . . .</i>	66
5.11	<i>Physical average radius (<math>r_x</math> [<math>\mu\text{m}</math>]), <math>NA=0.65</math>, energy=<math>2\mu\text{J}</math>. . . . .</i>	66
5.12	<i>Physical average radius (<math>r_y</math> [<math>\mu\text{m}</math>]), <math>NA=0.65</math>, energy=<math>2\mu\text{J}</math>. . . . .</i>	66
5.13	<i>Physical average radius (<math>r_x</math> [<math>\mu\text{m}</math>]), <math>NA=0.40</math>, energy=<math>3\mu\text{J}</math>. . . . .</i>	67
5.14	<i>Physical average radius (<math>r_y</math> [<math>\mu\text{m}</math>]), <math>NA=0.40</math>, energy=<math>3\mu\text{J}</math>. . . . .</i>	67
5.15	<i>Physical average radius (<math>r_x</math> [<math>\mu\text{m}</math>]), <math>NA=0.65</math>, energy=<math>3\mu\text{J}</math>. . . . .</i>	67
5.16	<i>Physical average radius (<math>r_y</math> [<math>\mu\text{m}</math>]), <math>NA=0.65</math>, energy=<math>3\mu\text{J}</math>. . . . .</i>	67
5.17	<i>Calculated values of <math>\Delta n</math> obtained for <math>NA=0.40</math> at an energy of <math>2\mu\text{J}</math> using the <math>V</math> parameter technique. The values of <math>\Delta n</math> are on a scale of <math>\times 10^{-3}</math>. . . . .</i>	70
5.18	<i>Calculated values of <math>\Delta n</math> obtained for <math>NA=0.40</math> at an energy of <math>3\mu\text{J}</math> using the <math>V</math> parameter technique. The values of <math>\Delta n</math> are on a scale of <math>\times 10^{-3}</math>. . . . .</i>	71

List of Tables

5.19	<i>Calculated values of <math>\Delta n</math> obtained for <math>NA=0.65</math> at the depth of focus <math>50\mu m</math> using the <math>V</math> parameter technique. The values of <math>\Delta n</math> are on a scale of <math>\times 10^{-3}</math>.</i>	71
5.20	<i>Calculated values of <math>\Delta n</math> obtained for <math>NA=0.40</math> at an energy of <math>2\mu J</math> using the Helmholtz technique. The values of <math>\Delta n</math> are on a scale of <math>\times 10^{-3}</math>.</i>	74
5.21	<i>Calculated values of <math>\Delta n</math> obtained for <math>NA=0.40</math> at an energy of <math>3\mu J</math> using the Helmholtz technique. The values of <math>\Delta n</math> are on a scale of <math>\times 10^{-3}</math>.</i>	74
5.22	<i>Calculated values of <math>\Delta n</math> obtained for <math>NA=0.65</math> at the depth of focus <math>50\mu m</math> using the Helmholtz technique. The values of <math>\Delta n</math> are on a scale of <math>\times 10^{-3}</math>.</i>	74
5.23	<i>Refractive index of the core obtained with SMF and MCF for <math>50\mu m</math> of depth at <math>NA=0.40</math> and energy=<math>3\mu J</math>.</i>	80
5.24	<i>Refractive index of the core obtained with SMF and MCF for <math>50\mu m</math> of depth at <math>NA=0.65</math> and energy=<math>3\mu J</math>.</i>	81
5.25	<i>Average refractive index values of the cladding at different positions measured from the location of the buried waveguide.</i>	81
5.26	<i>Calculated values of the core-cladding change (<math>\Delta n</math>) obtained for <math>NA=0.40</math> at an energy of <math>3\mu J</math> and depth of focus <math>50\mu m</math> using the interferometric technique with different values of cladding. The values of <math>\Delta n</math> are on a scale of <math>\times 10^{-3}</math>.</i>	81
5.27	<i>Calculated values of the core-cladding change (<math>\Delta n</math>) obtained for <math>NA=0.65</math> at an energy of <math>3\mu J</math> and depth of focus <math>50\mu m</math> using the interferometric technique with different values of cladding. The values of <math>\Delta n</math> are on a scale of <math>\times 10^{-3}</math>.</i>	81
5.28	<i>Comparison of the values of the index contrast (<math>\Delta n</math>) for the three techniques at a depth of focus of <math>50\mu m</math>, with an energy of <math>3\mu J</math>, and <math>NA=0.40</math>. Interferometer values for <math>MCF_{40\mu m}</math>.</i>	84
5.29	<i>Comparison of the values of the index contrast (<math>\Delta n</math>) from three techniques at a depth of focus of <math>50\mu m</math>, with an energy of <math>3\mu J</math>, and <math>NA=0.65</math>. Interferometer values for <math>MCF_{40\mu m}</math>.</i>	84

List of Tables

5.30	<i>Propagation losses (<math>\alpha</math> [dB/cm]) at an energy level of <math>2\mu\text{J}</math> for a <math>NA=0.40</math>.</i>	86
5.31	<i>Propagation losses (<math>\alpha</math> [dB/cm]) at an energy level of <math>3\mu\text{J}</math> for a <math>NA=0.40</math>.</i>	86
5.32	<i>Propagation losses (<math>\alpha</math> [dB/cm]) at <math>2\mu\text{J}</math> for <math>NA=0.65</math>. . . . .</i>	87
5.33	<i>Propagation losses (<math>\alpha</math> [dB/cm]) at <math>3\mu\text{J}</math> for <math>NA=0.65</math>. . . . .</i>	87

*“My dear, here we must run as fast as we can, just to stay in place. And if you wish to go anywhere you must run twice as fast as that.”*

Lewis Carroll, *Alice in Wonderland*

# 1

## Introduction

### 1.1 Overview

Femtosecond laser micromachining, also known as *Femtosecond Direct Laser Writing* (FDLW), has been widely used to fabricate photonic structures and devices since its first demonstration in 1996. This technique utilizes ultra-short *Near Infrared* (NIR) laser pulses that change the optical properties of a material by choosing suitable irradiation conditions that do not cause microfractures or damage (thermal or stress-induced) [5,6]. With DLW, we can produce optical waveguides or more complicated photonic devices such as splitters [7], interferometers [8], Bragg gratings, polarization control elements, frequency converters, among other components [9].

Optical waveguides are the fundamental components that support light propagation within a substrate and are composed of high-index cores surrounded by low-index

layers. The *refractive index profile* is a crucial parameter to determine its performance and to measure propagation losses, propagating modes, and bandwidth [10]. Thus, an accurate measurement of the refractive index profile in an optical waveguide is relevant for designing and optimizing an optical device structure. This research project aims to fabricate buried elliptical waveguides on soda-lime glass with the FDLW technique. The objective is to measure the *Refractive Index* (RI) of the core and cladding of the fabricated waveguides using different approaches to obtain the core-cladding index change at the centre of the formed waveguide and its index profile.

This chapter will first present a brief discussion of the history of the FDLW technique used to fabricate three-dimensional buried waveguides and their relation to integrated photonics. Then, we shall briefly discuss near-field techniques and the extrinsic Fabry-Pérot, an interferometer technique for measuring the refractive index on the buried waveguides. At this point, we will present the general and specific objectives of this thesis. We will then discuss the importance of this study and its restrictions. Lastly, we will provide a schematic overview of this thesis.

## 1.2 Background

Optics is a branch of physics that studies the generation and detection of light and its interaction with matter [11]. The first major invention in modern optics was the *Light Amplification by Stimulated Emission of Radiation* (LASER) by T.H. Maiman in 1960, creating the first working laser that uses infrared light; with this advancement, we began to have access to coherent light sources [12]. Later, in 1996, Hirao et al. demonstrated that tightly focused femtosecond laser pulses could permanently modify the optical properties of a small irradiated area within the bulk of a transparent substrate [13]. Since then, many researchers have been interested in exploring the unique capabilities of lasers for microfabrication.

FDLW is a fabrication technique that has some clear advantages over others, such as:

- **Direct and maskless fabrication.** This can be achieved because the substrate

moves on an XYZ platform while the light is irradiated [14].

- **Highly flexible technique.** It can be used in almost any transparent material (glass, crystals, plastic). Furthermore, laser irradiation parameters can be tailored to achieve a suitable RI for fabricating a specific photonic structure [14].
- **Three-dimensional technique.** We can decide the depth of the photonic structure within the substrate (z-axis). This can only be achieved with this technique, adding one degree of freedom to fabrication and permitting the development of unique and innovative device architectures. This advantage can be used to sense a substance that can be put on the top of the sensing device [14].

Optical waveguides are the most fundamental components used to guide light. We can define them as a spatially inhomogeneous restricting region where light can propagate [15]. Typically, a waveguide has a core region with an increased refractive index compared to its surroundings, forming the structure shown in Fig. 1.1.



*Figure 1.1: Scheme of an optical waveguide.*

Common types of optical waveguides encompass fiber optic waveguides and transparent dielectric materials. The latter can be categorized based on various geometries, including rectangular/channel, buried/immersed, planar/slab, circular, and strip configurations, as illustrated in Fig. 1.2 and 1.3. These classifications are crucial for understanding the diverse applications and fundamental principles governing the propagation of light within these structures.

Waveguides can also be classified according to: their mode structure (mono-mode or multi-mode), refractive index profile (step or gradient profile), and substrate material used (dielectric or semiconductor).

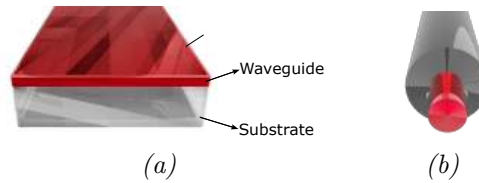


Figure 1.2: Basic waveguide structures (a) planar and (b) circular. In red we emphasize the waveguide from the substrate that is represented in white [1].

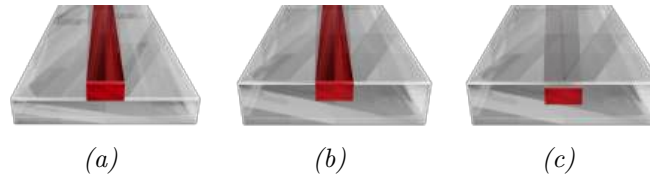


Figure 1.3: Types of rectangular (channel) waveguides (a) ridge, (b) embedded and (c) buried. The waveguide is the red part, and substrate is in white.

In order to comprehend the mode structure and refractive index profile classification, we must gain an understanding of how light is transmitted through a waveguide. This will be explored in depth in Chapter 2.

### 1.2.1 Waveguide configurations

FDLW optical waveguides can be classified depending on the induced refractive index changes in the laser-irradiated regions as follows:

- **Type I *Directly written waveguides.***

See Fig. 1.4a.

The fs laser-induced tracks are situated within a transparent material. In this configuration, the femtosecond laser induces a positive refractive index change ( $\Delta n > 0$ ) inside the focal volume, which serves as the waveguide core. This change is common in amorphous materials (glasses). In crystals, the increase of  $\Delta n$  only exists along a particular axis, supporting only guidance along one particular polarization. They are usually not stable and can be removed entirely by being exposed to high temperatures, reducing their applications. However, Type I structures are the easiest to fabricate with FDLW, and most bulk features can be preserved to an acceptable level [16].

- **Type II *Stress-induced waveguides.***

See Fig. 1.4b.

Stress-induced waveguides are located in the adjacent regions of the fs laser-induced tracks in dielectric materials. In this scheme, FDLW will induce a negative change in the refractive index ( $\Delta n < 0$ ) in the region directly irradiated, causing an expansion of the lattices in the focal volume. This expansion in the local region (core) creates a decrease in the refractive index, producing a relatively high index in the surrounding regions through the stress-induced effects. Type II waveguides are located in regions between highly damaged tracks, which means that bulk features in the waveguides may not be significantly affected. Because it is a well-understood mechanism, index changes are more easily controlled. The stress-induced waveguides are still very stable at high temperatures [16].

- **Type III *Depressed cladding waveguides.***

See Fig. 1.4c.

A depressed cladding waveguide consists of a core surrounded by a number of low-index tracks. These tracks are close to each other, constructing a quasi-continuous low-index barrier wall, which allows the confinement of the light field inside. Theoretically, any geometry can be formed by arranging the tracks at the waveguide cross-section. In practice, however, a circular shape is preferred because of its compatibility with the shape of optical fibers. The diameter of the cladding waveguides is typically  $30\mu m$  to  $150\mu m$ , separated by  $3 - 4\mu m$ . The flexible diameter of the waveguide cores enables the guidance from single-mode to highly multimode and from visible light to mid-IR wavelength regions. Type III structures are ideal platforms for unpolarized pumping as light sources [16].

- **Type IV *Ablated ridge waveguides.***

See Fig. 1.4d.

Ablated ridge waveguides are formed by high-intensity pulses of the fs laser that etch the selected region through an ultra-fast ablation mechanism. The guidance of the ablated ridge waveguides depends on the planar waveguide substrates.

A downside of Type IV ridge waveguides are the rough sidewalls produced by FDLW, which induce considerable losses and degrade waveguide quality. This quality can be improved by a postablation treatment (such as ion beam sputtering) that can be performed to reduce the roughness of the air gaps ablated [16].

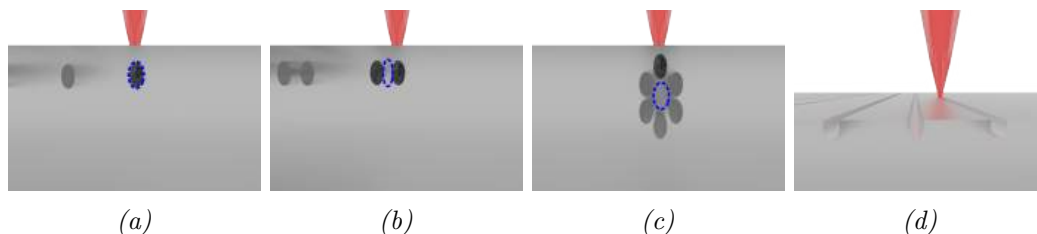


Figure 1.4: Illustration of the cross-section of the types of waveguide configuration depending on their fabrication. The dashed blue lines indicate the spatial locations of the core corresponding to the waveguide, and the more obscure circles indicate the ablated part. (a) Type I, (b) Type II, (c) Type III and (d) Type IV.

Generally, the waveguides created using the FDLW technique have minimal volumes, in which the light intensities reach high levels because of the tight confinement of the light fields in the refractive index changed area within the substrate. Benefiting from the compact geometry of the structures, the functional guiding devices can be manufactured on chip-scale wafers, in which integrated photonic circuits can be manufactured for various applications [16].

### 1.2.2 Waveguide writing techniques

The fabrication methods of a waveguide on a transparent bulk substrate can generally be divided into two: *longitudinal* and *transverse* (see Fig. 1.5).

Integrated optical devices are fabricated by scanning with the irradiation of a femtosecond laser beam through the material to create a structure of a continuous densified zone. Typically, the laser beam is stationary, and a translation stage is used to displace the sample [3].

In *longitudinal writing*, the sample is translated along the writing beam propagation direction. The advantage of this method is that the resulting waveguide structure has a cylindrical symmetric cross-section, and the transverse size is determined by the focal-

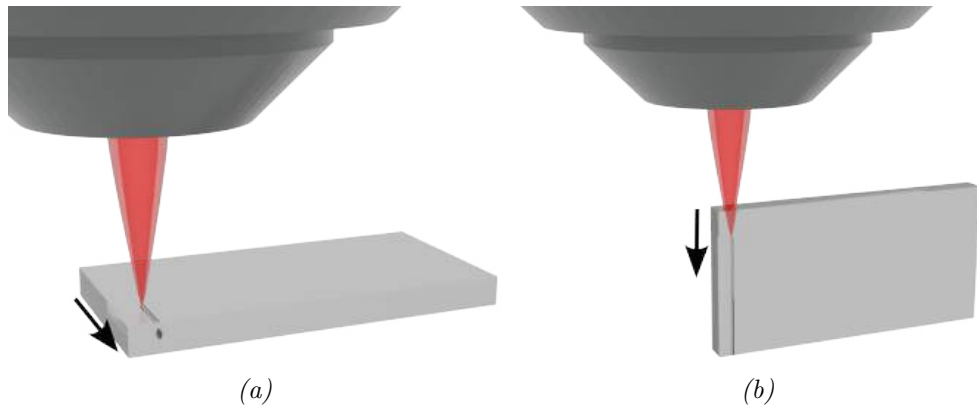


Figure 1.5: (a) Transverse and (b) longitudinal writing geometries for femtosecond laser writing waveguide fabrication in bulk transparent materials. The arrows indicate the substrate movement direction.

spot size of the objective lens that is used to concentrate the laser light. However, this means that the writing depth is limited by the working distance of the focusing lens of the MO and the spherical aberrations, which distort the focal shape. Thus, waveguides can only be a few millimeters long and the technique allows fabrication only of a straight waveguide [3], [4].

In *transverse writing*, the sample is translated perpendicular to the direction of propagation of the writing beam. Thus, the length of the waveguide is no longer restricted by the working distance of the objective lens. However, the waveguide profile takes an asymmetric droplet-like shape called here as elliptical. This writing geometry allows for the fabrication of more complex structures. The reason for this asymmetry is that for a Gaussian profile writing beam, the depth of focus ( $2z_r$ ) is greater than the spot size ( $2\omega_0$ ) by a factor  $\frac{2z_r}{2\omega_0} = \frac{n}{NA}$ , where  $n$  is the refractive index of the medium and  $NA$  is the *Numerical Aperture* of the lens. It is worth adding that this technique enables the demonstration of laser-written waveguides with the lowest propagation losses at the cost of prolonged fabrication. There are alternative solutions to the asymmetry. The basic one is to pre-modify the laser beam in such a way that the depth of focus and spot size would be the same size. This can be achieved by reshaping the incident beam and controlling the amplitude or phase. Another solution is to implement a femtosecond laser operating at hundreds of kilohertz or megahertz repetition rates. The train of laser

Material	Type I $\Delta n$	Type II $\Delta n$
<i>LiNbO<sub>3</sub></i>	$\Delta n < 1 \times 10^{-3}$	$(2 - 4) \times 10^{-3}$
<i>Nd : GGG</i>	$1.9 \times 10^{-3}$	$6 \times 10^{-4}$
<i>Silicon</i>	$(1.4 - 2.1) \times 10^{-3}$	-

Table 1.1: Values of  $\Delta n$  achieved in different crystals [3] [4].

pulses at a high repetition rate leads to heat accumulation and melting of the material. The spherically symmetric heat-affected zone induced by accumulated heat helps to correct the asymmetry of the waveguides. It has been found that the heat-affected zone can also be controlled by ambient temperature. In glasses, the modified area can be split into two regions: the inner modified region, where the temperature exceeds the forming temperature of the glass, and the outer region, where the temperature is close to the glass transformation temperature. Thus, the thermal modification mechanism includes not only the melting but also the softening of glass [3] [4].

### 1.2.3 Applications

Recently, FDLW techniques oriented to integrated optics applications are made using crystalline materials because they have fewer impurities than glass. Table 1.1 compares the  $\Delta n$  obtained by the Type I and Type II waveguides for different crystals. The index profile obtained for each waveguide depends on the material and the parameters set in the fabrication process. Because of this, the change in index obtained is difficult to compare with other materials for the FDLW. However, we can notice that the  $\Delta n$  reported is maintained in the order of  $10^{-3}$  for Type I waveguides and reaches  $10^{-4}$  for Type II waveguides, the same order of magnitude as the waveguides that we created (Type I, waveguides on soda lime).

Waveguides fabricated by femtosecond laser micromachining can be used in a variety of technical areas in photonics. Some examples are as follows [16]:

- **Electro-optic modulators**

Electro-optic modulators can be used to modulate signal parameters such as phase, intensity, and polarization. They are mainly created with Type II structures.

- **Frequency converters**

The conversion efficiency depends on the nonlinear bulk features and the guiding properties of the structures. Frequency doubling has been achieved in all four configurations from Type I to Type IV structures.

- **Waveguide lasers**

Waveguide lasers possess lower lasing thresholds, comparable efficiencies, and compact geometries compared to bulk lasers. Fabricated recently in Type III structures, but they are also extensively known in Type II configuration.

#### 1.2.4 Proposed techniques for measuring the RI of 3D waveguides

The main characteristics of an optical waveguide, such as bandwidth, mode propagation conditions and propagation losses, are intrinsically related to their *Refractive Index* profile. Therefore, it is essential to establish an efficient and accurate method for measuring and finding its relationship with the fabrication process parameters.

Next, we will briefly present the techniques used in the present work to estimate the RI on a buried waveguide.

##### **Near-field mode techniques**

Two of the techniques use the transmitted beam on a near-field condition: inverse Helmholtz equation and the normal frequency (V parameter). Based on the measurement of the intensity of the transmitted beam near the output guide facet, the RI and the index profile distribution can be calculated.

The inverse Helmholtz technique has high frequency noise in the measured intensity profile, making complicated to calculate the refractive index profile from the intensity data. To achieve this, we required a digital filter to smooth the measured intensity profile, but this provides a solution with a loss of accuracy.

The normal frequency (V parameter) technique introduces errors due to the two input values required. Suppose these values are incorrect, meaning their relationship does not correspond to a single-mode waveguide. In that case, we will not obtain a

valid value of the relation between the mode size and waveguide size, meaning that we will not be able to calculate a  $\Delta n$  value.

### **Fabry-Pérot technique**

The extrinsic Fabry-Pérot interferometer with two cavities, used to calculate the RI of the buried waveguides, was based on a *Single Mode Fiber* (SMF) (*Extrinsic Fabry-Pérot Interferometer*) and a *Multicore Fiber* (MCF) (*Extrinsic Hybrid Fabry-Pérot Interferometer*). The choice of the MCF was due to its larger core, allowing for greater light collection. This technique relies on the interference of two cavities formed by the air gap (cavity one) and substrate (cavity two) interfaces, generating a signal that could be translated into the frequency domain. By knowing the *Optical Path Length* (OPL) of light in the second cavity and the length of the substrate, the refractive index can be determined.

These techniques will be explained deeply in chapter 4.

## **1.3 Objectives**

### **1.3.1 General objectives**

1. Determine the physical and optical characteristics of waveguides fabricated with femtosecond laser writing for implementation on photonic devices.
2. Develop a standardized procedure to fabricate repeatable waveguides.
3. Use techniques to characterize the refractive index of the fabricated waveguides.

### **1.3.2 Specific objectives**

1. Design elliptical embedded waveguides with different diameters.
2. Fabricate buried waveguides on soda-lime glass using the FDLW technique with different manufacturing parameters, such as scan speed, NA, depth and laser energy. Explore their effect on the optical properties of the waveguide and establish the optimal parameters for high-quality waveguide fabrication.

3. Measure the core RI of fabricated waveguides using at least two established techniques to understand the properties of the waveguides and their suitability in optical systems.

This research project began with the need to validate the RI valued obtained by two different methods: One using the interferometric technique to obtain a faster calculation of the RI, and the near-field technique that uses the Helmholtz equation to obtain the RI value.

The significance of this research lies in the possibility of corroborating the RI estimated value of the near-field technique with the in situ measurement of the refractive index of the 3D buried waveguides using the extrinsic Fabry-Pérot interferometer. Therefore, we are able to establish optimal fabrication parameters to achieve the desired increase in  $\Delta n$ .

## 1.4 Structural outline

This thesis is composed of five chapters, including this introductory one, which are organized as follows:

In Chapter 2, the theoretical basis for the transmission of light through a dielectric waveguide, including the associated propagation losses, is briefly discussed.

In Chapter 3, the fabrication technique is discussed. This includes information about the laser writing system, the steps in making the buried waveguides, and how the waveguides are formed.

In Chapter 4, we describe the techniques utilized here to calculate the core-cladding index change in the buried waveguides in depth.

In Chapter 5, we analyze and discuss the results of  $\Delta n$  for the different techniques. Also, the size of the modes, dimensions of the waveguides, and propagation losses are shown.

In the last chapter of this thesis, we summarize the main conclusions of this project and suggest ideas for further research.

*“We must have perseverance and above all confidence in ourselves. We must believe that we are gifted for something.”*

Marie Curie

# 2

## Fundamental theory of light propagation in waveguides

An *optical waveguide* is a dielectric structure that provides a means to confine and guide light within a solid transparent medium. In practice, dielectric waveguides play a crucial role by serving as fundamental building blocks that support various optical devices.

This chapter provides an overview of the fundamental principles needed to propagate light inside dielectric waveguides.

We suppose the elliptical-shaped waveguides fabricated by FDLW as a circular-shaped dielectric waveguide (i.e. optical fibre) for the sake of an easy analysis of the propagation of light inside of it.

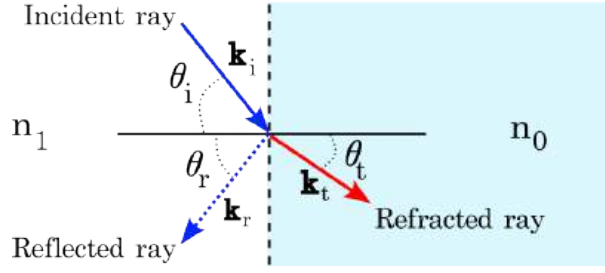


Figure 2.1: Diagram illustrating the various paths that light can take at the air-glass boundary, with the blue section representing glass and the white section representing air.

## 2.1 Total internal reflection and Snell's law

The propagation of light as explained by geometric optics provides a fundamental understanding of optical phenomena through the principles of Snell's Law and total internal reflection. At the boundary of two materials with different refractive indexes, light can either experience *reflection* or *refraction*.

In the case of light reflection, we have a plane of incidence defined by the surface and the incoming beam. The angle of incidence, denoted by  $\theta_i$ , is defined as the angle between the incoming beam and the normal surface. The reflected beam is also in the plane of incidence, and its angle of reflection, denoted by  $\theta_r$ , is equal to the angle of incidence. In the case of the refracted or transmitted beam, the angle is taken with respect to the normal and is denoted by  $\theta_t$ . This can be seen in Fig. 2.1.

We define wave vectors  $\mathbf{k}_i$ ,  $\mathbf{k}_t$ , and  $\mathbf{k}_r$  for each incident, transmitted and reflected light, respectively. The magnitudes of the vectors are:

$$|\mathbf{k}_i| = \frac{2\pi}{\lambda} n_0$$

$$|\mathbf{k}_t| = \frac{2\pi}{\lambda} n_1$$

$$|\mathbf{k}_r| = \frac{2\pi}{\lambda} n_0$$

where  $\lambda$  is the wavelength and  $n_0$ ,  $n_1$  stand for the refractive index of two media; the

waveguide ( $n_0$ ) and surrounding area ( $n_1$ ), respectively.

To reach the *Total Internal Reflection* (TIR) condition, all wave vectors must be in one plane:

$$(\mathbf{k}_i \cdot \mathbf{r})_{z=0} = (\mathbf{k}_r \cdot \mathbf{r})_{z=0} = (\mathbf{k}_t \cdot \mathbf{r})_{z=0} \quad (\text{Eq. 2.1})$$

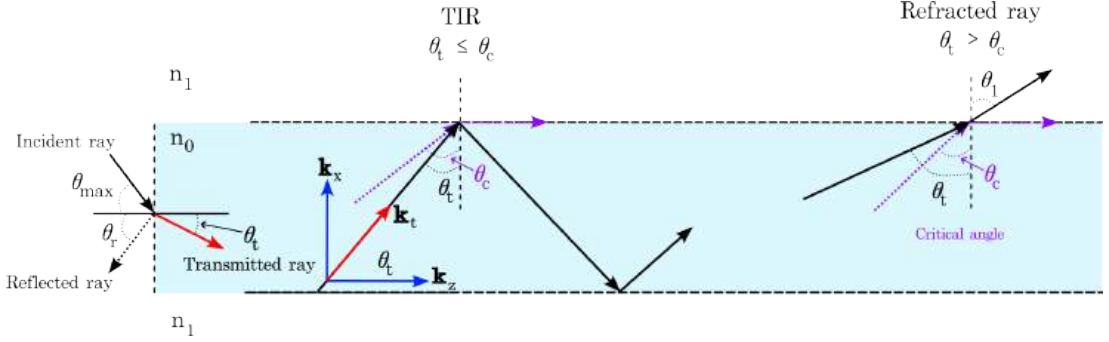


Figure 2.2: Representation of a ray of light traveling through a waveguide to illustrate the TIR, the critical angle, its relationship with the NA ( $\theta_{max}$ ) and the formation of evanescent waves by the refracted rays.

From the first part of Eq. 2.1, we find the **law of reflection**:

$$n_1 \sin(\theta_i) = n_1 \sin(\theta_r) \quad (\text{Eq. 2.2})$$

And from the first and last term of Eq. 2.1, we find **Snell's law**:

$$n_0 \sin(\theta_i) = n_1 \sin(\theta_t) \quad (\text{Eq. 2.3})$$

The most fundamental principle behind guided light waves is the TIR. This phenomenon occurs when light is trapped in a medium with a higher refractive index ( $n_0 > n_1$ ) and propagates inside the medium if the transmitted angle  $\theta_t$  is not greater than the critical angle  $\theta_c$ . When a wave is incident from medium 1 into medium 0, where  $n_0 > n_1$ , the angle of the ray refracted  $\theta_t$  will be smaller than the angle of incidence  $\theta_i$ . As  $\theta_i$  increases,  $\theta_t$  also increases until  $\theta_i$  reaches  $\pi/2$ . At this point, the angle of incidence  $\theta_i$  reaches a specific angle known as the critical angle ( $\theta_c$ ). When  $\theta_t = \frac{\pi}{2}$ , this signifies that  $\theta_c = \theta_{max}$ . The  $\theta_{max}$  denotes the maximum light acceptance angle or

cone of the waveguide and is known as *Numerical Aperture* (NA). At the value of  $\theta_t = \frac{\pi}{2}$  the transmission wave propagates along the interface; this is known as *evanescent wave* (see Fig. 2.2) [17].

For our analysis of circular geometry, we consider a cylindrical coordinate system and an approximation to a stepped refractive index. The direction of electromagnetic wave propagation is assumed to be along the  $z$  - *axis*, while the electric and magnetic fields are mutually perpendicular, and also perpendicular to the direction of wave propagation.

### 2.1.1 Guided modes in waveguides

To describe the behaviour of light trapped in the waveguide, the concept of *mode* is necessary. These are determined as solutions, or eigensolutions, to the wave equations for a specific wavelength and polarization. While the condition  $\theta_t \leq \theta_c$  is necessary for total internal reflection, the term *modes* refers to the distinct ways the wave can propagate within the waveguide, depending on factors like wavelength and waveguide geometry. Each mode is associated with light rays at a discrete propagation angle. Modes are given as particular standing wave patterns of transverse distribution maintained at all distances along the waveguide axis. The total electromagnetic field can be a combination of multiple modes. The mode number ( $m$ ) is related to the number of waves or rays propagating within the waveguide, as shown in Fig. 2.3. For example, *mode* = 0 has the largest incident angle, the next one has a lower angle, and so on; that is, as  $m$  increases, the angles of incidence  $\theta_i$  become smaller, and the higher modes (with larger  $m$ ) generally have more complex propagation patterns with steeper angles relative to the axis of the waveguide [1] [17].

The ray optics approach gives a very intuitive picture of the waveguide modes and their key characteristics. Nevertheless, this approach has many limitations for use in more complex shapes of the waveguide [18].

The *Optical Path Length* (OPL), denoted as  $L_o$ , is a measure of the distance that light travels through a medium, considering both the physical distance and the refractive index of the medium. It is an essential concept in optics because it accounts for

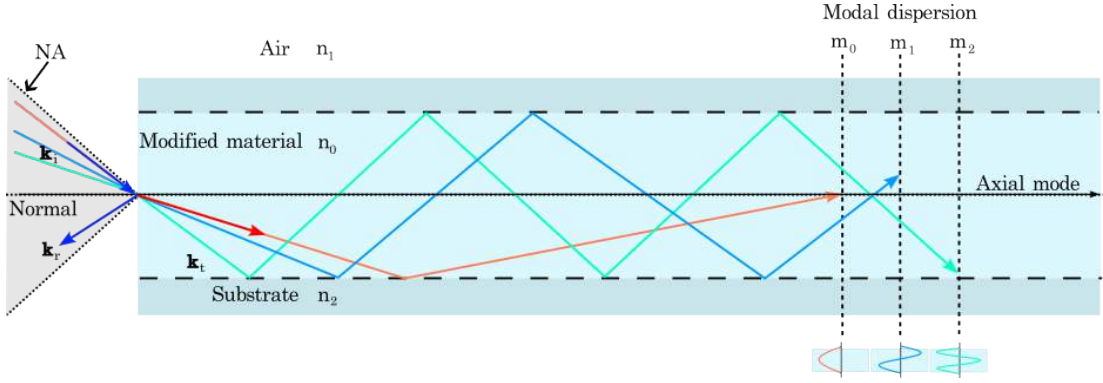


Figure 2.3: Modes of a waveguide. The field patterns are shown correspondingly: Orange is the fundamental mode ( $m=0$ ), blue is the guided first high-order mode ( $m=1$ ) and green the second high-order mode ( $m=2$ ).

how the speed of light changes when passing through materials with different refractive indices. Mathematically, it is given by the product of the *path length*  $L_p$  and the refractive index of the medium in which the light is propagating [19]:

$$L_o = n_0 L_p \quad (\text{Eq. 2.4})$$

## 2.2 General wave equation

Light is an electromagnetic wave consisting of oscillating electric and magnetic fields. These fields propagate perpendicular to each other and to the direction of propagation, oscillating harmonically in the temporal and spatial domains (see Fig. 2.4).

To describe propagation in space, we define the plane of incidence, which is the normal surface of the incoming beam. Electric and magnetic fields can be decomposed into two separate polarization components: *Transverse-Magnetic* (TM) and *Transverse-Electric* (TE). The behaviour of light as an electromagnetic wave is governed by Maxwell's equations. We start from these equations to find the wave equation of propagating light.

The Maxwell's equations presented next are in differential form:

*Faraday's law* states that a changing magnetic flux through a loop produces an induced

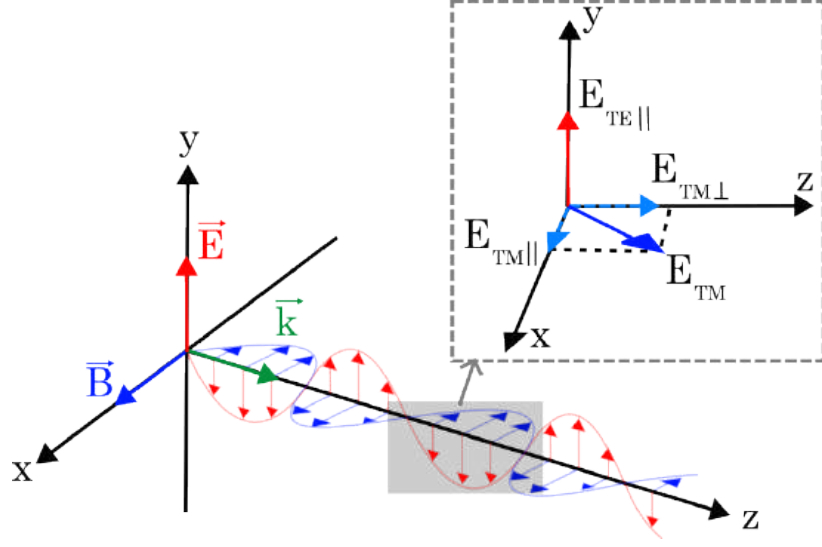


Figure 2.4: Exemplification of the relationship between  $\mathbf{E}$  and  $\mathbf{H}$  in a plane wave.

electric field.

$$\nabla \times \mathbf{E} = -\frac{\partial \mathbf{B}}{\partial t} \quad (\text{Eq. 2.5})$$

*Ampere's law* states that the flow of current along a given axis (such as the  $z$ -axis) produces a magnetic field that is orthogonal to the direction of the current.

$$\nabla \times \mathbf{H} = \mathbf{J} + \frac{\partial \mathbf{D}}{\partial t} \quad (\text{Eq. 2.6})$$

*Gauss's law for electric fields* states that the net electric flux through a closed surface is proportional to the electric charge density inside the surface.

$$\nabla \cdot \mathbf{D} = \rho \quad (\text{Eq. 2.7})$$

*Gauss's law for magnetic fields* states that the net magnetic flux through any closed surface is zero, meaning that particles always have a dipole.

$$\nabla \cdot \mathbf{B} = 0 \quad (\text{Eq. 2.8})$$

where  $\mathbf{E}$  is the electric field,  $\mathbf{H}$  is the magnetic field,  $\mathbf{D}$  is the electric displacement,  $\mathbf{B}$  is the magnetic induction or magnetic flux density,  $\mathbf{J}$  is the electric current density

(current per unit area), and  $\rho$  is the electric charge density (charge per unit volume) [20] [1]. It is worth to mention that  $\mathbf{E}$  and  $\mathbf{B}$  are fundamental microscopic fields, while  $\mathbf{D}$  and  $\mathbf{H}$  are macroscopic fields that incorporate the medium response.

A dielectric material is a non-conductive substance that lacks free charges or currents, i.e no sources ( $\rho = 0$ ,  $\mathbf{J} = 0$ ), does not exhibit magnetic properties, and is an isotropic medium. Electric permittivity  $\varepsilon$  and permeability  $\mu$  are non-dependent on  $\mathbf{E}$  and  $\mathbf{H}$ , respectively. With these conditions superimposed Eq. 2.5, Eq. 2.6, Eq. 2.7, and Eq. 2.8 are simplified to:

$$\textit{Faraday's law} \qquad \qquad \qquad \nabla \times \mathbf{E} = -\mu_0 \frac{\partial \mathbf{H}}{\partial t} \qquad \qquad \qquad (\text{Eq. 2.9})$$

$$\textit{Ampere's law} \qquad \qquad \qquad \nabla \times \mathbf{H} = \varepsilon_0 n^2 \frac{\partial \mathbf{D}}{\partial t} \qquad \qquad \qquad (\text{Eq. 2.10})$$

$$\textit{Gauss's law for electric fields} \qquad \qquad \qquad \nabla \cdot \mathbf{D} = 0 \qquad \qquad \qquad (\text{Eq. 2.11})$$

$$\textit{Gauss's law for magnetic fields} \qquad \qquad \qquad \nabla \cdot \mathbf{B} = 0 \qquad \qquad \qquad (\text{Eq. 2.12})$$

where  $n$  is the refractive index of the medium.

The previous equations consider the waves on the vacuum (Eq. 2.9 to Eq. 2.12), we can adapt them and derive from them the wave equation for the electric field and the magnetic induction field in dielectric media [17] [21]:

*Wave equation for the electric field:*

$$\nabla^2 \mathbf{E} = \mu_0 \varepsilon_0 n^2 \frac{\partial^2 \mathbf{E}}{\partial t^2} \qquad \qquad \qquad (\text{Eq. 2.13})$$

*Wave equation for the magnetic field:*

$$\nabla^2 \mathbf{H} = \mu_0 \varepsilon_0 \frac{\partial \mathbf{H}}{\partial t^2} - \frac{1}{n^2} \nabla^2 \times (\nabla \times \mathbf{H}) \qquad \qquad \qquad (\text{Eq. 2.14})$$

## 2.3 Light propagation in cylindrical waveguides and their propagation modes

In a waveguide, the electromagnetic field is propagated through the waveguide by TIR from the walls of the structure. If the transverse dimensions, e.g. shape and size of the waveguide, are comparable to the wavelength of light, only certain field distributions, or modes, will satisfy Maxwell's equations and the boundary conditions [22].

Because we are dealing with waveguides with circular geometry, we use a cylindrical coordinate system and a stepped refractive index to facilitate the analysis. Electromagnetic wave propagation is assumed to occur along the  $z$  – *axis*, with mutually perpendicular electric and magnetic fields that are also perpendicular to the direction of wave propagation (Fig. 2.4) [23].

$$\mathbf{E} = \mathbf{E}(r, \theta)e^{i(\omega t - \beta z)} \quad (\text{Eq. 2.15})$$

$$\mathbf{H} = \mathbf{H}(r, \theta)e^{i(\omega t - \beta z)} \quad (\text{Eq. 2.16})$$

where  $i$  denotes the imaginary unit,  $\omega$  is the frequency of oscillation and  $\beta$  is the propagation constant or ray invariant, defined by the translational invariance of the waveguide; a ray of light that is constant along the path and specifies the direction at any position in the cross-section [19].

Using Eq. 2.15 and Eq. 2.16 in Eq. 2.13 and Eq. 2.14, we obtain the wave equations for the electric and magnetic fields in their general form:

$$\nabla_T^2 \mathbf{E}(r, \theta) + (k_0^2 n^2 - \beta^2) \mathbf{E}(r, \theta) = 0 \quad (\text{Eq. 2.17})$$

$$\nabla_T^2 \mathbf{H}(r, \theta) + (k_0^2 n^2 - \beta^2) \mathbf{H}(r, \theta) = 0 \quad (\text{Eq. 2.18})$$

where  $k_0$  is the wave number in vacuum and  $\nabla_T$  is the transverse Laplacian, that in

cylindrical coordinates, is given by:

$$\nabla_T^2 = \frac{1}{r} \frac{\partial}{\partial r} \left( r \frac{\partial}{\partial r} \right) + \frac{1}{r^2} \frac{\partial^2}{\partial \theta^2} \quad (\text{Eq. 2.19})$$

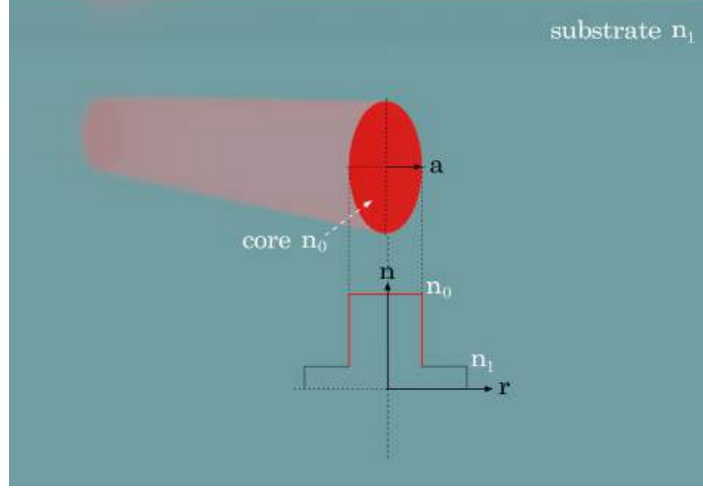


Figure 2.5: Nomenclature and step index representation of a buried cylindrical waveguide, where  $a$  is the core radius,  $n_0$  the refractive index at the core, and  $n_1$  is the refractive index of the medium (substrate).

Considering a cylindrical coordinate system as a solution to Maxwell's equations, we have the following:

$$\mathbf{E}(r, \theta, z, t) = R(r)e^{(\pm il\theta)}e^{i(\omega t - \beta z)} \quad (\text{Eq. 2.20})$$

where the parameter  $l$  represents the integer values of the solution of the angular component ( $\theta$ ).

By inserting Eq. 2.15 and Eq. 2.16 into Eq. 2.10, and Eq. 2.9, respectively, and making the appropriate substitutions, we find:

$$r^2 \frac{d^2 R}{dr^2} + r \frac{dR}{dr} + ((k_0^2 n^2 - \beta^2)r^2 - l^2)R = 0 \quad (\text{Eq. 2.21})$$

From Fig. 2.5 we see that a buried waveguide can be approximated to a step

refractive index is:

$$\begin{array}{lll} n_0 & -a \leq r \leq a & \text{core} \\ n_1 & r > |a| & \text{substrate} \end{array} \quad (\text{Eq. 2.22})$$

If we assume that the fields inside the core are oscillating while decaying exponentially outside of it, we can derive solutions as follows:

$$r^2 \frac{d^2 R}{dr^2} + r \frac{dR}{dr} + \left( u^2 \frac{r^2}{a^2} - l^2 \right) R = 0; \quad -a \leq r \leq a \quad (\text{Eq. 2.23})$$

$$r^2 \frac{d^2 R}{dr^2} + r \frac{dR}{dr} + \left( v^2 \frac{r^2}{a^2} + l^2 \right) R = 0; \quad r > |a| \quad (\text{Eq. 2.24})$$

where

$$u = a \sqrt{(k_0^2 n_0^2 - \beta^2)} \quad (\text{Eq. 2.25})$$

$$v = a \sqrt{(\beta^2 - k_0^2 n_1^2)} \quad (\text{Eq. 2.26})$$

We can combine the refractive index with the wavelength  $\lambda$  of light propagating along the waveguide to form a single dimensionless parameter  $V$ , known as the *waveguide parameter*, or *waveguide frequency* [19]:

$$V = \sqrt{(u^2 + v^2)} = k_0 a \sqrt{(n_0^2 - n_1^2)} \quad (\text{Eq. 2.27})$$

with  $k_0 = \frac{2\pi}{\lambda_0}$

To ensure light confinement within the material, the following condition should be met:

$$n_1^2 k_0^2 < \beta^2 < n_0^2 k_0^2$$

As a result, to obtain guided modes, both  $u$  and  $v$  must have real values.

Since the solutions to Eq. 2.23 and Eq. 2.24 are Bessel functions, they can be

expressed as:

$$R(r) = J_l\left(\frac{u}{a}r\right), \quad -a \leq r \leq a \quad (\text{Eq. 2.28})$$

In the region ( $r > a$ ) of the substrate, the solution  $R(r)$  must exhibit exponential decay for large values of  $r$ . The solution for this region is given by the modified Bessel function  $K_l$ . Hence, we obtain:

$$R(r) = K_l\left(\frac{v}{a}r\right), \quad r > |a| \quad (\text{Eq. 2.29})$$

To obtain a physically viable general solution, we must ensure that there is continuity between Eq. 2.28 and Eq. 2.29 and their first derivative at the boundary ( $r = a$ ). This leads to the following equation:

$$u \frac{J_{l-1}(u)}{J_l(u)} = -\frac{K_{l-1}(v)}{K_l(v)} \quad (\text{Eq. 2.30})$$

To determine the propagation modes permitted, we need to solve Eq. 2.30.

There is a more general equation to find the permitted propagation modes. Defining the effective index as:

$$n_{eff} = \frac{\beta}{k_0} \quad (\text{Eq. 2.31})$$

and the normalized propagation constant:

$$b = \frac{n_{eff}^2 - n_1^2}{n_0^2 - n_1^2} = \frac{v^2}{V^2} \quad (\text{Eq. 2.32})$$

then as a consequence, we have:

$$v = V\sqrt{b} \quad (\text{Eq. 2.33})$$

and

$$u = \sqrt{V^2 - v^2} = V\sqrt{1 - b} \quad (\text{Eq. 2.34})$$

Lastly, we can rewrite the transcendental equation as:

$$V(\sqrt{1-b}) \frac{J_{l-1}(V\sqrt{1-b})}{J_l(V\sqrt{1-b})} = -V(\sqrt{b}) \frac{K_{l-1}(V\sqrt{b})}{K_l(V\sqrt{b})}, \quad l \geq 1 \quad (\text{Eq. 2.35})$$

and

$$V(\sqrt{1-b}) \frac{J_1(V\sqrt{1-b})}{J_0(V\sqrt{1-b})} = V(\sqrt{b}) \frac{K_1(V\sqrt{b})}{K_0(V\sqrt{b})}, \quad l = 0 \quad (\text{Eq. 2.36})$$

which can be numerically solved by knowing the refractive indices, the wavelength, and the size of the waveguide.

The solutions of these transcendental equations determine the curves of the propagation constant  $b$  as a function of the normalized frequency  $V$ ,  $u$ , and  $v$  for the electromagnetic field equation. To ensure finite solutions, there must be values of propagation modes ( $m$ ) that correspond to the radial part of the equation for a given value of  $l$  for the angular solution. The weak guidance condition ( $n_0 \approx n_1$ ) yields  $LP_{lm}$  modes (Linearly Polarized modes), which are the most common modes found in fibres with weak guidance (i.e., weak contrast between the refractive indices). We obtain the smallest solution by solving the transcendental equation for  $l = 0$  (lowest mode). The  $LP_{01}$  mode, which is the fundamental or Gaussian mode, is obtained when  $m = 1$  [24].

The  $LP_{01}$  mode is the most commonly observed in optical fibers and waveguides. It has a Gaussian intensity distribution, meaning it is the most efficient in terms of power propagation because the light is evenly distributed across the core of the waveguide. Understanding this mode is crucial for designing waveguide systems, where the fundamental mode often carries most of the signal.

## 2.4 Losses in dielectric waveguides

The *insertion loss* is the attenuation of an optical signal when a device or component is inserted into the optical path. This parameter quantifies how much of the signal is lost due to a specific component, such as a waveguide structure, connector or a splice [18,25].

The *insertion loss* can be defined as:

$$Loss_{dB} = -10 \text{Log}_{10} \left( \frac{I_{out}}{I_{in}} \right) \quad (\text{Eq. 2.37})$$

And is typically expressed in decibels  $dB$ .

Key contributors of the *insertion loss*:

- *Dispersion*: The geometry and structure of optical waveguides, related to fabrication parameters, influence the confinement of the light inside the waveguide.
- *Material absorption*: Due to intrinsic properties of the material.
- *Reflection losses*: Mismatches in impedance or refractive index at interfaces (e.g., between waveguides or between a waveguide and a connector) can cause reflection, leading to losses.
- *Coupling losses*: Inefficient confinement between components (e.g., from a fibre to a waveguide) can lead to power (energy) loss.
- *Bending losses*: When the waveguide is bent, some of the light may radiate out of the waveguide, increasing insertion loss.

For buried waveguides in soda lime, reflection and coupling losses are particularly important, because they contribute more to the overall losses. Specifically [26]:

- *Mode-size mismatch*.
- *fibre-waveguide misalignment*.
- *Fresnel reflection*.

From the Eq. 2.37,  $I_{in}$  refers to the power input, while  $I_{out}$  represents the power output of the system. Losses per unit length or propagation loss rate ( $\alpha$  [ $dB/cm$ ]) can be determined by the ratio of Eq. 2.37 to the physical length  $L$  [ $cm$ ] of the waveguide.

$$\alpha = \frac{Loss_{dB}}{L} = -\frac{10}{L} \text{Log}_{10} \left( \frac{I_{out}}{I_{in}} \right) \quad (\text{Eq. 2.38})$$

We can measure the quality of the fabricated waveguide by calculating the losses resulting from light propagation inside it. In Eq. 2.38, it is assumed that all the input energy  $I_{in}$  is coupled to the waveguide. However, there are losses due to coupling caused by poor alignment of the optical axes when coupling light to the waveguide through an optical fibre, as *multiple reflections* between the fibre-air-waveguide, as well as the *decoupling* of transverse modes due to the differences between the mode field distributions of the fibre and the mode supported by the waveguide.

Additionally, there is energy loss at the waveguide output due to *Fresnel reflection* at the waveguide-air interface. *Fresnel reflection* comes from refractive index changes at the interface (air-glass) and may create unbearable back-reflections and incurred at the start/end of the waveguide, this is why they are not considered as caused by propagation within the waveguide. Hence, the input energy  $I_{in}$  is reduced, and only an energy amount  $I_{ac}$  is poured into the waveguide, which can be used to evaluate the quality of the fabricated waveguide.

$$I_{ac} = \eta_{ac} I_{in} \quad (\text{Eq. 2.39})$$

The *coupling coefficient*  $\eta_{ac}$  takes into account the effects of poor alignment, multiple reflections, and the coupling of transverse modes. Therefore, to calculate the *propagation loss coefficient*  $\alpha_p$  [dB/cm], the coupled energy  $I_{ac}$  from Eq. 2.39 is substituted for the input energy  $I_{in}$  in Eq. 2.38, obtaining the following:

$$\alpha_p = -\frac{10}{L} \text{Log}_{10} \left( \frac{I_{out}}{\eta_{ac} I_{in} T_F} \right) \quad (\text{Eq. 2.40})$$

Here, we have also added  $T_F$ , which is the *light transmittance due to Fresnel reflection* at the waveguide-air interface. Then the confinement coefficient  $\eta_{ac}$  is given by:

$$\eta_{ac} = \eta_{alg} \eta_{mul} \eta_{modes} \quad (\text{Eq. 2.41})$$

The parameter  $\eta_{alg}$  represents the *alignment loss coefficient*, which is assumed to be one when there is good alignment. The parameter  $\eta_{mul}$  represents the *efficiency due to multiple reflections* between the fibre-air-waveguide, while the parameter  $\eta_{modes}$  represents the *efficiency due to the coupling of transverse modes*.

### 2.4.1 Efficiency due to multiple reflections

To couple light into the waveguide, an optical fibre is used as close as possible to the face of substrate where the waveguide is located. Separation can be monitored using a digital microscope at the top of the system and the *fibre-waveguide distance* ( $z$ ) desired is achieved on the microscale ( $\approx 5\mu m$ ). Because the air gap between the fibre and waveguide is of the order of the incident light wavelength ( $\lambda = 1.5\mu m$ ), a thin air film is formed, where multiple reflections occur back and forth between the fibre-air-waveguide, causing interference between different rays. Therefore the **Fresnel reflection** ( $\eta_r$ ) of this thin film is as follows:

$$\eta_r = \frac{\left(\frac{n_f - n_z}{n_f + n_z}\right)^2 + \left(\frac{n_g - n_z}{n_g + n_z}\right)^2 + 2\left(\frac{n_f - n_z}{n_f + n_z}\right)\left(\frac{n_g - n_z}{n_g + n_z}\right)\cos\left(\frac{4\pi n_z z}{\lambda}\right)}{1 + \left(\frac{n_f - n_z}{n_f + n_z}\right)^2 + \left(\frac{n_g - n_z}{n_g + n_z}\right)^2 + 2\left(\frac{n_f - n_z}{n_f + n_z}\right)\left(\frac{n_g - n_z}{n_g + n_z}\right)\cos\left(\frac{4\pi n_z z}{\lambda}\right)} \quad (\text{Eq. 2.42})$$

where:

$n_f$  - Effective index of the fibre core.

$n_g$  - Effective index of the waveguide core.

$n_z$  - Refractive index of the gap between the fibre and the waveguide.

$\lambda$  - wavelength.

So, the transmittance,  $\eta_{mul}$ , due to the *Fresnel reflection* phenomenon, is calculated as:

$$\eta_{mul} = T_{mul} = 1 - \eta_r \quad (\text{Eq. 2.43})$$

The equation above shows that the efficiency or transmittance,  $\eta_{mul}$ , due to multiple reflections depends on the effective refractive indices of the fibre core ( $n_f$ ), the

waveguide core ( $n_g$ ), the medium between them ( $n_z$ ), the separation between the fibre and the waveguide ( $z$ ), and the wavelength  $\lambda$ .

### 2.4.2 Mode-size mismatch

The coupling between the transverse modes of any two waveguides is given by:

$$\eta_{modes} = \frac{\left| \int_{-\infty}^{\infty} \psi_1(x, y) \psi_2(x, y) dx dy \right|^2}{\int_{-\infty}^{\infty} |\psi_1|^2 dx dy \int_{-\infty}^{\infty} |\psi_2|^2 dx dy} \quad (\text{Eq. 2.44})$$

where  $\psi_1$  and  $\psi_2$  are the electric field amplitudes of the fibre and waveguide modes, respectively.

The mode of a single-mode optical fibre is well described by a circular Gaussian mode:

$$\psi_1(x, y) = A_0 e^{-\left(\frac{x^2 + y^2}{\omega_0^2}\right)} \quad (\text{Eq. 2.45})$$

where  $\omega_0$  is the *radius of the mode*.

The waveguide mode is generally eccentric ( $\omega_1 + \omega_3 \neq 2\omega_2$ ) and asymmetric ( $\omega_1 \neq \omega_3$ ), and near the substrate surface the waveguide mode can be represented as a combination of Gaussians (see Fig. 2.6 ) [27]:

$$\psi_2(x, y) = f(x) \cdot g(y) \quad (\text{Eq. 2.46})$$

where

$$f(x) = F_0 e^{\left(\frac{-x^2}{\omega_2^2}\right)} \quad (\text{Eq. 2.47})$$

and

$$\begin{aligned} g(y) &= G_0 e^{\left(\frac{-y^2}{\omega_1^2}\right)}, y < 0 \\ g(y) &= G_0 e^{\left(\frac{-y^2}{\omega_3^2}\right)}, y \geq 0 \end{aligned} \quad (\text{Eq. 2.48})$$

The values  $\omega_1$ ,  $\omega_2$ , and  $\omega_3$  represent the mode radii of the waveguide, and  $d$  represents the depth of focus. They are illustrated in Fig. 2.6.

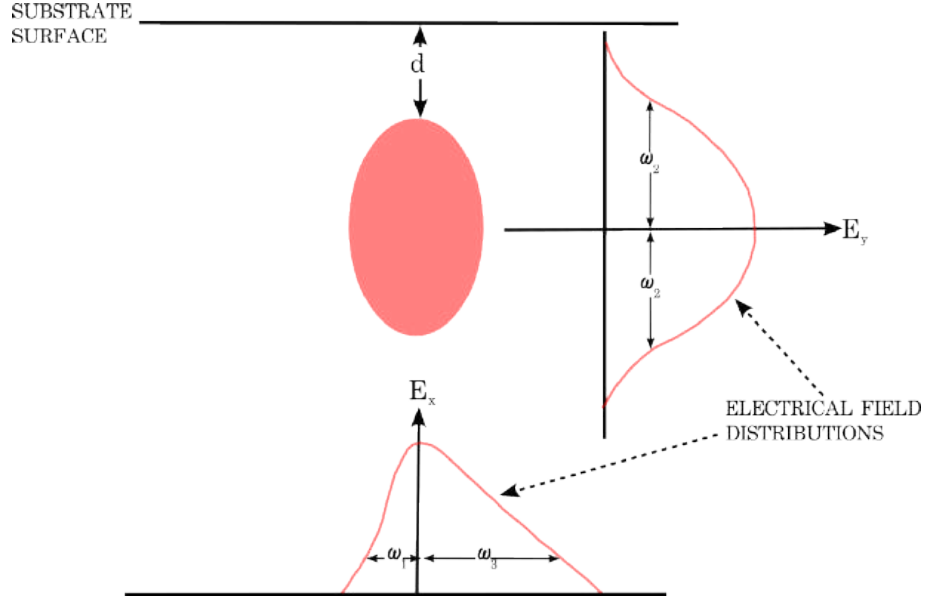


Figure 2.6: Typical distribution of waveguide mode profiles in a transverse propagation.

By substituting Eq. 2.45, Eq. 2.46, Eq. 2.47 and Eq. 2.48 into Eq. 2.44, we obtain the expression of the coupling efficiency entirely in terms of modal parameters:

$$\eta_{modes} = \frac{2 \left[ \left( \frac{1}{\omega_0^2} + \frac{1}{\omega_1^2} \right)^{-\frac{1}{2}} + \left( \frac{1}{\omega_0^2} + \frac{1}{\omega_3^2} \right)^{-\frac{1}{2}} \right]^2}{\omega_0^2 \omega_2 (\omega_1 + \omega_3) \left( \frac{1}{\omega_0^2} + \frac{1}{\omega_2^2} \right)} \quad (\text{Eq. 2.49})$$

If we assume that the transverse mode profile in Fig. 2.6 is eccentric but symmetric, that is  $\omega_3 = \omega_1$ , we obtain that the *coupling coefficient*  $\eta_{modes}$  at the waist (assuming perfect alignment) of the waveguide is given by [25] [28]:

$$\eta_{modes} = \frac{4}{\left( \frac{\omega_2}{\omega_0} + \frac{\omega_0}{\omega_2} \right) \left( \frac{\omega_1}{\omega_0} + \frac{\omega_0}{\omega_1} \right)} \quad (\text{Eq. 2.50})$$

where:

$\omega_0$  is the radius of the incident mode.

$\omega_1$  the horizontal radius of the waveguide mode.

$\omega_2$  is the vertical radius of the waveguide mode.

### 2.4.3 Transmission due to Fresnel reflection

The Fresnel transmission coefficient from medium 1 to medium 2, for normal incidence between two non-conductive media, is given by [29]:

$$t_{12} = \frac{2n_1}{n_1 + n_2} \quad (\text{Eq. 2.51})$$

where  $n_1$  and  $n_2$  are the RI of medium 1 and medium 2, respectively. Thus, the transmittance from medium 1 to medium 2 is defined as follows:

$$T_F = \frac{n_2}{n_1} t_{12}^2 = \frac{4n_1 n_2}{(n_1 + n_2)^2} \quad (\text{Eq. 2.52})$$

*“The most difficult thing is the decision to act;  
the rest is merely tenacity.”*

Amelia Earhart

# 3

## Femtosecond-written waveguide fabrication

A wide variety of techniques have been developed for the fabrication of microcomponents and devices using polymer, glass, and silicon substrates. These techniques can be categorized into two classes: parallel processing techniques based on photolithography and serial processing techniques based on direct writing [2].

Although parallel processing techniques are typically faster than serial processing techniques for manufacturing a large number of chips, they often require expensive clean-room facilities, such as photolithography systems and specialized expertise. However, serial processing techniques allow for rapid prototyping of microstructures in a more cost-effective manner, particularly when producing small quantities of individual components [2].

This chapter explores the complexities of the serial technique used to create buried waveguides on a soda-lime substrate. We investigate the internal operations and fea-

tures that occur within the substrate material and explain the essential procedures that result in the formation of these waveguides.

### 3.1 Femtosecond direct laser writing technique

The fabrication of waveguiding structures in bulk glass using focused femtosecond laser pulses is an established process. It can be performed under different scanning geometries, scan inscription velocity, NA, energy of the laser, wavelength, pulse duration, repetition rate, polarization, and depth, applied to samples to control the change in the refractive index of the waveguide [30]. During laser ablation, the energy that reaches the sample is absorbed, transmitted, and reflected depending on the properties of the materials [31].

In this thesis, the FDLW technique is applied using a *Coherent Libra HE* amplified laser with an arranged Ti:Sapphire amplification system. This laser emits  $50fs$  pulses with an average energy of  $1mJ$  at  $1kHz$  of repetition rate, with a wavelength centered at  $800nm$ . Our system is integrated with a *Newport  $\mu FAB$  microfabrication workstation* (see Fig. 3.1 and 3.2). These two devices constitute the essential elements for fabricating buried waveguides at the *Ultrafast Optics Laboratory (LOU)* in the *Optical Research Center (CIO)*.

The *Newport  $\mu FAB$  microfabrication workstation* has three motors to control the movement of the workpiece through an XYZ motion system, with a travel distance of  $100mm \times 100mm \times 5mm$ , respectively, with a resolution  $\pm 0.05\mu m$  and a maximum XY speed of  $300mm/s$ . A reflective light microscope monitors the laser processing in real time, with the vision system being on-axis. The interface user is a simple and intuitive software for advanced laser processing [32]. The  $\mu FAB$  station controls the energy delivered by the *Libra HE laser* with a shutter.

#### 3.1.1 Fundamentals of femtosecond laser writing in glass

FDLW enables integrated optostructures with complex three-dimensional geometries to be buried in glass, eliminating the need to use multistep procedures [2]. Femtosecond

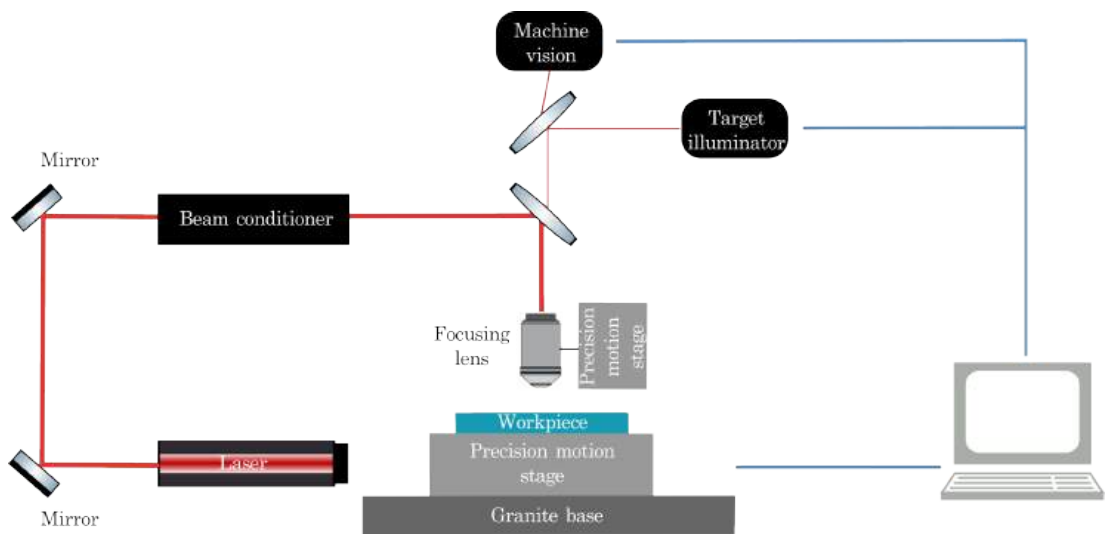


Figure 3.1: Diagram of the experimental setup for the FDLW technique.

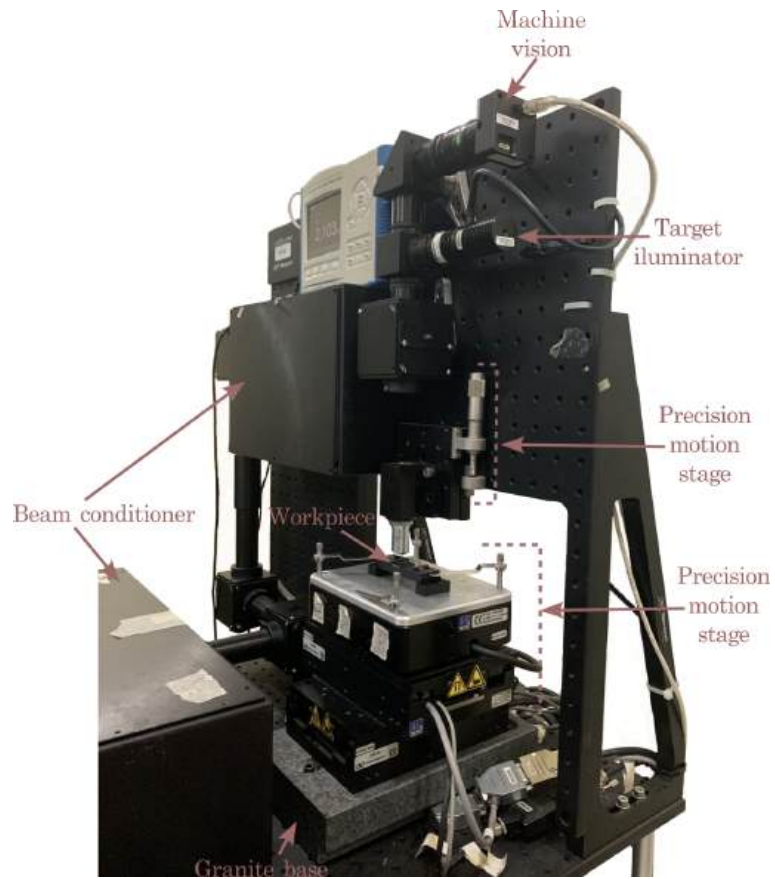


Figure 3.2: Picture of the  $\mu$ FAB microfabrication workstation.

laser micromachining has the advantage of having an ultrashort pulse width and an extremely peak intensity, which gives it unique characteristics [33]. The short pulse width suppresses the formation of a *Heat-Affected Zone* (HAZ), which is vital for ultrahigh precision fabrication, whereas high peak intensity allows nonlinear interactions such as multiphoton absorption to be induced in transparent materials [34]. HAZ has been explained as rapid energy deposition in the material, which is why FDLW is known as a nonthermal process. It takes a few picoseconds for the electron distribution to reach thermal equilibrium after the femtosecond laser irradiates the substrate. This irradiation leads to the generation of electron heating that generates a hot electron gas, converting only a tiny fraction of the laser energy into heat, resulting in the nonthermal processing required for microfabrication [33].

Femtosecond lasers can selectively modify the interior of glass by multiphoton absorption, which occurs only near the focal spot where the laser intensity exceeds a certain threshold. Femtosecond laser irradiation can alter both optical (e.g., refractive index) and chemical properties (e.g., chemical etch rate) of the glass. This makes it easy to fabricate buried waveguides using a tightly focused femtosecond laser beam [35].

Femtosecond lasers enable the processing of most materials with extremely high precision and negligible shock or thermal loading to the surrounding area [36]. When materials like dielectrics and wide-bandgap crystals, which are transparent to the laser wavelength, are exposed to femtosecond laser irradiation, electron excitation (ionization) can occur through nonlinear processes like multiphoton absorption or tunnelling ionization. These processes are a result of the laser's extremely high peak intensity [33].

The probabilities of multiphoton absorption and tunnelling ionization in femtosecond laser interaction with transparent materials can be determined by the Keldysh parameter  $\gamma$ . When  $\gamma \gg 1$  ( $\gamma \ll 1$ ), multiphoton absorption (tunnelling ionization) dominates, and for  $\gamma \approx 1$ , photoionization is induced by a combination of both processes [37]. Fig. 3.3 shows multiphoton absorption based on the electron excitation process in the bandgap of glass materials. Light with a photon energy smaller than the bandgap cannot excite electrons, so no absorption is induced in the stationary state. However, when an extremely high photon density is simultaneously incident on the

material, an electron can be excited by multiple photons via virtual states, even if the photon energy is smaller than the bandgap. This phenomenon is referred to as multiphoton absorption. High photon density can be easily obtained using femtosecond lasers due to the ultrashort pulse width [2].

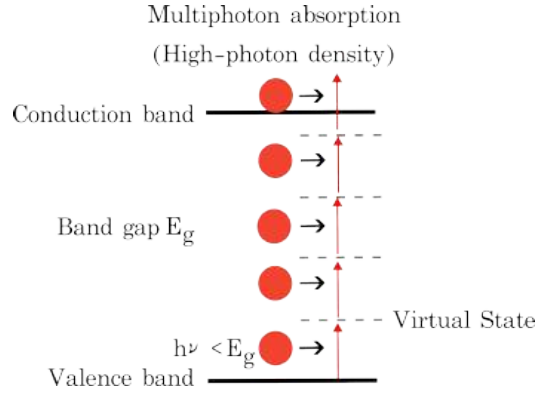


Figure 3.3: Excitation multiphoton process of electrons in bandgap materials through multiple photons [2].

The threshold or critical value is determined by the pulse width and material. If a transparent material is exposed to a femtosecond laser beam with sufficient pulse energy, absorption can occur in the immediate vicinity of the focal point (see Fig. 3.4). As a result, it becomes possible to perform internal modification and structure fabrication [2].

The use of femtosecond lasers allows for the suppression of heat diffusion in the vicinity of the processed region. This characteristic is advantageous as it results in improved spatial resolutions. When the laser used to irradiate the substrate has a typical spot size equal to the wavelength, the processed area expands beyond the size of the laser spot due to the length of thermal diffusion. On the other hand, due to the minimal thermal diffusion during femtosecond laser irradiation, it is improbable for the affected area to exceed the spot size [2].

Nonlinear multiphoton absorption has the potential to enhance spatial resolution. In an ideal scenario, the spatial intensity of a femtosecond laser beam follows a Gaussian profile (see Fig. 3.5). In the case of single-photon absorption, the distribution of absorbed laser energy by the material aligns with this beam profile. However, in the case

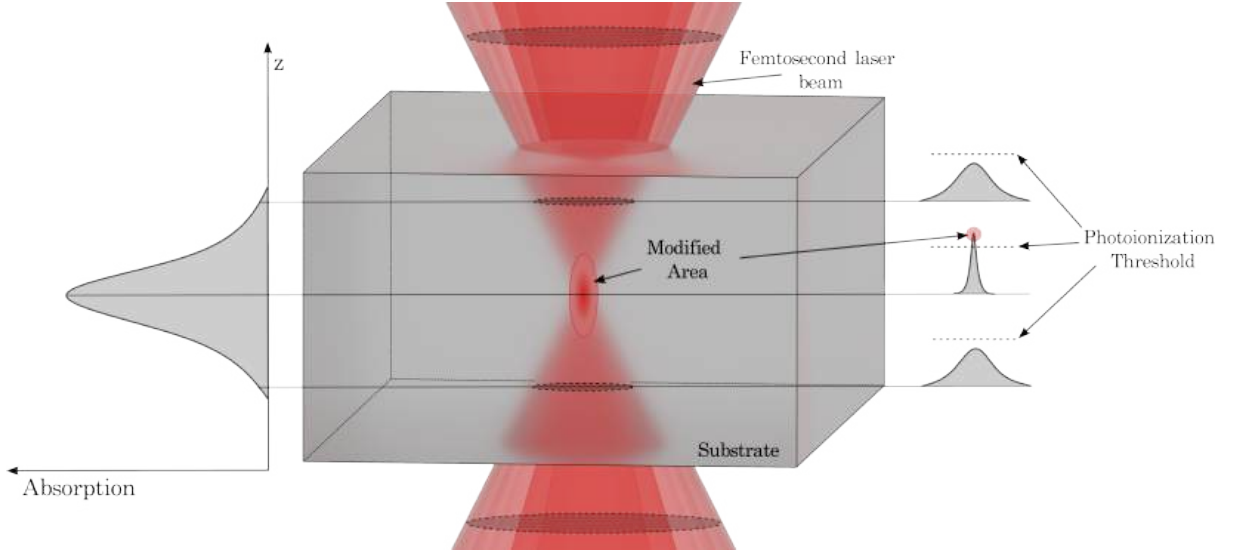


Figure 3.4: Illustration of the internal modification within the transparent substrate caused by femtosecond laser irradiation through multiphoton absorption.

of multiphoton absorption or three photon absorption, the absorbed energy distribution becomes narrower and smaller as the order ( $n$ ) of multiphoton absorption increases. This is because the effective absorption coefficient for  $n$ -photon absorption is directly proportional to the  $n$ th energy of the laser intensity [2]. As a result, the effective beam size  $\omega$  for  $n$ -photon absorption can be expressed as:

$$\omega = \frac{\omega_0}{\sqrt[n]{n}} \quad (\text{Eq. 3.1})$$

In addition, the fabrication resolution can be improved by adjusting the laser intensity. Therefore, the utilization of nonlinear multiphoton absorption enables the surpassing of the diffraction limit imposed by the laser wavelength, thus achieving a subdiffraction resolution [2].

### 3.1.2 Laser-material interaction

The process of modifying the refractive index within the material can be divided into three primary stages: the initial *generation of a free-electron plasma*, which is then followed by the *energy relaxation* and subsequent *modification of the material*. Next, we will explain briefly how every stage happens.

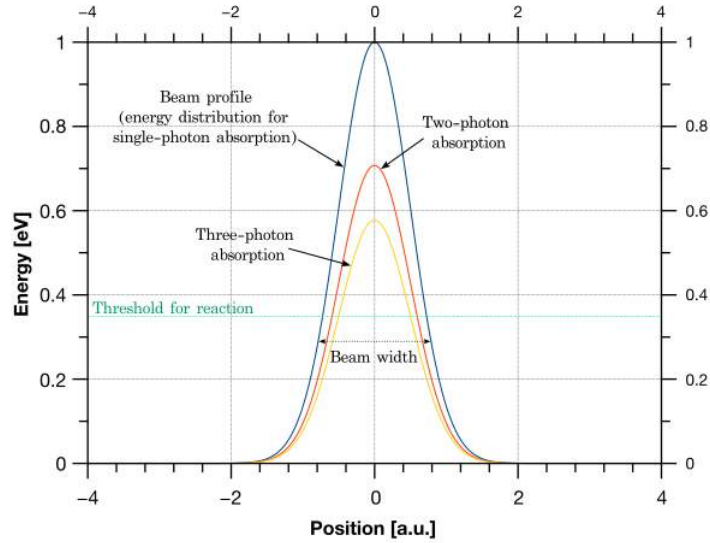


Figure 3.5: Representation example of spatial distribution of the laser energy absorbed by transparent materials; One-photon (blue), two-photon (orange), and three-photon (yellow). The green line indicates the required value to exceed in order to induce changes within the glass (3.5 eV for soda-lime).

Focused femtosecond laser pulses, with wavelengths in the visible or near-infrared spectra, have insufficient photon energy to be linearly absorbed in glasses. Valence electrons are instead promoted to the conduction band through nonlinear photoionization, which proceeds by multiphoton ionization and/or tunneling photoionization pathways depending on the laser frequency and intensity. In our case, we will be focusing on multiphoton ionization as it is the primary mechanism at high frequencies and low laser intensities [38].

If we irradiate the substrate with a slightly higher intensity (closer to the threshold), excited electrons can sequentially absorb several photons in the same laser pulse, so that they are excited to higher energy states for which free-carrier absorption is efficient. At sufficiently high laser intensities, excited electrons are accelerated by the intense electric field of the ultrafast laser beam and collide with surrounding atoms, generating secondary electrons (avalanche ionization), which cause a Coulomb explosion and eventually nonthermal ablation. Glass heating occurs a few tens of picoseconds

after laser irradiation due to free-electron relaxation, and the irradiated area returns to room temperature after several tens of microseconds, causing modification or damage (See Fig. 3.6) [2], [5].

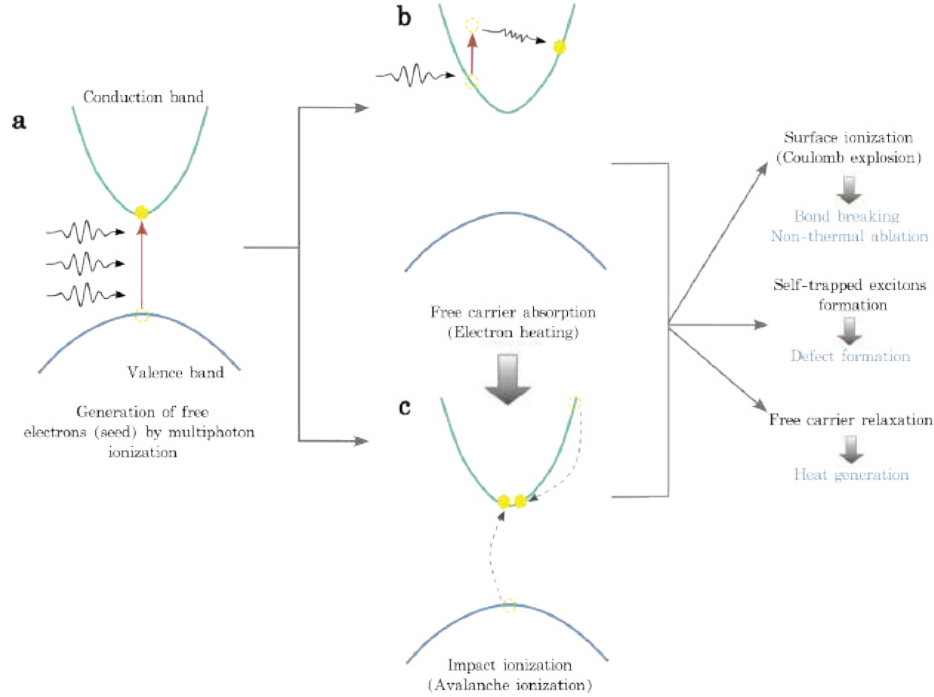


Figure 3.6: Nonlinear photoionization processes in glass by femtosecond laser irradiation. (a) Multiphoton absorption, (b) avalanche ionization, made by free carrier absorption, followed by (c) impact ionization or the continuity of avalanche ionization.

Due to the fact that avalanche photoionization relies solely on laser intensity, the optical breakdown threshold intensity shows only a minimal fluctuation with the bandgap energy of the material. Because of this low dependence of the breakdown threshold on the bandgap energy, femtosecond laser microfabrication can be applied in a wide range of materials [5]. At low pulse energies, glasses exhibit a gradual refractive index modification, allowing the fabrication of photonic devices. For this to happen, we have to control the parameters that strongly influence the resulting morphology after femtosecond laser exposure: repetition rate, scan speed, focusing condition NA, polarization, pulse duration, depth, and direction [14].

The observed morphological changes can be generally classified into three types of structural changes: a smooth refractive index change, a form birefringent refractive

index modification, and microexplosions leading to empty voids; see Fig. 3.7. Because of the nonlinear nature of the interaction, absorption takes place only within the focal volume located deep inside the bulk material. By using computer-controlled motion stages to move the sample in relation to the laser focus, it is possible to create a region with a higher refractive index along any desired three-dimensional path [14].

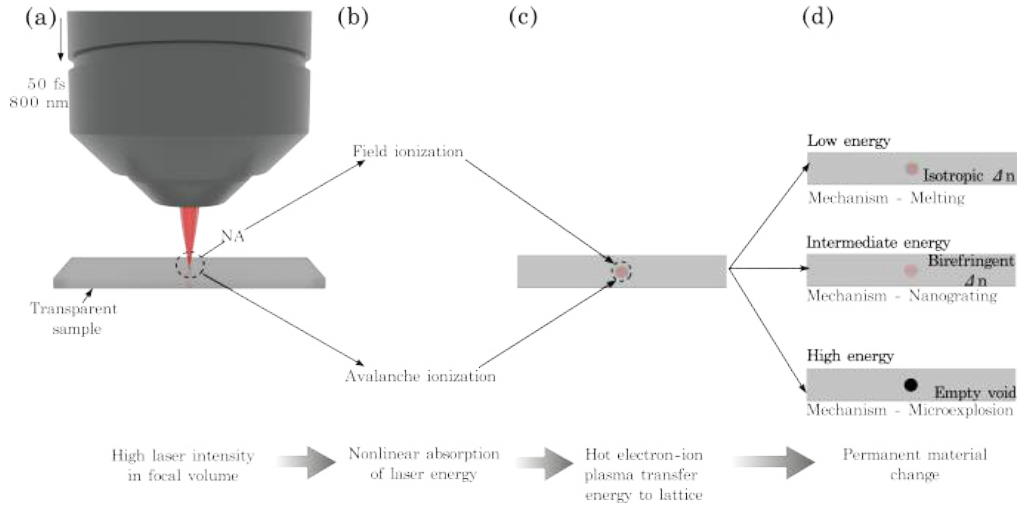


Figure 3.7: Depiction of the morphological changes produced by femtosecond laser irradiation: (a) When the laser is exposed to a femtosecond laser, there is a (b) nonlinear absorption leading to the creation of a free electron plasma through multiphoton ionization. This process is followed by an avalanche photoionization, resulting in the formation of a (c) hot electron plasma (d) leading to three distinct types of permanent modification.

For the creation of waveguides we sought an isotropic modification, where there exists a uniform modification in the *Refractive Index*, which is required for a low propagation loss. This is attainable for energy just above the threshold, that is the low energy. It is argued that modification of *Refractive Index* results in the formation of a darkening region in soda-lime after being exposed to a femtosecond laser. This darkening is caused by the absorption of light by mobile charge carriers, which then interact to create trapped hole centers [39] leading to a zone with negative RI change. While the bright zone indicates the positive change of the RI (see Fig. 3.8) [40].

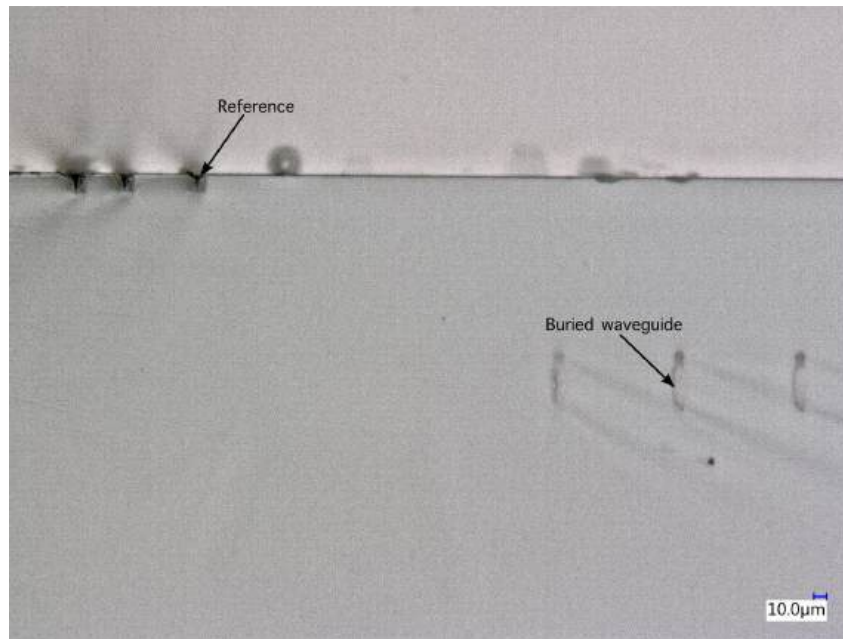


Figure 3.8: Example of fabrication of buried waveguides. The darker zones indicate the negative  $\Delta n$  contrast and the bright zone indicates the positive  $\Delta n$  contrast (waveguide).

## 3.2 Fabrication methodology for buried waveguides

Now we proceed to explain the key steps and considerations in the procedure to obtain straight buried waveguides on the soda-lime substrate at the CIO.

### 3.2.1 Substrate preparation

This research used a *microscopic slide of soda-lime glass* that is commercially available. The composition of soda-lime made by *Corning glass* is 73%  $SiO_2$  + 14%  $Na_2O$  + 7%  $CaO$  + 4%  $MgO$  + 2%  $Al_2O_3$  [41]. These microscope slides have dimensions of 75 mm  $\times$  25 mm and a thickness of 1.1 mm [42]. We cut the substrates and polish the side faces to achieve the substrates depicted in Fig. 3.14. The cutting and polishing processes were performed in the CIO's optic workshop, obtaining two substrates with the dimensions shown in Fig. 3.14.

### 3.2.2 Steps for making a waveguide

**Step one (Design):** The waveguide geometry was designed using AutoCAD (at the coordinate origin), where the waveguide size was specified, and a .DXF file was generated. Then, this .DXF file was converted to a compatible format (.cvs file) with the micromachining station program used by the .DXF converter software. In our case, we draw a straight line with a size greater than the width of the substrate  $L$  (see Fig. 3.13) to make sure that the laser irradiates the entire substrate.

**Step two (Find edge):** The substrate is placed as shown in Fig. 3.9, with the *Microscope Objective* at a distance that focuses on the surface of the substrate.

1. Using the microfabrication workstation software, *Newport Laser Microfabrication, version 4.9.9*, we proceed to find the top border on the substrate as shown in Fig. 3.10.
2. Stand in a corner and open the shutter with power at 2%.

**Step three (Z-correction):**

1. Find the bottom edge and save the coordinates to  $P0$ .
2. Save the second point at  $P1$  after focusing the damage caused by the laser on the lower edge (see Fig. 3.11).
3. Find the right edge, open the shutter and make a small point of damage, focus and save the coordinates at  $P2$  (see Fig. 3.12).

**Step four (Fabrication):**

1. Load into the microstation software the .DXL file.
2. Determine the number of repetitions and the distance between each one.

The fabrication for  $NA=0.40$  consisted of buried waveguides that exhibited variations in the depth of focus. These variations were  $50\mu m$ ,  $150\mu m$ ,  $250\mu m$ . Each set of buried waveguides, consisting of three waveguides, had the same scan speed and energy. The energy and scan speed varied across sets, increasing from  $2\mu J$  to  $3\mu J$  and

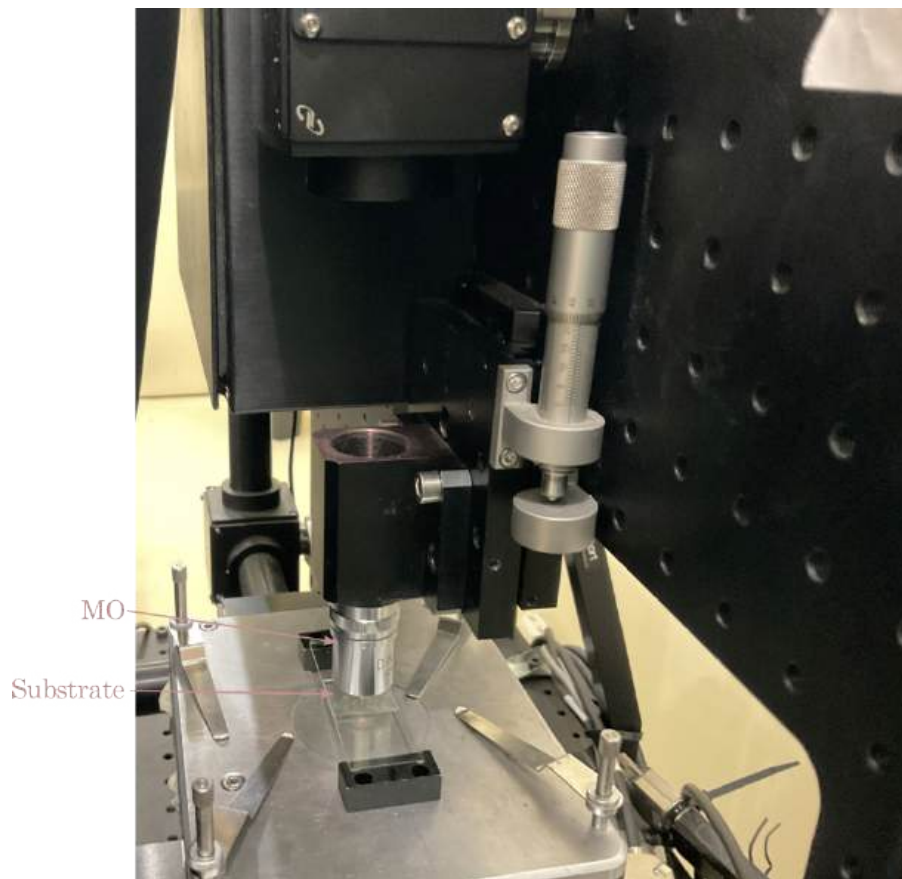


Figure 3.9: Picture of the focus of the MO on the surface of the substrate.

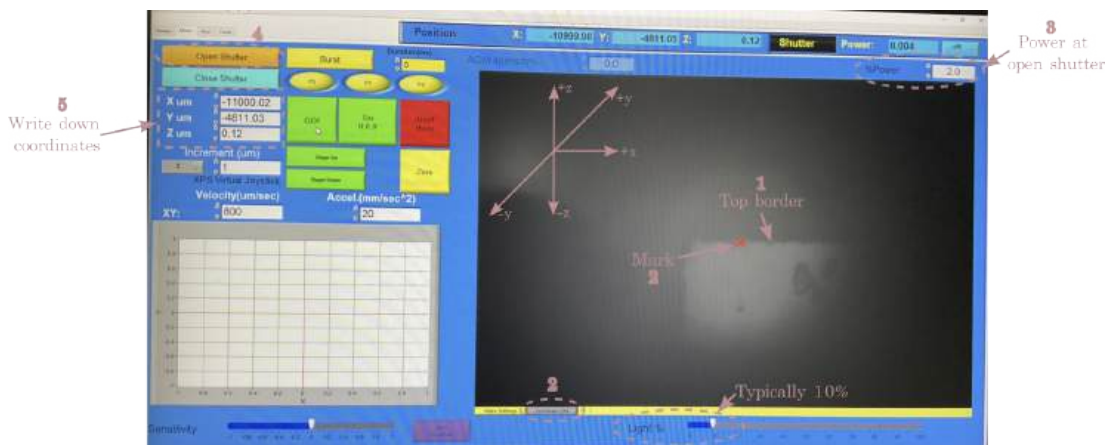


Figure 3.10: Image of the steps described to find the top edge.

from  $100\mu\text{m}/\text{s}$  to  $600\mu\text{m}/\text{s}$  for the writing speed. The manufacturing process of these buried waveguides involved the use of a microscope objective with a magnification of

### Chapter 3. Femtosecond-written waveguide fabrication



Figure 3.11: Image of the steps described to find the bottom edge.

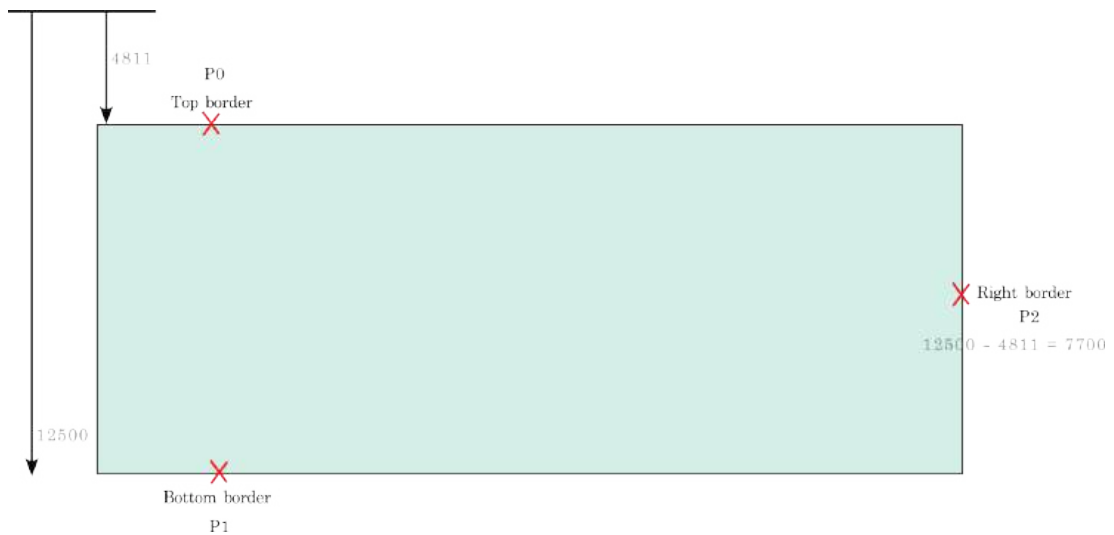


Figure 3.12: Example of the location of the  $P_0$ ,  $P_1$ ,  $P_2$  points.

20 $\times$ , which is equivalent to a numerical aperture (NA) of 0.40 [43]. For NA=0.65 each set of buried waveguides had three waveguides with the same scan speed and energy and using only one depth ( $50\mu\text{m}$ ). Across sets, the energy and scan speed increased from  $2\mu\text{J}$  to  $3\mu\text{J}$  and from  $100\mu\text{m/s}$  to  $600\mu\text{m/s}$ . Each set was separated by a surface line as indicated in Fig. 3.14. After considering the aforementioned modifications, we obtained a total of 54 buried waveguides for energy levels of  $2\mu\text{J}$ , and  $3\mu\text{J}$  at different depths of focus and scan speeds for NA=0.40. Similarly, for NA=0.65, we achieved

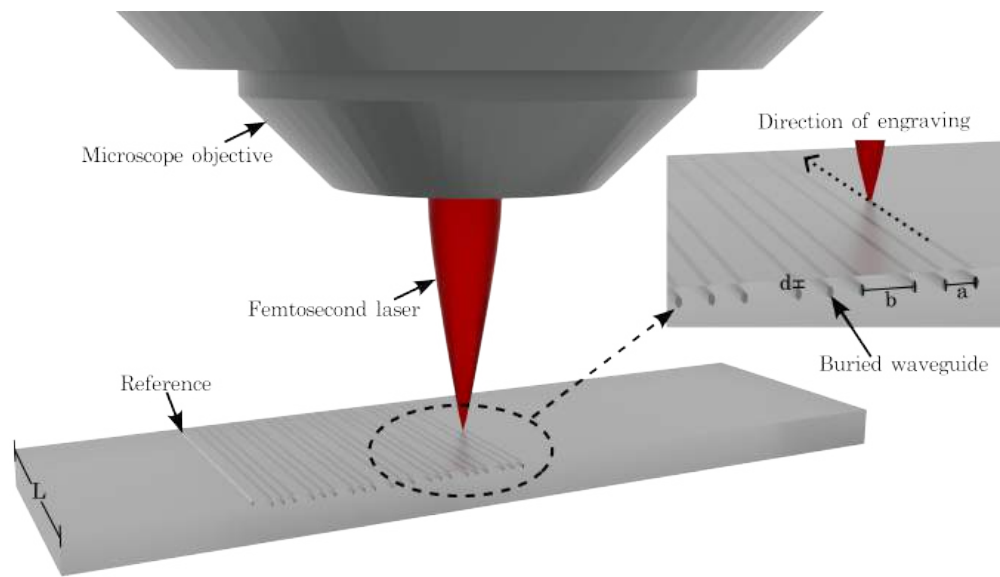
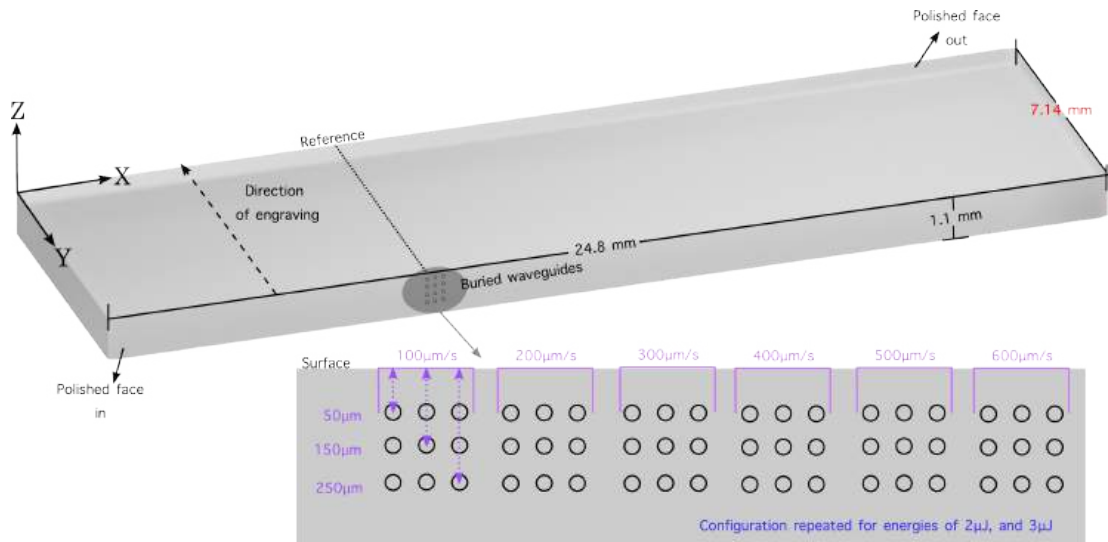


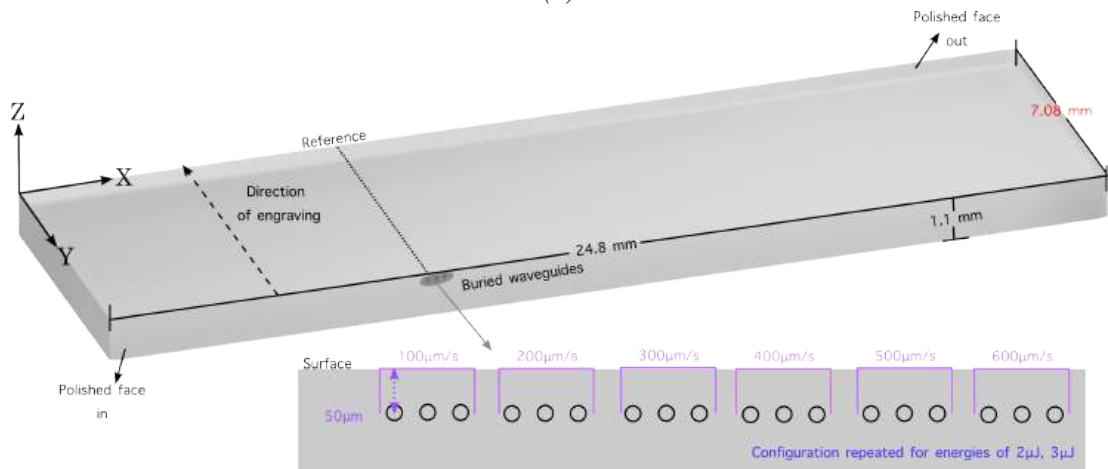
Figure 3.13: Illustration of the technique known as femtosecond laser writing (FDLW) for fabricating optical buried waveguides. The diagram includes variables such as  $a$ , which represents the separation between waveguides,  $b$ , which denotes the distance from each set of three waveguides, and  $d$ , which indicates the distance from the top surface.

36 buried waveguides for energy levels of  $2\mu J$ , and  $3\mu J$  at  $100\mu m/s$  to  $600\mu m/s$  scan speed.

Chapter 3. Femtosecond-written waveguide fabrication



(a)



(b)

Figure 3.14: Substrates employed in the fabrication of waveguide arrays positioned below the surface. (a)  $NA=0.40$  and (b)  $NA=0.65$ .

“If you can’t explain it simply, you don’t understand it well enough.”

Richard Feynman

# 4

## Techniques for refractive index measurement in buried waveguides

The *refractive index profile* of an optical waveguide is its most defining property. It directly determines the number of transverse modes supported by the waveguide and the properties of the modes [14]. Proper knowledge of the waveguide cross-section is essential for the later creation of integrated optical devices. This chapter describes the three experimental techniques proposed to measure the refractive index contrast of buried waveguides made by an ultrafast laser on a soda-lime substrate.

## 4.1 End-fire coupling techniques

### 4.1.1 Normalized frequency in a waveguide

As we know, the simplest waveguide consists of a higher RI surrounded by a material with a lower RI, known as a core and cladding, respectively. Any waveguide can support only a finite number of modes; some are propagated within it, and others are radiated.

The cross-section shape of a waveguide has a direct relation with the number of modes that a waveguide can transmit and, therefore, has a direct relationship between the field distribution of the guided modes and the cross-sectional refractive index profile of the waveguide [14].

The *normalized frequency*  $V$  is a parameter that allow us to estimate the number of guided modes:

$$V = \frac{2a\pi}{\lambda} \sqrt{n_1^2 - n_2^2} \quad (\text{Eq. 4.1})$$

where:

$V$  is the dimensionless normalized frequency of the waveguide.

$\lambda$  is the free space wavelength of the light.

$n_1$  is the RI of the core.

$n_2$  is the RI of the cladding.

$a$  is the radius of the core.

From Eq. 4.1, we can see that the number of modes supported by the waveguide decreases with the rise of  $\lambda$ . Also, a larger core means an increase in the value of  $V$ , or put in another way, a larger core supports more modes. Another way to increase the modes supported is increasing the value of the *refractive index contrast* ( $\Delta n$ ); this makes the waveguide more efficient at confining light within the core.

It is crucial to know that Eq. 4.1 is only obtained under the conditions of a step-index waveguide with a circular core and a normalized frequency ( $V < 2.405$ ) [14].

### Measure of the refractive index contrast $\Delta n$

We can obtain the RI of the core of the waveguide with the use of an alternative formula to calculate the number of modes that can be supported by a step-index optical waveguide [21]:

$$M \approx \frac{4}{\pi} \left( \frac{2a}{\lambda} \right)^2 \sqrt{n_1^2 - n_2^2} \quad (\text{Eq. 4.2})$$

where  $M$  is the approximate quantity of guided modes.

With  $V_c$  as a cut-off frequency and  $\lambda_c$  as a cut-off wavelength, we can find the conditions that determine if the waveguide is [14]:

Monomode:

$$V < V_c \quad \lambda > \lambda_c \quad (\text{Eq. 4.3})$$

Multimode:

$$V \geq V_c \quad \lambda \leq \lambda_c \quad (\text{Eq. 4.4})$$

where  $V_c$  and  $\lambda_c$  can be found from Eq. 4.1.

A vital parameter is  $\Delta n$ , defined as the difference between the substrate RI and the RI of the core. This positive change can be measured from the parameter  $V$ , we can obtain a relation from Eq. 4.1 and the equation proposed by Marcuse on [44] for a monomode, step-index waveguide:

$$\frac{w}{a} = 0.65 + \frac{1.619}{V^{3/2}} + \frac{2.879}{V^6} \quad (\text{Eq. 4.5})$$

with:

$a$  as the radius of the core.

$w$  as the radius of the guided mode.

We then need to find the appropriate value of  $V$  until the left side of the equation 4.5 is the same as the right. We must first measure the values of  $a$  and  $w$  to obtain this value. We can obtain the value of  $a$  from the pictures we take with the help of the microscope that we used to observe the fabricated waveguides. At the same time, we

can calculate the value of  $\omega$  from the picture of the mode that we take with the help of the slit profiler at  $\frac{1}{c^2}$ , with the condition that the beam has a Gaussian profile.

#### 4.1.2 Inverse Helmholtz equation

The *inverse Helmholtz equation technique* is a *Near Field* (NF) technique based on the measurement of the transmitted beam intensity near the guide facet, from which electric field intensity and index distribution can be calculated [45]. The NF method applies to a single-mode buried 3D waveguide with an elliptical shape.

An optical waveguide supports only a finite number of modes and any mode must be a solution of:

$$\nabla^2 \vec{E}(r) - \left( \frac{n(r)^2}{c^2} \right) \frac{\partial^2 \vec{E}(r)}{\partial t^2} = 0 \quad (\text{Eq. 4.6})$$

Which is known as Maxwell's wave equation.  $\vec{E}(r)$  is the electric field vector at some point  $r$ ,  $n(r)$  is the refractive index of the medium at that point, and  $c$  is the speed of light in a vacuum. Only in weakly guiding waveguides the mode can be thought as a plane wave traveling along the  $z - axis$ . Weakly guiding is defined by the maximum variation between the core and the cladding, typically less than  $\sim 1\%$ .

Thinking about the mode as a plane wave traveling along the  $z - axis$  with no dependency on  $z$ , from  $E(r)$ , we arrive at the scalar wave equation of the *Helmholtz equation* [14]:

$$\nabla^2 E(x, y) + [k^2 n^2(x, y) - \beta^2] E(x, y) = 0 \quad (\text{Eq. 4.7})$$

where  $\beta$  is a propagation constant.

The Eq. 4.6 illustrates the relationship between the field distribution of the guided modes and the refractive index. If the optical waveguide of interest is single mode, the *Helmholtz equation* can be used to determine its RI profile by measuring the near-field profile of the guided mode [14].

Rearranging the Helmholtz equation (Eq. 4.7), we obtain Eq. 4.8 for  $n^2(x, y)$ :

$$n^2(x, y) = n_b + \Delta n(x, y)^2 = n_{eff} - \frac{\lambda^2}{4\pi^2} \frac{\nabla^2 E(x, y)}{E(x, y)} \quad (\text{Eq. 4.8})$$

where  $n_{eff}$  is the effective index for the mode,  $n_b$  is the RI of the substrate and  $E(x, y)$  is the normalized E-field distribution across the mode. This field can be inferred by measuring the near-field intensity mode  $I(x, y)$  and using the relationship  $E(x, y) = \sqrt{I(x, y)}$ . Despite the fact that  $n_{eff}$  is an unknown constant, the RI difference profile  $\Delta n(x, y)$  is unaffected by the magnitude of  $n_{eff}$ . The RI difference profile can therefore be recovered by solving Eq. 4.8 using numerical methods [14].

## 4.2 Extrinsic Fabry-Pérot interferometer

Fibre optic sensors have some unique advantages over conventional electrical sensors, such as immunity to electromagnetic interference, corrosion resistance, and small size. Among a large number of fibre optic sensors, for example, fibre Bragg gratings (FBGs), long-period gratings, and various interferometric sensors, the *Fabry-Pérot Interferometer* (FPI) is especially advantageous in terms of fabrication complexity and cost of fabrication [46]. Since its first report by Fabry and Pérot, the FPI has played an important role in various optical fields. The FPI sensors can be classified into two categories, the *Intrinsic Fabry-Pérot Interferometer* (IFPI) and the *Extrinsic Fabry-Pérot Interferometer* (EFPI). In the case of the IFPI, the Fabry-Pérot cavity is formed between two fibre-in-line reflectors with a solid cavity (see Fig. 4.1a). As for the EFPI, it can be subdivided into those with one cavity and those with two cavities. The EFPI with one cavity has an external reflector placed at a certain distance away from the end facet of the optical fibre. The fibre and reflector can be attached to different structures to form a Fabry-Pérot cavity (see Fig. 4.1b [46]). As for the EFPI of the dual cavity, it consists of a reflective surface, from which we obtain the multiple reflections, as we can see in Fig. 4.1c to form the second cavity, instead of a non-reflective structure.

The configuration for a Fabry-Pérot interferometer made out of optical fibre in Fig. 4.1a is the simplest example of how any Fabry-Pérot interferometer works. The interference inside the structure is produced by the superposition of multiple beams

generated inside the cavity. For the analysis of the RI on the buried waveguides, an EFPI sensor is used in the configuration of two cavities. Here, we will proceed to explain how it works at a high level; for a deeper explanation, it can be reviewed in [47].

In Fig. 4.1c, we can see the serial configuration of a EFPI of dual-cavity. This type of optical sensor stands out because it is possible to measure more than one parameter with its structure simultaneously. The interfering light produces a modulated cosine signal, enabling simultaneous measurement of multiple parameters. In our setup, this includes the optical path in the air, within the waveguide (soda-lime substrate), and their combined path length. Using a Fast Fourier Transform (FFT), the modulated cosine signal (resulting from the alignment of the sensor with the fabricated waveguide) is represented in the frequency domain for the analysis. With knowledge of the optical path length (OPL) of the waveguide, which corresponds to the substrate's thickness, we can calculate the refractive index using the following equation.

$$n = \frac{OPL}{L_w} \quad (\text{Eq. 4.9})$$

where:

$L_w$  - physical length of the waveguide.

$n$  - refractive index of the waveguide.

It is important to mention that different configurations were used for the fabrication of the sensor, a *Single Mode Fiber* (SMF) (a simple EFPI, see Fig. 4.1c) and a *Multicore Fiber* (MCF) in a configuration of *extrinsic hybrid Fabry-Pérot interferometer* both for the calculation of the refractive index at the core and the cladding. The *extrinsic hybrid Fabry-Pérot interferometer* (Fig. 4.1d) works similarly as the simple *Extrinsic Fabry-Pérot Interferometer* of one cavity.

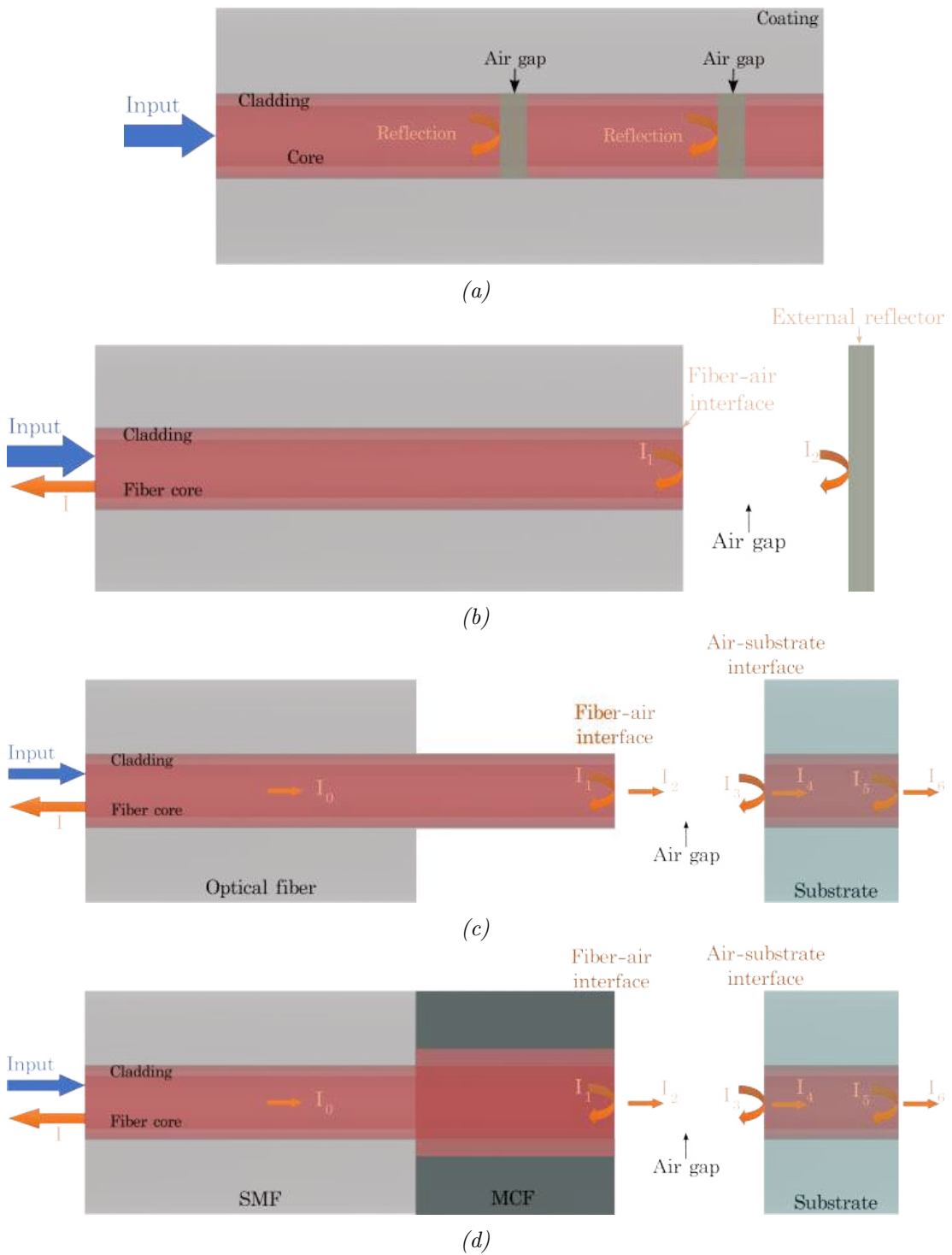


Figure 4.1: The diagram illustrates the operation of four types of fibre optics interferometers: (a) Intrinsic Fabry-Pérot Interferometer, (b) Extrinsic Fabry-Pérot Interferometer with one cavity, (c) EFPI with two cavities, (d) Extrinsic hybrid Fabry-Pérot interferometer.

*“The reason is, when there is a hard problem, one has to work a long time and has to be persistent. In order to be persistent, you have got to be convinced that it’s worthwhile working so hard, that you’re going to get somewhere.”*

Leonard Mlodinow, Feynman’s Rainbow: A Search for Beauty in Physics and in Life

# 5

## Results and discussion

This chapter details the fabrication results and the measurement of physical and optical attributes of buried waveguides made by the FDLW technique in soda-lime glass. It compares the results of the change of the refractive index obtained for the techniques reviewed in the previous chapter. It provides an interpretation and a discussion of these results based on different manufacturing parameters to establish the optimal parameters for high-quality waveguide fabrication and their generation of a symmetrical mode.

We selected three distinct techniques for calculating the RI, each with specific advantages. The normalized frequency technique, also called the “V parameter”, allows us to know if the waveguide is single-mode, has a step-like profile and is circular shaped. This provides us with insights into the symmetry of the mode, restricted by accurately measuring the radius of the mode and the physical dimensions of the waveguide core. The inverse Helmholtz technique serves as a powerful method for reconstructing the

index change in both two-dimensional (2D) and three-dimensional (3D) graphical representations, with the primary limitation being the quality of the mode picture employed. The success of this methodology is contingent upon precise system alignment, which is crucial for achieving accurate results. However, a notable drawback of this technique is the necessity of applying a filter to mitigate noise present in the mode data, which can impact the overall effectiveness of the reconstruction process.

Finally, using the extrinsic Fabry-Pérot sensor, we can measure the refractive index change at both the core and cladding of the waveguide. The measurement at the core is done using the configuration shown in Fig. 4.1c, while the measurement at the cladding uses the configuration in Fig. 4.1d. As an optical interferometric sensor, one of the main drawbacks is the requirement for precise alignment of the system to ensure accurate data collection. This alignment is crucial because the sensor's position directly influences the measurements obtained. Given the small size of the waveguides, ensuring proper positioning at the core can be particularly challenging.

We present our findings using tables and graphs that illustrate how the refractive index varies with writing speed and between them with the use of different energies. We compare the advantages and disadvantages of the different techniques employed to calculate the refractive index contrast. It is essential to select and standardize the waveguide fabrication parameters (i.e. numerical aperture (NA), depth of focus, energy and writing speed) to achieve an approximation to a specific value of refractive index in soda-lime material. This process should ensure repeatability with a step-like index profile, minimize dark zones (negative index), create an isotropic bright zone (positive index), and establish a smooth contrast index. Additionally, the design should feature a symmetrical mode and minimize ellipticity in the physical geometry, all of which are crucial for the effective design of photonic devices.

The present chapter follows the next structure. First, we show the arrangement used to characterize the buried waveguides by capturing pictures of the modes for the different fabricated waveguides, which are presented along with the calculation of their radii. Then, we used electronic microscopes of different resolutions to measure the physical radii sizes of the waveguide. Ultimately, we present the calculated data for the

refractive index contrast using the techniques in the previous chapter and compare the results by interpretation.

To conclude, we present the calculation data of the insertion loss. This measurement is taken from the power transmitted through the waveguide, specifically between a coupling single-mode fibre (SMF) at the entrance of the buried waveguide and the focus of a MO at the output side. The measured power is then compared to the power propagated at the output facet of the optical fibre (SMF).

## 5.1 Near-field mode characterization

### 5.1.1 Experimental arrangement

The experimental setup shown in Fig. 5.1 was designed to visualize the modes of the fabricated waveguides through a slit beam profiler. Thus, we can determine if the buried waveguide is monomode or multimode based on the image by observing the quantity of the modes visualized and if it exhibits stable mode confinement and propagation characteristics by observing the shape of the mode.

The optical system for characterization consists of two stages: *aligning* and *visualization*. On the *aligning* part, we have two piezoelectric actuators, an electronic microscope, a XYZ platform for a SMF fibre at the entrance of the waveguide, and one XY platform to move the sample. Then, on the *visualization* part, we have another XYZ platform for a MO of NA=0.40, an iris diaphragm to filter the noise, and a scanning-slit optical beam profiler to visualize the field corresponding to the mode (see Fig. 5.1).

The MO amplifies the mode at the output of the waveguide to improve the visualization, with a working distance of 160mm where we positioned a scanning-slit optical beam profiler connected to a laptop which allows us to capture images and real-time visualization of the waveguide modes. The iris diaphragm is positioned between the profiler and the MO to filter the light, allowing only the mode-containing light to pass through.

We utilized piezoelectric actuators mounted on XYZ platforms to enhance the align-

ment. This arrangement provides us with the flexibility to make meticulous horizontal adjustments between the optical fibre (or the MO) and the buried waveguide by making fine vertical tweaks to guarantee the best transmission of the output light. Also, we employed an electronic microscope to determine the optical fibre's position relative to the substrate to focus the waveguide we wanted to see relative to the surface reference, see Fig. 5.2.

We used a *Thorlabs 4-Channel fibre-Coupled Laser Source (MCLS1)* [48] at  $\lambda = 1550nm$  for the characterization because of the wide use of this wavelength on optical sensors.

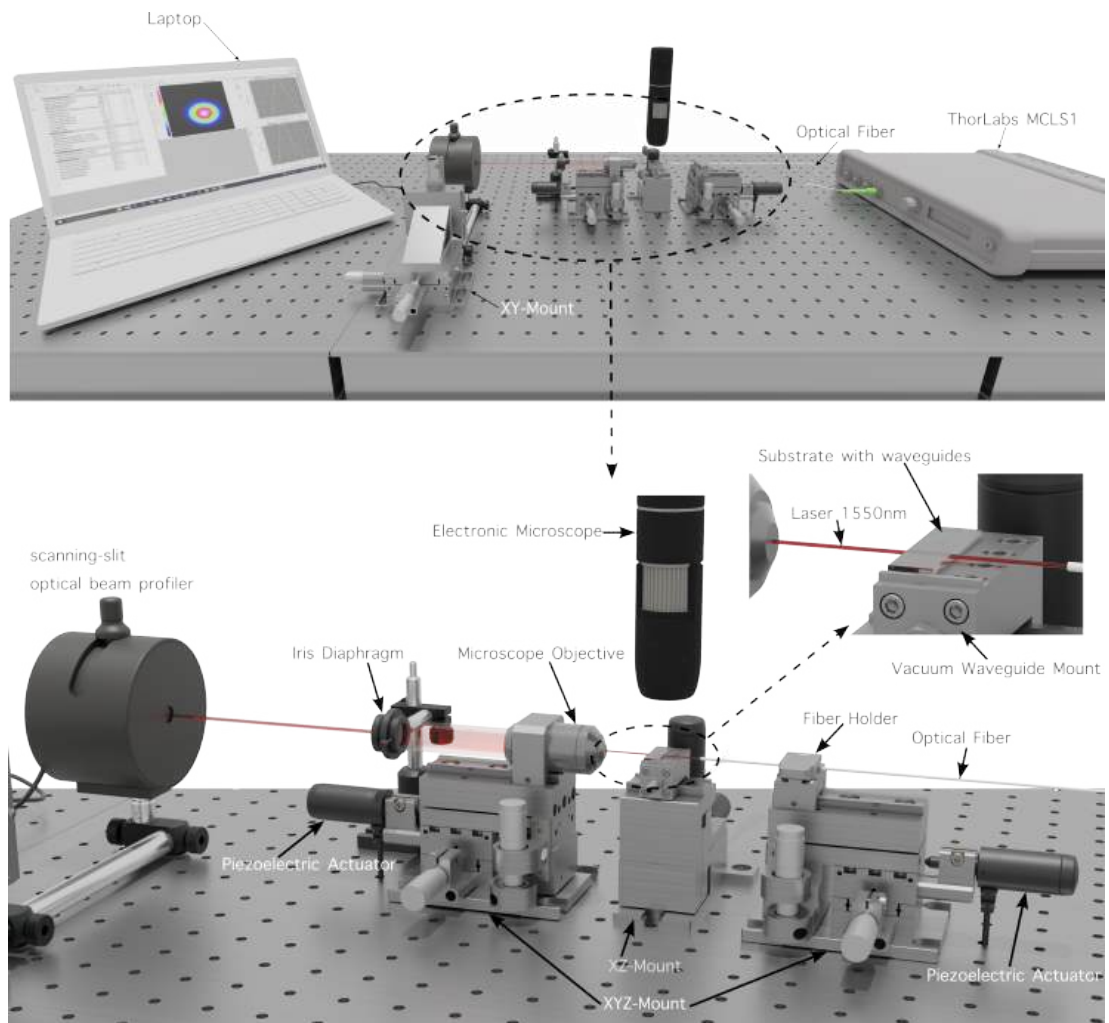


Figure 5.1: Experimental setup for the analysis of the optical characteristics of buried waveguides.

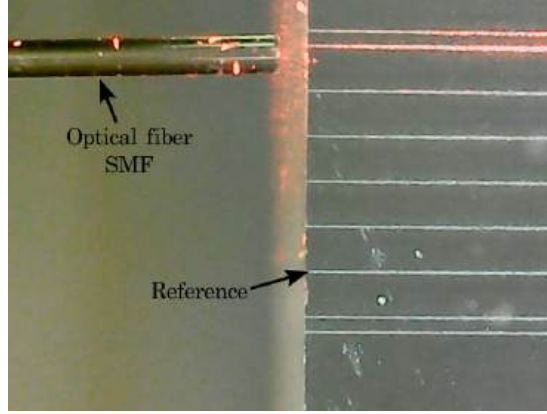


Figure 5.2: Example of the alignment of the optical fibre with chosen waveguide through the surface reference.

To conduct our measurements, we first set the *Thorlabs MCLS1* to a wavelength of  $\lambda = 640nm$  to visualize the optimal transmission through the waveguide, which appears as a bright red point. Next, we align the system vertically at the required depth ( $50\mu m$ ,  $150\mu m$  and  $250\mu m$ ). After achieving vertical alignment, we adjust the system horizontally to pinpoint the location of the maximum intensity. Once a clear red point is visible, we switch the light source to  $\lambda = 1550nm$ , and use a slit beam profiler program on our laptop to observe the mode. We make precise adjustments with the piezoelectric actuators to the visualized mode, and upon achieving the maximum intensity value, we record the corresponding data for the waveguide. From Fig. 5.3 to Fig. 5.8, we present the profiles of transverse modes for fabrication parameters with  $NA=0.40$  at energy levels of  $2\mu J$  and  $3\mu J$  for different depths ( $50\mu m$ ,  $150\mu m$ , and  $250\mu m$ ). For the case of  $NA = 0.65$  at energies of  $2\mu J$  and  $3\mu J$ , the analysis is only conducted for a depth of  $50\mu m$  (Fig. 5.9 and 5.10).

The primary objective of this work was to compare the calculated value of the refractive index change of buried waveguides by three different techniques with different numerical apertures (0.40 and 0.65) at the same depth of focus  $50\mu m$  and the same energy  $3\mu J$  but different writing speed ( $100-600\mu m/s$ ). However, the research was later extended to investigate the behavior of the refractive index contrast at greater depths (specifically  $150\mu m$  and  $250\mu m$ ) and lower energy  $2\mu J$ . Given the promising results previously presented (referenced in [26] and [49]) for buried waveguides as optical devices,

we decided to also explore the results at these additional depths and energy. Thus, the data for NA=0.40 at  $150\mu m$ ,  $250\mu m$ , and for the  $2\mu J$  are included as supplementary insights, while the main focus remains on the results for  $50\mu m$  at the energy of  $3\mu J$  for both numerical apertures (0.40 and 0.65). That said, the fabrication of those extra buried waveguides was limited by the function of the laser of fabrication, meaning that for NA=0.65, we only obtained buried waveguides at  $50\mu m$  of depth.

## 5.2 Mode analysis and comparison of buried waveguides

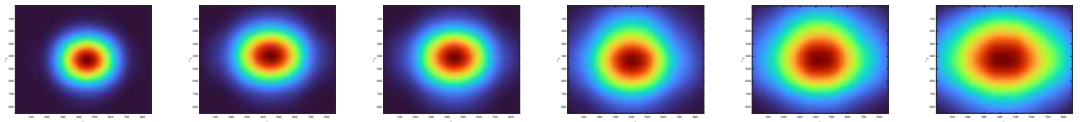
A mode analysis is essential for understanding and characterizing the modes present in a given optical system. This analysis provides insights into the field distribution within the waveguide, which directly influences its performance in terms of light confinement, transmission efficiency, and overall behavior, whether monomode or multimode.

A single-mode regime is crucial because devices such as Mach-Zehnder interferometer-based sensors rely on the optical interaction between the modal field and the variable of interest, as well as the interference pattern that is produced as a result [49]. The effective confinement is also an essential variable because if light results improve in transmittance, that means a reduction in propagation losses, allowing us to see more defined modes that could present symmetrical mode field distributions. This is directly translated into good-quality waveguide characteristics that can be used in the fabrication of an optical integrated sensor.

From Fig. 5.3 to 5.8, we present the transverse mode profile fields of each buried waveguide created under different setup conditions. We observe notable single-mode behavior, characterized by minimal dispersion for the writing speeds of  $100\mu m/s$  to  $300\mu m/s$  at NA=0.40 for both energies of fabrication of  $2\mu J$  and  $3\mu J$  for a depth of  $50\mu m$ . Being the most defined modes those made by  $3\mu J$  of energy. For waveguides produced with a NA=0.65 (Fig. 5.9 to 5.10), there is a significant enhancement in the symmetry of the mode profile, along with a reduction in the size of the modes of the waveguides fabricated at  $3\mu J$  across all writing speeds.

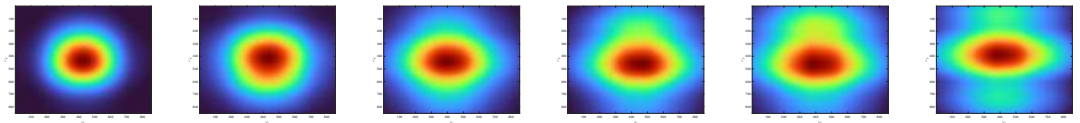
The waveguides made at  $150\mu m$  and  $250\mu m$  for both energies have a poorly defined

mode. This worsens for a lower NA and higher writing speeds, which may lead to inadequate energy deposition and an anisotropic change at the focused area. Therefore, it is recommended to work with NA values equals or greater than 0.40 to achieve isotropic changes at depths greater than  $50\mu m$ , and writing speeds around  $100\mu m/s$  to  $300\mu m/s$ . The apparent multimode behavior in waveguides at depths of  $150\mu m$  and  $250\mu m$  is attributed to the spherical aberration. This aberration, along with self-focusing and nonlinear absorption, typically lead to the formation of an asymmetrical structure and a non-uniform refractive index distribution within the waveguide. This can result in an asymmetrical mode field pattern for the guided light [40].



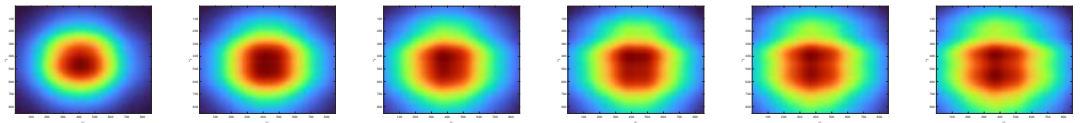
(a)  $100\mu m/s$ . (b)  $200\mu m/s$ . (c)  $300\mu m/s$ . (d)  $400\mu m/s$ . (e)  $500\mu m/s$ . (f)  $600\mu m/s$ .

Figure 5.3: Modes of the buried waveguides at a depth= $50\mu m$  with an energy= $2\mu J$  and  $NA=0.40$ .



(a)  $100\mu m/s$ . (b)  $200\mu m/s$ . (c)  $300\mu m/s$ . (d)  $400\mu m/s$ . (e)  $500\mu m/s$ . (f)  $600\mu m/s$ .

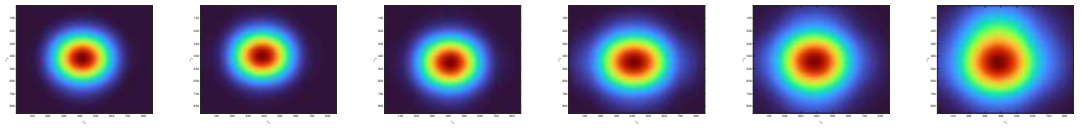
Figure 5.4: Modes of the buried waveguides at a depth= $150\mu m$  with an energy= $2\mu J$  and  $NA=0.40$ .



(a)  $100\mu m/s$ . (b)  $200\mu m/s$ . (c)  $300\mu m/s$ . (d)  $400\mu m/s$ . (e)  $500\mu m/s$ . (f)  $600\mu m/s$ .

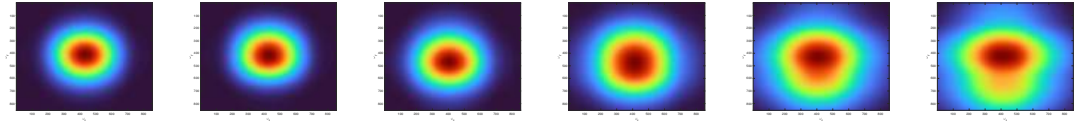
Figure 5.5: Modes of the buried waveguides at a depth= $250\mu m$  with an energy= $2\mu J$  and  $NA=0.40$ .

Chapter 5. Results and discussion



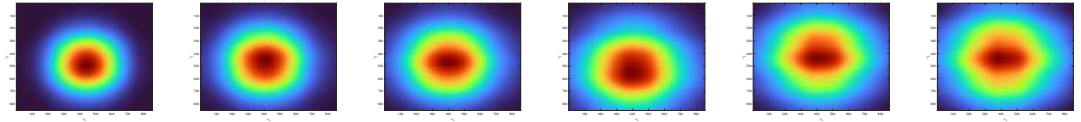
(a)  $100\mu\text{m/s}$ . (b)  $200\mu\text{m/s}$ . (c)  $300\mu\text{m/s}$ . (d)  $400\mu\text{m/s}$ . (e)  $500\mu\text{m/s}$ . (f)  $600\mu\text{m/s}$ .

Figure 5.6: Modes of the buried waveguides at a depth= $50\mu\text{m}$  with an energy= $3\mu\text{J}$  and  $NA=0.40$ .



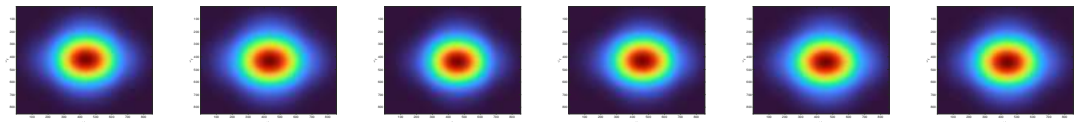
(a)  $100\mu\text{m/s}$ . (b)  $200\mu\text{m/s}$ . (c)  $300\mu\text{m/s}$ . (d)  $400\mu\text{m/s}$ . (e)  $500\mu\text{m/s}$ . (f)  $600\mu\text{m/s}$ .

Figure 5.7: Modes of the buried waveguides at a depth= $150\mu\text{m}$  with an energy= $3\mu\text{J}$  and  $NA=0.40$ .



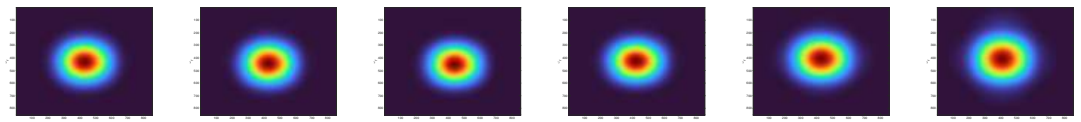
(a)  $100\mu\text{m/s}$ . (b)  $200\mu\text{m/s}$ . (c)  $300\mu\text{m/s}$ . (d)  $400\mu\text{m/s}$ . (e)  $500\mu\text{m/s}$ . (f)  $600\mu\text{m/s}$ .

Figure 5.8: Modes of the buried waveguides at a depth= $250\mu\text{m}$  with an energy= $3\mu\text{J}$  and  $NA=0.40$ .



(a)  $100\mu\text{m/s}$ . (b)  $200\mu\text{m/s}$ . (c)  $300\mu\text{m/s}$ . (d)  $400\mu\text{m/s}$ . (e)  $500\mu\text{m/s}$ . (f)  $600\mu\text{m/s}$ .

Figure 5.9: Modes of the buried waveguides at a depth= $50\mu\text{m}$  with an energy= $2\mu\text{J}$  and  $NA=0.65$ .



(a)  $100\mu\text{m/s}$ . (b)  $200\mu\text{m/s}$ . (c)  $300\mu\text{m/s}$ . (d)  $400\mu\text{m/s}$ . (e)  $500\mu\text{m/s}$ . (f)  $600\mu\text{m/s}$ .

Figure 5.10: Modes of the buried waveguides at a depth= $50\mu\text{m}$  with an energy= $3\mu\text{J}$  and  $NA=0.65$ .

### 5.2.1 Mode size of the waveguides

We determined the mode size radius of the buried waveguides at  $1/e^2$  using the X and Y profile data of the transversal mode and calculating the pixel size. The pixel size was derived from the dimensions of the captured profile data. We then applied the following formula:

$$px = \frac{p}{(num_{px})(magnification)}$$

where:

$px$  - Value equivalent of each pixel.

$p$  - The sum of the values of the first and last positions across the entire dataset of the intensity profile, it represents the value in micrometers (-x to +x).

$num_{px}$  - Number of pixels of the picture, this could be seen on the information of the picture, here we obtain a picture of 853x853.

$magnification$  - 20x for the visualization of the mode.

We calculated the average value of the mode radii obtained in X and Y, which is shown in Tables 5.1 to 5.8. We can see from the tables that the mode size increases with fabrication depth (Fig. 5.11 to 5.13). This occurs because dispersion also increases due to non-uniform material modification; as the writing speed increases, it prevents the material from being modified uniformly. From this, we can infer that the optimal fabrication depth is  $50\mu m$ , as it has the least light dispersion and the lowest deformation of the laser beam at the focus within the material, from the smaller size of the transversal mode. Moreover, this is true for both fabrication energies  $2\mu J$  and  $3\mu J$  for the NA=0.40 (Tables 5.1, 5.2, 5.5 and 5.6). Between these two energies of fabrication, the best is  $3\mu J$  because it presents the smaller size for the mode relative to a better light confinement. Following the same analysis as before, we can see from Tables 5.3, 5.4, 5.7 and 5.8 for NA=0.65, that the best confinement exist on the waveguides made with  $3\mu J$  of energy.

Writing speed $\mu m/s$	50 $\mu m$	150 $\mu m$	250 $\mu m$
100	8.956	10.064	11.947
200	9.832	11.296	12.946
300	9.956	12.226	13.388
400	10.544	13.760	13.388
500	11.497	13.574	14.806
600	15.674	12.435	14.922

Table 5.1: Average horizontal mode field radius ( $\omega_x$  [ $\mu m$ ]),  $NA=0.40$ , energy= $2\mu J$

Writing speed $\mu m/s$	50 $\mu m$	150 $\mu m$	250 $\mu m$
100	8.979	9.669	12.249
200	9.622	12.226	12.970
300	9.948	8.251	15.131
400	12.954	7.670	15.131
500	14.736	14.783	14.945
600	14.271	11.942	14.713

Table 5.2: Average vertical mode field radius ( $\omega_y$  [ $\mu m$ ]),  $NA=0.40$ , energy= $2\mu J$ .

Writing speed $\mu m/s$	50 $\mu m$
100	8.002
200	11.498
300	13.273
400	14.846
500	29.108
600	27.505

Table 5.3: Average horizontal mode field radius ( $\omega_x$  [ $\mu m$ ]),  $NA=0.65$ , energy= $2\mu J$ .

Writing speed $\mu m/s$	50 $\mu m$
100	8.495
200	12.277
300	14.098
400	15.261
500	29.545
600	28.066

Table 5.4: Average vertical mode field radius ( $\omega_y$  [ $\mu m$ ]),  $NA=0.65$ , energy= $2\mu J$ .

Writing speed $\mu m/s$	50 $\mu m$	150 $\mu m$	250 $\mu m$
100	8.646	9.359	10.335
200	8.956	9.677	11.195
300	9.142	10.142	12.063
400	9.405	11.164	12.830
500	10.056	11.924	12.993
600	11.257	12.458	12.900

Table 5.5: Average horizontal mode field radius ( $\omega_x$  [ $\mu m$ ]),  $NA=0.40$ , energy= $3\mu J$

Writing speed $\mu m/s$	50 $\mu m$	150 $\mu m$	250 $\mu m$
100	8.545	9.932	10.366
200	8.731	10.227	12.404
300	9.134	9.832	12.923
400	9.560	13.659	13.644
500	10.893	13.574	13.899
600	12.768	15.271	14.759

Table 5.6: Average vertical mode field radius ( $\omega_y$  [ $\mu m$ ]),  $NA=0.40$ , energy= $3\mu J$ .

Writing speed $\mu m/s$	50 $\mu m$
100	6.122
200	9.790
300	8.883
400	14.260
500	16.785
600	19.657

Table 5.7: Average horizontal mode field radius ( $\omega_x$  [ $\mu m$ ]),  $NA=0.65$ , energy= $3\mu J$ .

Writing speed $\mu m/s$	50 $\mu m$
100	7.037
200	10.573
300	9.345
400	14.618
500	17.097
600	20.245

Table 5.8: Average vertical mode field radius ( $\omega_y$  [ $\mu m$ ]),  $NA=0.65$ , energy= $3\mu J$ .

## Chapter 5. Results and discussion

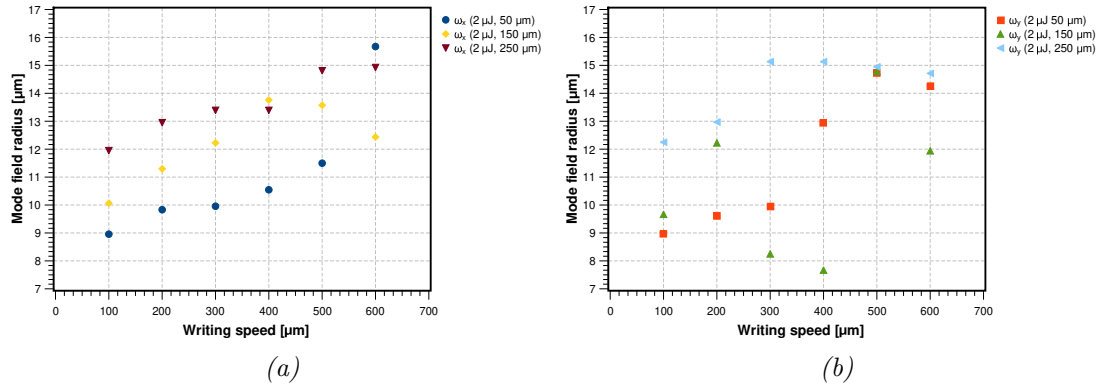


Figure 5.11: Average mode field radius (a) horizontal ( $\omega_x$  [ $\mu\text{m}$ ]) and (b) vertical ( $\omega_y$  [ $\mu\text{m}$ ]) of the waveguides fabricated at  $50\mu\text{m}$ ,  $150\mu\text{m}$  and  $250\mu\text{m}$  within the substrate,  $NA=0.40$  at energy= $2\mu\text{J}$ .

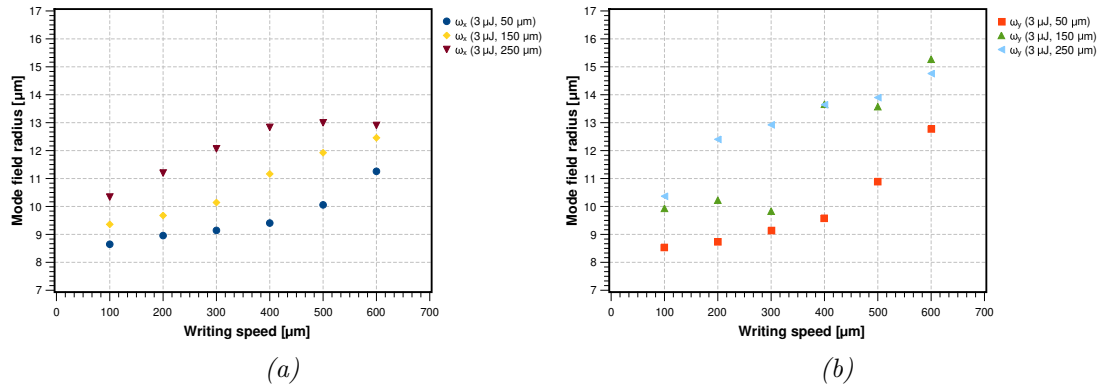


Figure 5.12: Average mode field radius (a) horizontal ( $\omega_x$  [ $\mu\text{m}$ ]) and (b) vertical ( $\omega_y$  [ $\mu\text{m}$ ]) of the waveguides fabricated at  $50\mu\text{m}$ ,  $150\mu\text{m}$  and  $250\mu\text{m}$  within the substrate,  $NA=0.40$  at energy= $3\mu\text{J}$ .

From the graphs 5.11, 5.12 and 5.13, we can confirm a steady change for most setup parameters, especially at  $50\mu\text{m}$  of depth,  $3\mu\text{J}$  of energy, giving a positive tendency across all writing speeds.

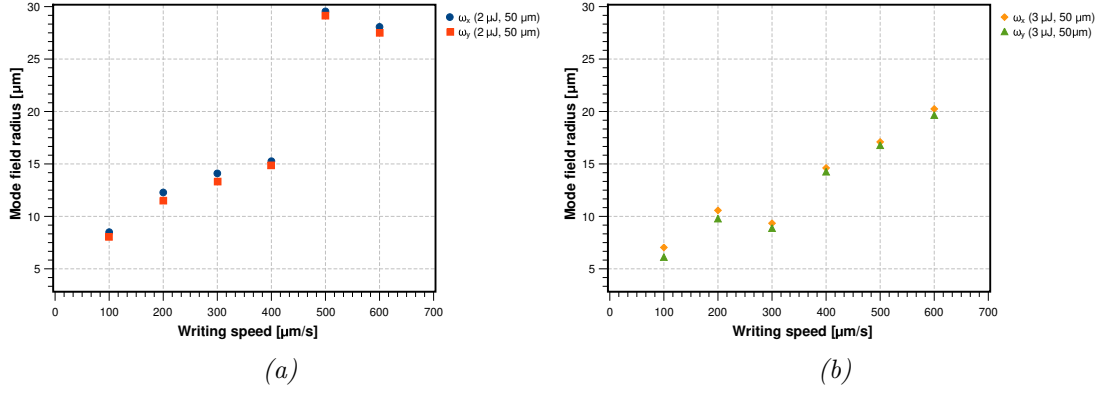


Figure 5.13: Average mode field radius of the waveguides horizontal ( $\omega_x$  [ $\mu\text{m}$ ]) and vertical ( $\omega_y$  [ $\mu\text{m}$ ]) fabricated at  $50\mu\text{m}$  within the substrate,  $NA=0.65$  at energies of (a)  $2\mu\text{J}$  and (b)  $3\mu\text{J}$ .

### 5.2.2 Physical size of the cross-section of the waveguides

Two distinct methods were employed to determine the dimensions of the buried waveguides made by both numerical apertures ( $NA=0.40$  and  $NA=0.65$ ). In the case of the waveguides made by  $NA=0.40$ , a software tool is utilized that allows us to specify the size per pixel (*Tracker 6.0 from Physlet Physics* [50]), enabling us to quantify the waveguide dimensions based on the images shown in Fig. 5.14.

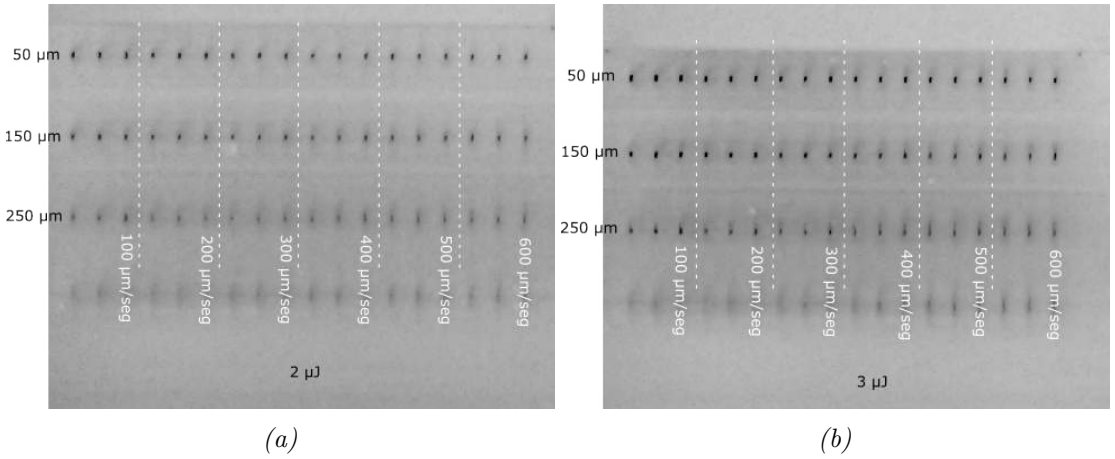


Figure 5.14: Cross-sections obtained from the waveguides made by  $NA=0.40$ , (a) energy= $2\mu\text{J}$ , (b) energy= $3\mu\text{J}$ .

To measure the waveguides made by  $NA=0.65$ , the features of the microscope Keyence were used, it was possible to automatically calculate the width and height

size of the waveguide selected using the pictures on Fig. 5.15 and 5.16.

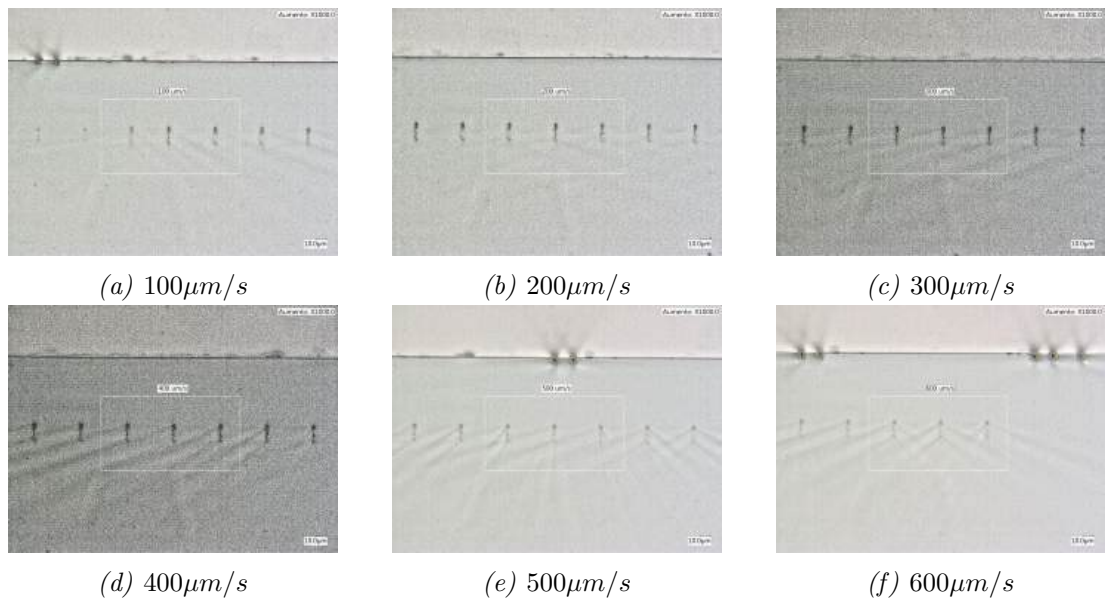


Figure 5.15: Cross-section images of the cross-sections of waveguides made by  $NA=0.65$  and  $energy=2\mu J$ .

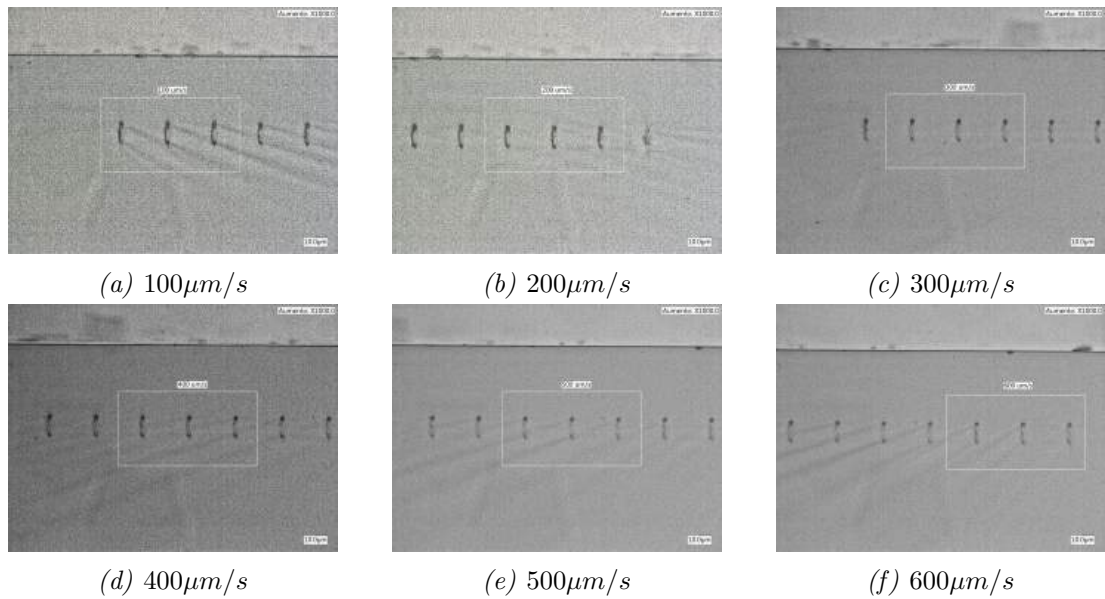


Figure 5.16: Cross-section images of the cross-sections of waveguides made by  $NA=0.65$  and  $energy=3\mu J$ .

From Table 5.9 to Table 5.16 we obtain the graphs at Fig. 5.18 and Fig. 5.19, we observe that the relationship between depth and waveguide size is inversely propor-

tional, with the smallest values occurring at  $50\mu m$  depth. As expected, the waveguide size is lower at  $2\mu J$  than at  $3\mu J$ . This difference arises because higher laser energy during fabrication results in greater area of modification on the substrate, leading to larger waveguides. This trend also holds for the waveguides created with  $NA=0.65$ .

Writing speed $\mu m/s$	50 $\mu m$	150 $\mu m$	250 $\mu m$
100	3.112	3.651	4.659
200	3.020	3.399	4.221
300	2.988	3.163	4.040
400	2.837	2.737	3.707
500	2.678	2.518	3.024
600	2.517	2.361	2.454

Table 5.9: Physical average radius ( $r_x$  [ $\mu m$ ]),  $NA=0.40$ , energy= $2\mu J$ .

Writing speed $\mu m/s$	50 $\mu m$	150 $\mu m$	250 $\mu m$
100	5.805	7.195	7.886
200	5.665	6.625	7.158
300	5.611	5.956	7.091
400	5.097	5.776	6.925
500	4.904	5.574	6.702
600	4.710	5.241	6.420

Table 5.10: Physical average radius ( $r_y$  [ $\mu m$ ]),  $NA=0.40$ , energy= $2\mu J$ .

Writing speed $\mu m/s$	50 $\mu m$
100	2.283
200	1.850
300	1.416
400	1.833
500	1.483
600	1.450

Table 5.11: Physical average radius ( $r_x$  [ $\mu m$ ]),  $NA=0.65$ , energy= $2\mu J$ .

Writing speed $\mu m/s$	50 $\mu m$
100	3.350
200	3.233
300	2.633
400	2.600
500	2.266
600	2.083

Table 5.12: Physical average radius ( $r_y$  [ $\mu m$ ]),  $NA=0.65$ , energy= $2\mu J$ .

Writing speed $\mu m/s$	50 $\mu m$	150 $\mu m$	250 $\mu m$
100	3.209	4.569	5.243
200	3.146	3.934	4.712
300	3.062	3.776	4.309
400	2.939	3.601	4.025
500	2.871	3.352	3.514
600	2.768	3.310	3.218

Table 5.13: Physical average radius ( $r_x$  [ $\mu m$ ]),  $NA=0.40$ , energy= $3\mu J$ .

Writing speed $\mu m/s$	50 $\mu m$	150 $\mu m$	250 $\mu m$
100	5.563	6.920	10.375
200	5.912	6.824	9.241
300	5.714	6.655	8.806
400	5.417	6.475	8.296
500	5.327	6.130	8.062
600	4.948	5.842	7.826

Table 5.14: Physical average radius ( $r_y$  [ $\mu m$ ]),  $NA=0.40$ , energy= $3\mu J$ .

Writing speed $\mu m/s$	50 $\mu m$
100	1.950
200	1.866
300	2.016
400	1.783
500	1.750
600	1.583

Table 5.15: Physical average radius ( $r_x$  [ $\mu m$ ]),  $NA=0.65$ , energy= $3\mu J$ .

Writing speed $\mu m/s$	50 $\mu m$
100	4.200
200	3.283
300	3.066
400	2.733
500	2.566
600	2.533

Table 5.16: Physical average radius ( $r_y$  [ $\mu m$ ]),  $NA=0.65$ , energy= $3\mu J$ .

The results presented in Tables 5.9 to 5.14 indicate that writing speeds of  $300\mu\text{m}/\text{s}$  and  $400\mu\text{m}/\text{s}$  for a numerical aperture  $\text{NA}=0.40$ , at a depth of  $50\mu\text{m}$ , resulted in waveguides that exhibit the least elliptical characteristics. This suggests a more rounded fundamental mode. In comparison, for a  $\text{NA}=0.65$ , the waveguides achieving a more circular configuration are those produced at writing speeds of  $400\mu\text{m}/\text{s}$  and  $500\mu\text{m}/\text{s}$  for both energy levels examined.

At the depths of  $150\mu\text{m}$  and  $250\mu\text{m}$ , the observed shape increasingly takes on an elliptical form. This behavior is attributed to the non-uniform variation of optical properties in the region where the laser beam focuses, a phenomenon influenced by spherical aberrations. These aberrations result in an uneven distribution of energy, leading to the deformation in shape as depth increases.

The analysis of the graphs presented in Fig. 5.17 and 5.18 reveals a consistent decreasing trend in values across varying writing speeds, with the maximum value observed at a speed of  $100\mu\text{m}/\text{s}$  and the minimum at  $600\mu\text{m}/\text{s}$ . This trend is consistent across all the experimental setups. The data indicate that the smallest waveguide exhibits a depth of  $50\mu\text{m}$ , which increases with the profundity of focus. Similarly, an increase in energy from  $2\mu\text{J}$  to  $3\mu\text{J}$  correlates with an increase in the size of the fabricated structures. Consequently, the optimal fabrication parameters for both NA were determined to be a depth of  $50\mu\text{m}$  with an energy setting of  $3\mu\text{J}$ .

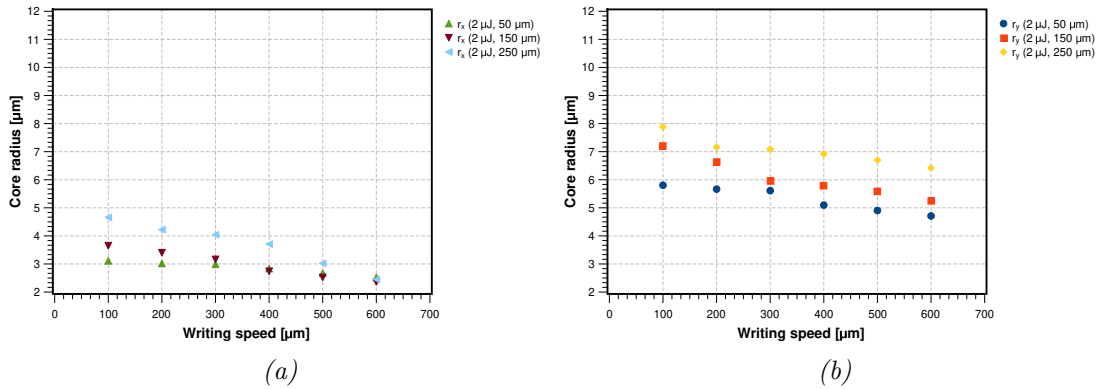


Figure 5.17: Physical average size of the cross-section of the waveguides fabricated at  $50\mu\text{m}$ ,  $150\mu\text{m}$  and  $250\mu\text{m}$  within the substrate,  $\text{NA}=0.40$  at energy= $2\mu\text{J}$ , (a) horizontal radius ( $r_x$  [ $\mu\text{m}$ ]), (b) vertical radius ( $r_y$  [ $\mu\text{m}$ ]).

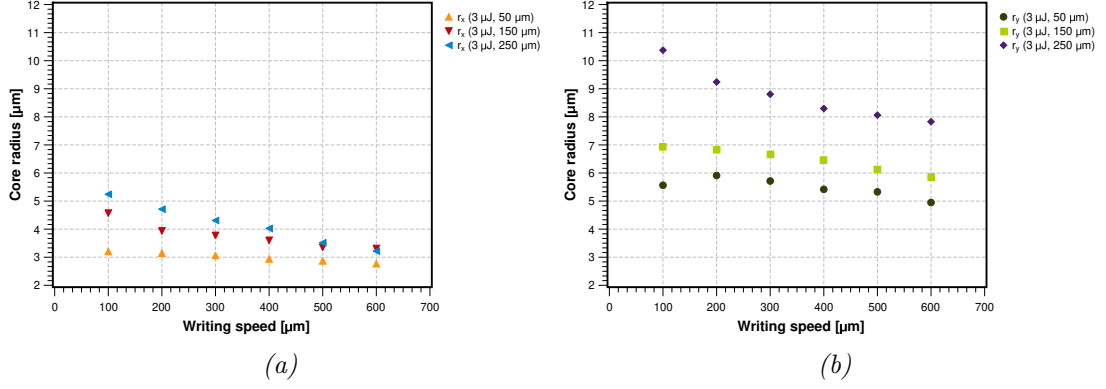


Figure 5.18: Comparison of the physical size of waveguides fabricated at  $50\mu\text{m}$ ,  $150\mu\text{m}$  and  $250\mu\text{m}$  within the substrate, for  $NA=0.40$  at  $\text{energy}=3\mu\text{J}$ , (a) horizontal radius ( $r_x$  [ $\mu\text{m}$ ]), (b) vertical radius ( $r_y$  [ $\mu\text{m}$ ]).

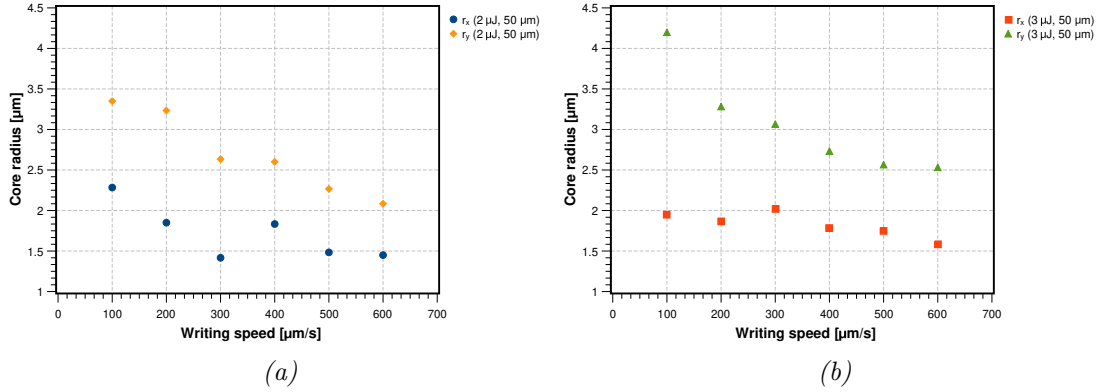


Figure 5.19: Comparison of the physical average horizontal radius ( $r_x$  [ $\mu\text{m}$ ]) and vertical radius ( $r_y$  [ $\mu\text{m}$ ]), of waveguides fabricated at  $50\mu\text{m}$  within the substrate, for  $NA=0.65$ , (a)  $\text{energy}=2\mu\text{J}$ , (b)  $\text{energy}=3\mu\text{J}$ .

### 5.3 Core-cladding index change calculation using the normalized frequency technique

As explained in the previous chapter, the V parameter determines the number of modes that can propagate within a waveguide. This is because it depends on the core and cladding indices: if the difference between these indices ( $\Delta n$ ) is large, the V parameter increases, which can allow the propagation of more than one mode due to improved confinement within the waveguide.

The relationship between the physical size of a waveguide and the V parameter

is characterized by a linear correspondence. As the physical size of the waveguide increases, the  $V$  parameter similarly increases, facilitating the propagation of additional modes when  $V > 2.405$ . This observation underscores the significance of the waveguide's geometry in influencing light confinement and mode propagation within the structure.

It is also relevant to mention that for smaller wavelengths ( $\lambda$ ), the  $V$  parameter increases. This means that for the same waveguide geometry, the number of allowed modes varies with the wavelength. Here, for  $\lambda = 1550nm$ , we aim to find the optimal geometry and therefore the best fabrication parameters to achieve a more homogeneous RI change region for the fundamental mode. This is crucial for creating optical devices sensors that operate at this wavelength, minimizing losses and enhancing bandwidth.

This technique can be used to calculate  $\Delta n$  by relating the physical size of the waveguide to the mode size. By calculating this ratio and setting a tolerance, we can iteratively apply the Marcuse equation to obtain an experimental value for the  $V$  parameter. With this value, we can then approximate  $\Delta n$ .

The approximated  $\Delta n$  values obtained from this method for the core-cladding index change are detailed in Tables 5.17, 5.18 (NA=0.40) and Table 5.19 (NA=0.65).

<b>Writing speed [<math>\mu m/s</math>]</b>	<b>50 <math>\mu m</math></b>	<b>150 <math>\mu m</math></b>	<b>250 <math>\mu m</math></b>
100	4.121	3.458	2.932
200	3.954	3.170	2.826
300	3.918	3.667	2.772
400	3.809	3.757	2.865
500	3.666	3.112	2.981
600	3.665	2.999	3.256

*Table 5.17: Calculated values of  $\Delta n$  obtained for NA=0.40 at an energy of  $2\mu J$  using the  $V$  parameter technique. The values of  $\Delta n$  are on a scale of  $\times 10^{-3}$ .*

Writing speed [ $\mu\text{m}/\text{s}$ ]	50 $\mu\text{m}$	150 $\mu\text{m}$	250 $\mu\text{m}$
100	4.158	3.924	3.401
200	4.110	3.866	3.263
300	4.077	3.964	3.180
400	4.040	3.696	3.136
500	3.918	3.478	3.179
600	3.771	3.433	3.266

Table 5.18: Calculated values of  $\Delta n$  obtained for  $NA=0.40$  at an energy of  $3\mu\text{J}$  using the  $V$  parameter technique. The values of  $\Delta n$  are on a scale of  $\times 10^{-3}$ .

Writing speed [ $\mu\text{m}/\text{s}$ ]	2 $\mu\text{J}$	3 $\mu\text{J}$
100	5.226	5.607
200	4.799	4.831
300	5.220	5.035
400	4.692	4.491
500	-	4.379
600	-	5.087

Table 5.19: Calculated values of  $\Delta n$  obtained for  $NA=0.65$  at the depth of focus  $50\mu\text{m}$  using the  $V$  parameter technique. The values of  $\Delta n$  are on a scale of  $\times 10^{-3}$ .

In the analysis presented, we explore the effects of various fabrication depths on the refractive index change in waveguides fabricated with specific pulse energy levels and numerical apertures. The results illustrated in Fig. 5.20 confirm that the fabrication depth of  $50\mu\text{m}$  has the most consistent results with a negative slope for both energies across all values of writing speed, with a higher contrast at  $3\mu\text{J}$ , confirming the effectiveness of the waveguide fabrication technique with minimal induced damage. The behaviour at higher depths confirms the non-homogeneous changes in the substrate.

For the case of  $NA=0.65$  (Fig. 5.21) the maximum observed  $\Delta n$  reaches  $5.2 \times 10^{-3}$ , with a minimum of  $4.3 \times 10^{-3}$ . These elevated refractive index changes can be attributed to the increased energy attained at higher magnifications (higher  $NA$ ), despite this improvement poses a risk of introducing microfractures that could adversely affect the waveguide's integrity, leading to elevated losses.

The methodology employed in this study can be characterized as a numerical approach, necessitating accuracy in measuring mode size and waveguide dimensions to achieve reliable results. This is exemplified by our inability to obtain usable values for

## Chapter 5. Results and discussion

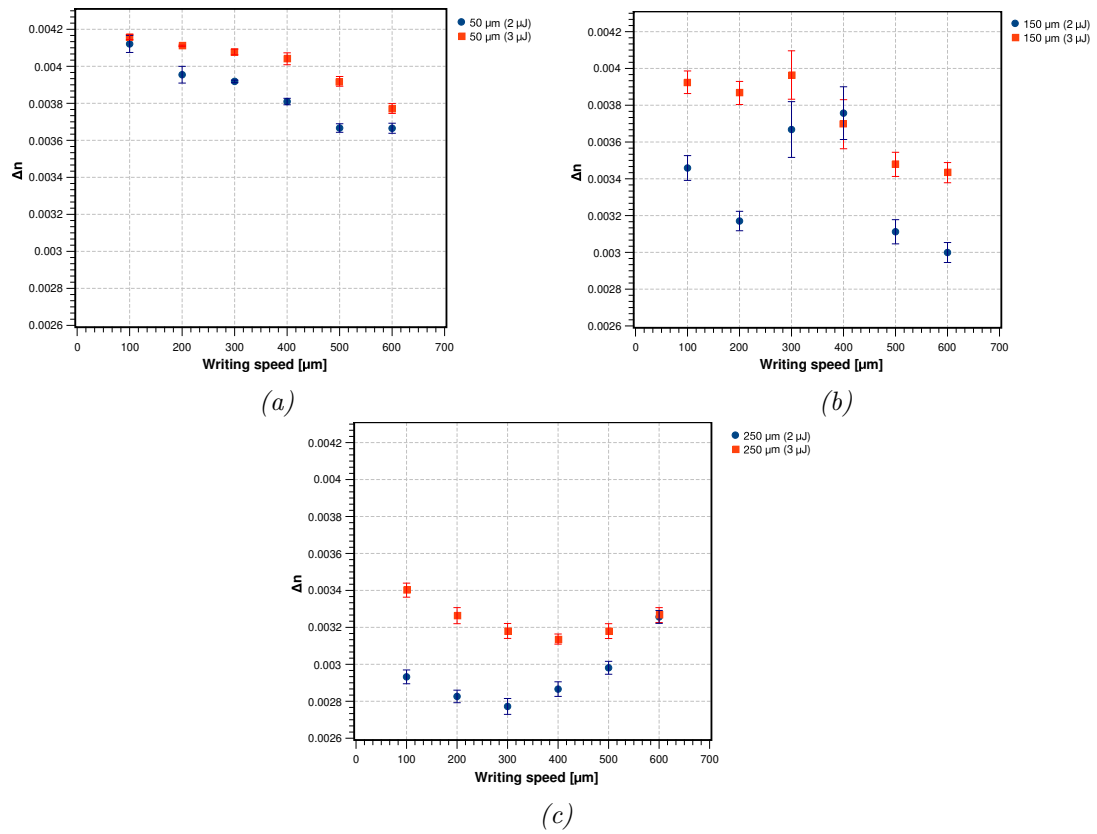


Figure 5.20: Comparison of  $\Delta n$  at different energies of fabrication,  $NA=0.40$  and depth of focus (a)  $50\mu\text{m}$ , (b)  $150\mu\text{m}$  and (c)  $250\mu\text{m}$ .

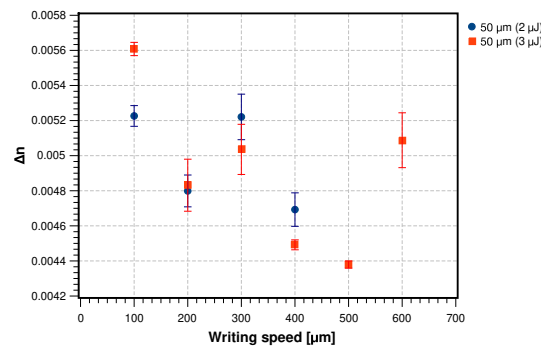


Figure 5.21: Comparison of  $\Delta n$  for different energies of fabrication at  $NA=0.65$  and  $depth=50\mu\text{m}$ .

$NA=0.65$  with a pulse energy of  $2\mu\text{J}$  at writing speeds of  $500\mu\text{m}/\text{s}$  and  $600\mu\text{m}/\text{s}$ . The analysis underscores the importance of maintaining a specific ratio (of a monomode and step-like waveguide, i.e.  $V < 2.405$ ) between these parameters to ensure that the

waveguide operates as a single mode with a normalized frequency. Also, we highlight the fact that this technique works only for step-index single-mode waveguides with a circular core, that is the more asymmetrical the waveguide is the less probable is that we can calculate the core-cladding index change.

## 5.4 Core-cladding index change calculation using the inverse Helmholtz technique

The principal outcome of this technique is the ability to reconstruct the index change profile and its distribution utilizing exclusively the mode image. This calculation is realized through the application of the inverse Helmholtz equation.

In Figure 5.22, we present the index change profiles and corresponding values obtained via this technique for waveguides fabricated with a numerical aperture  $NA=0.40$  at an input energy of  $2\mu J$ . In contrast, Fig. 5.23 illustrates the results for identical  $NA$  at an increased input energy of  $3\mu J$ . The profile obtained through this method exhibits characteristics similar to a step profile. Therefore, we can assert that the approximation derived from the  $V$  parameter in the previous section is valid.

In this analysis, we compute the approximated index change value by calculating the value at the center of the profiles. The resulting data can be found in Table 5.20, corresponding to an input energy of  $2\mu J$ , and in Table 5.21 for an input energy of  $3\mu J$ , both with a  $NA$  of 0.40. Figure 5.22b clearly illustrates the step profile-like form for writing speeds ranging from  $100\mu m/s$  to  $300\mu m/s$ . However, this shape is lost at higher writing speeds ( $400-600\mu m/s$ ) due to the poor confinement of light in these waveguides. Despite this, a decreasing correlation between the index change ( $\Delta n$ ) and the writing speed is maintained.

As the fabrication depth increases, the waveguides that retain a step-like profile at a depth of  $250\mu m$  are only effective at the two initial speeds ( $100 - 200\mu m/s$ ), becoming ineffective beyond this depth. Nevertheless, the observed decreasing relationship persists across all fabrication depths.

We observe at  $NA=0.40$  for  $3\mu J$  a more square-like index profile, which would be

Writing speed [ $\mu\text{m}/\text{s}$ ]	50 $\mu\text{m}$	150 $\mu\text{m}$	250 $\mu\text{m}$
100	4.201	3.285	2.050
200	3.429	2.678	1.325
300	2.496	1.932	1.193
400	2.371	1.432	1.465
500	2.077	1.006	0.977
600	1.695	1.144	0.924

Table 5.20: Calculated values of  $\Delta n$  obtained for  $NA=0.40$  at an energy of  $2\mu\text{J}$  using the Helmholtz technique. The values of  $\Delta n$  are on a scale of  $\times 10^{-3}$ .

Writing speed [ $\mu\text{m}/\text{s}$ ]	50 $\mu\text{m}$	150 $\mu\text{m}$	250 $\mu\text{m}$
100	4.147	5.219	2.744
200	1.807	3.037	2.438
300	3.426	2.484	2.000
400	3.054	2.294	1.568
500	2.604	2.242	1.469
600	2.084	1.043	1.124

Table 5.21: Calculated values of  $\Delta n$  obtained for  $NA=0.40$  at an energy of  $3\mu\text{J}$  using the Helmholtz technique. The values of  $\Delta n$  are on a scale of  $\times 10^{-3}$ .

Writing speed [ $\mu\text{m}/\text{s}$ ]	2 $\mu\text{J}$	3 $\mu\text{J}$
100	3.453	5.289
200	3.108	5.330
300	3.563	5.534
400	3.184	5.070
500	3.012	4.761
600	3.261	2.366

Table 5.22: Calculated values of  $\Delta n$  obtained for  $NA=0.65$  at the depth of focus  $50\mu\text{m}$  using the Helmholtz technique. The values of  $\Delta n$  are on a scale of  $\times 10^{-3}$ .

characterized by a reduction in the central value of  $\Delta n$ , as demonstrated in Fig. 5.23a, 5.23c, and 5.23e. However, contrary to our expectations, the  $\Delta n$  pattern displays a nonlinear decreasing trend because the waveguides presented some damage.

Utilizing this technique, we are able to analyze the integrity of waveguides during the fabrication process, identifying damage produced by various factors. A predominant cause of such damage is identified as microfractures, which may arise from the inherent material properties or from the non-homogeneous generation of refractive index changes, often due to the presence of impurities within the material and high energy

## Chapter 5. Results and discussion

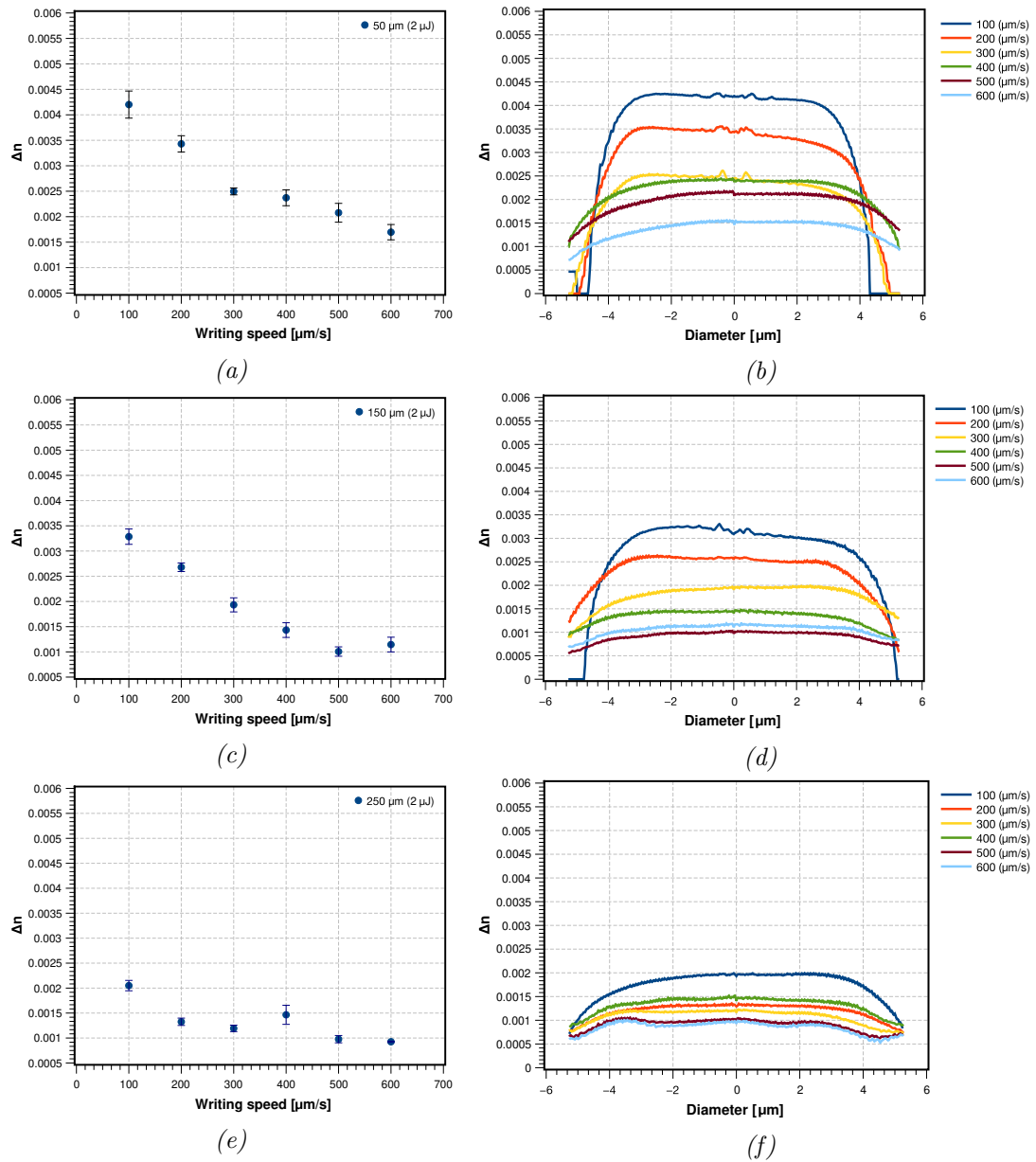


Figure 5.22: (a), (c), (e) Core-cladding index contrast ( $\Delta n$ ) and (b), (d), (f) refractive index profiles for  $NA=0.40$  at an energy of  $2\mu\text{J}$ , with depths of focus of  $50\mu\text{m}$ ,  $150\mu\text{m}$ , and  $250\mu\text{m}$ .

levels.

The observed core-cladding change in the focused area by an energy of  $3\mu\text{J}$  exceeds that produced by an energy input of  $2\mu\text{J}$ , accompanied by a corresponding increase in the mode size. This behavior aligns with theoretical expectations; specifically, the

## Chapter 5. Results and discussion

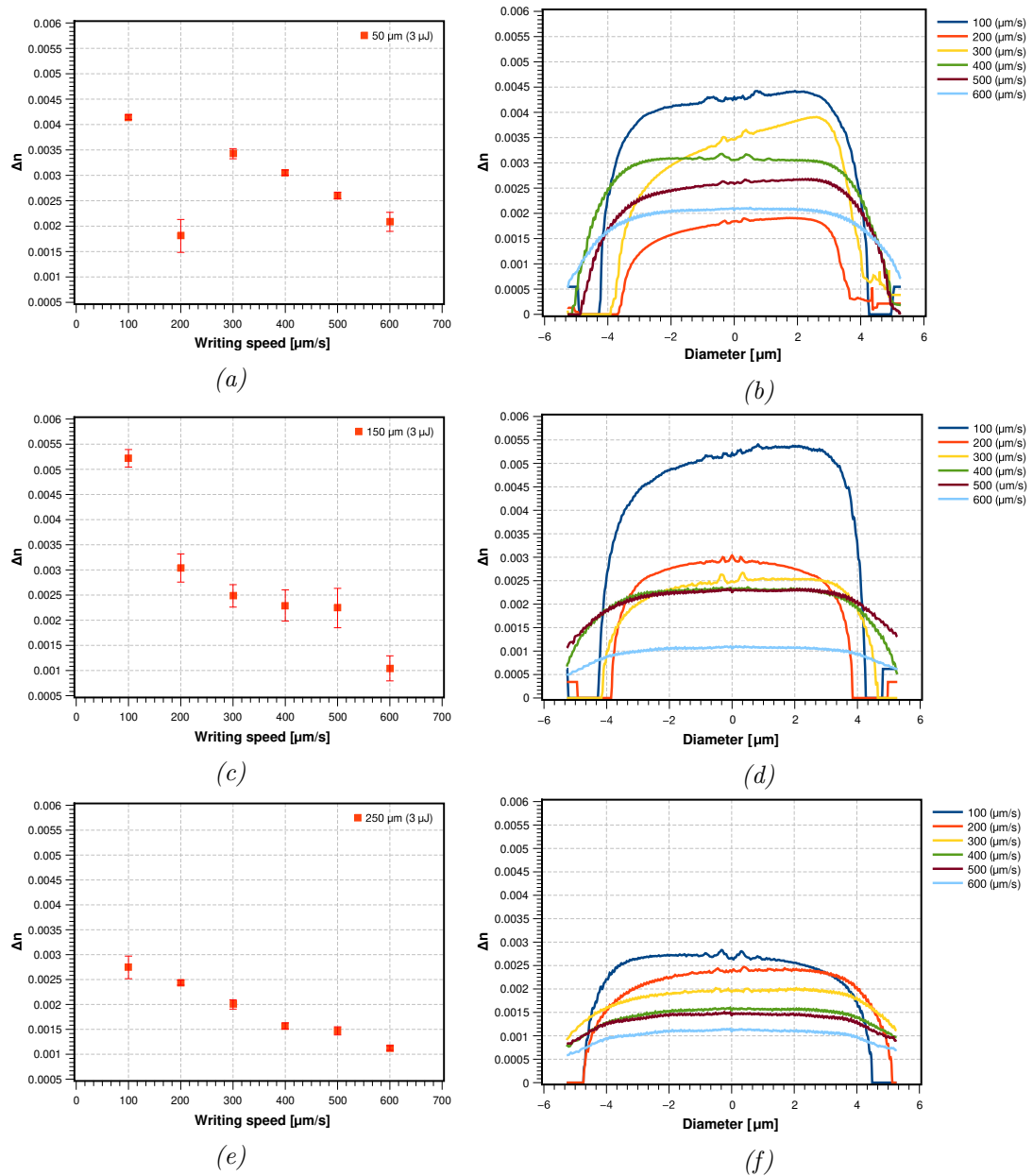


Figure 5.23: (a), (c), (e) Core-cladding index contrast ( $\Delta n$ ) and (b), (d), (f) refractive index profiles for  $NA=0.40$  at an energy of  $3\mu\text{J}$ , with depths of focus of  $50\mu\text{m}$ ,  $150\mu\text{m}$ , and  $250\mu\text{m}$ .

introduction of increased energy into the laser beam during the fabrication process leads to an expanded incidence area. This expansion fosters the formation of a more homogeneous waveguide and enhances light confinement. However, as illustrated in figures 5.23, this does not necessarily correlate with an optimal change in the refractive

## Chapter 5. Results and discussion

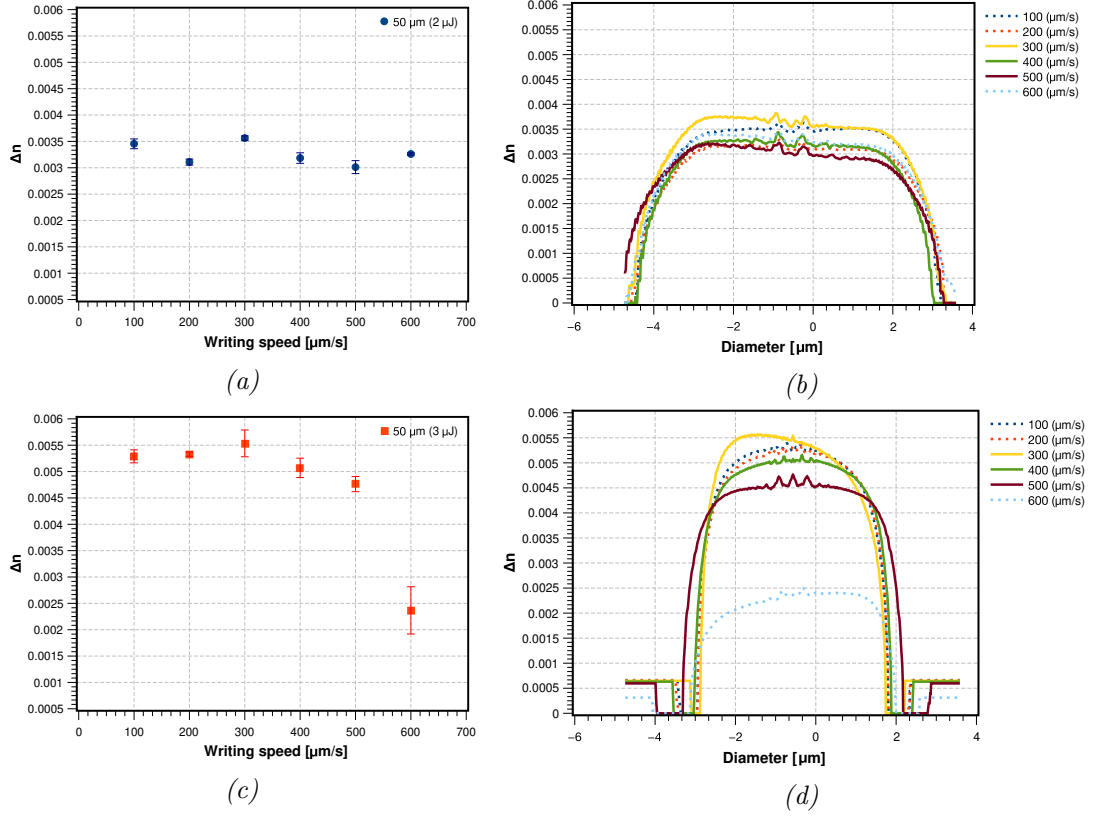


Figure 5.24: (a), (c) Core-cladding index contrast ( $\Delta n$ ) and (b), (d) refractive index profiles for  $NA=0.65$ , with depths of focus of  $50\mu\text{m}$  and energies of  $2\mu\text{J}$  and  $3\mu\text{J}$ .

index. Notably, the profiles exhibit asymmetry, with improved performance observed at writing speeds within the range of  $100\text{-}300\ \mu\text{m/s}$ . Nevertheless, at a depth of  $250\mu\text{m}$ , the step-like profile continues to manifest for writing speeds between  $100\text{-}200\ \mu\text{m/s}$ .

A maximum change of the RI of  $\Delta n = 4.1 \times 10^{-3}$  and a minimum  $\Delta n = 2.8 \times 10^{-3}$  at  $2\mu\text{J}$  were obtained. As for  $3\mu\text{J}$ , the maximum is  $\Delta n = 4.1 \times 10^{-3}$  and the minimum  $\Delta n = 3.1 \times 10^{-3}$ . These values are smaller than those obtained by V parameter calculation. Because of the use of only one value as an input, this can reduce the error in the calculation, depending only on the error introduced by the experimental collecting data (transverse mode).

If we compare the values of  $\Delta n$  at the same energy but different depth of fabrication we find that at the greatest fabrication depth we have the smallest change. This makes sense because at this depth the waveguides have a more amorphous shape indicating

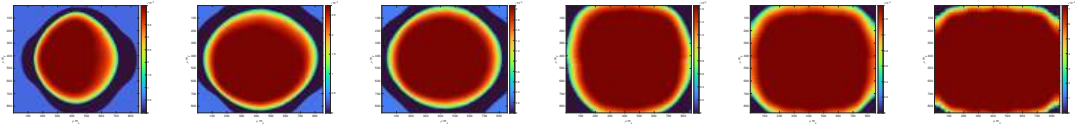
the bad distribution of the energy (spherical aberrations). In the same way at  $150\mu m$  of depth the value is smaller than at  $50\mu m$ . With a decreasing behavior at  $300 - 500\mu m/s$  for  $3\mu J$  and  $100 - 300\mu m/s$  for  $2\mu J$ .

With a similar analysis, from Fig. 5.24 we see a good decreasing behavior for  $300 - 500\mu m/s$ , this could be because of the increase in energy that is focused due the increase of the NA, so the best writing speed to create a smooth change index area is at  $300\mu m/s$  to  $500\mu m/s$ .

#### 5.4.1 2D Core-cladding index change distribution

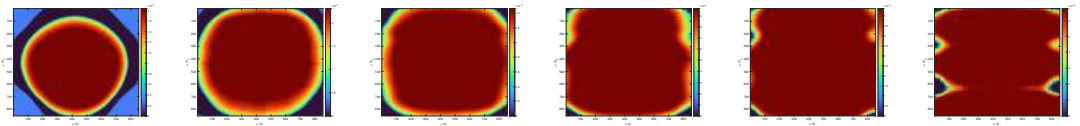
Fig. 5.25 to 5.32 show the core-cladding index change distribution on the buried waveguides. We have a stable index distribution for  $NA=0.40$  at  $100 - 300\mu m/s$  only for  $50\mu m$  of depth, for both energies, based on a more circular shape.

As for  $NA=0.65$  we can see a significant shape improvement at  $3\mu J$  comparing with  $2\mu J$ , but both present a good geometry, being the best for  $NA=0.65$  at  $400\mu m/s$  of writing speed for both energies, because it has the most circular shape.



(a)  $100\mu m/s$ . (b)  $200\mu m/s$ . (c)  $300\mu m/s$ . (d)  $400\mu m/s$ . (e)  $500\mu m/s$ . (f)  $600\mu m/s$ .

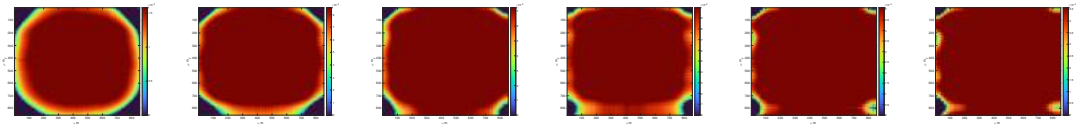
Figure 5.25: 2D index profile ( $\Delta n$ ) of the waveguides at depth= $50\mu m$ , energy= $2\mu J$ , with  $NA=0.40$ .



(a)  $100\mu m/s$ . (b)  $200\mu m/s$ . (c)  $300\mu m/s$ . (d)  $400\mu m/s$ . (e)  $500\mu m/s$ . (f)  $600\mu m/s$ .

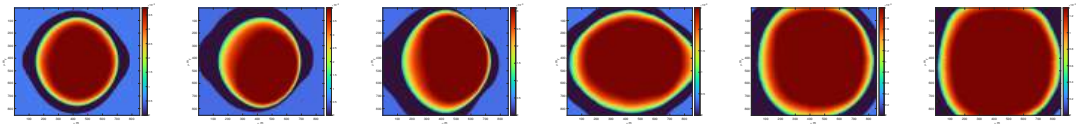
Figure 5.26: 2D index profile ( $\Delta n$ ) of the waveguides at depth= $150\mu m$ , energy= $2\mu J$ , with  $NA=0.40$ .

Chapter 5. Results and discussion



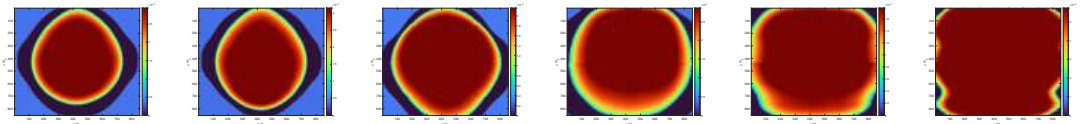
(a)  $100\mu\text{m/s}$ . (b)  $200\mu\text{m/s}$ . (c)  $300\mu\text{m/s}$ . (d)  $400\mu\text{m/s}$ . (e)  $500\mu\text{m/s}$ . (f)  $600\mu\text{m/s}$ .

Figure 5.27: 2D index profile ( $\Delta n$ ) of the waveguides at depth= $250\mu\text{m}$ , energy= $2\mu\text{J}$ , with  $NA=0.40$ .



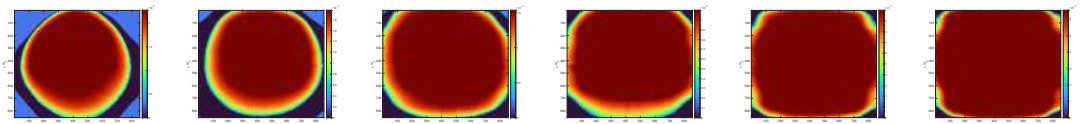
(a)  $100\mu\text{m/s}$ . (b)  $200\mu\text{m/s}$ . (c)  $300\mu\text{m/s}$ . (d)  $400\mu\text{m/s}$ . (e)  $500\mu\text{m/s}$ . (f)  $600\mu\text{m/s}$ .

Figure 5.28: 2D index profile ( $\Delta n$ ) of the waveguides at depth= $50\mu\text{m}$ , energy= $3\mu\text{J}$ , with  $NA=0.40$ .



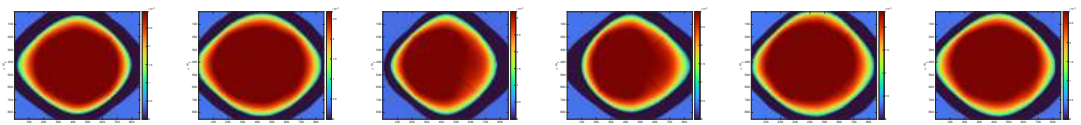
(a)  $100\mu\text{m/s}$ . (b)  $200\mu\text{m/s}$ . (c)  $300\mu\text{m/s}$ . (d)  $400\mu\text{m/s}$ . (e)  $500\mu\text{m/s}$ . (f)  $600\mu\text{m/s}$ .

Figure 5.29: 2D index profile ( $\Delta n$ ) of the waveguides at depth= $150\mu\text{m}$ , energy= $3\mu\text{J}$ , with  $NA=0.40$ .



(a)  $100\mu\text{m/s}$ . (b)  $200\mu\text{m/s}$ . (c)  $300\mu\text{m/s}$ . (d)  $400\mu\text{m/s}$ . (e)  $500\mu\text{m/s}$ . (f)  $600\mu\text{m/s}$ .

Figure 5.30: 2D index profile ( $\Delta n$ ) of the waveguides at depth= $250\mu\text{m}$ , energy= $3\mu\text{J}$ , with  $NA=0.40$ .



(a)  $100\mu\text{m/s}$ . (b)  $200\mu\text{m/s}$ . (c)  $300\mu\text{m/s}$ . (d)  $400\mu\text{m/s}$ . (e)  $500\mu\text{m/s}$ . (f)  $600\mu\text{m/s}$ .

Figure 5.31: 2D index profile ( $\Delta n$ ) of the waveguides at depth= $50\mu\text{m}$ , energy= $2\mu\text{J}$ , with  $NA=0.65$ .

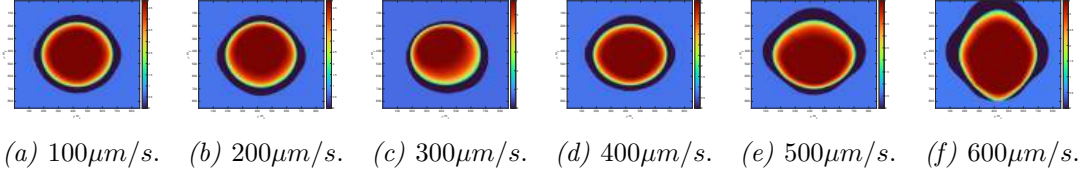


Figure 5.32: 2D index profile ( $\Delta n$ ) of the waveguides at depth= $50\mu\text{m}$ , energy= $3\mu\text{J}$ , with  $NA=0.65$ .

## 5.5 Core-cladding index change calculation using an interferometric sensor

In this study, we utilized a *Single Mode Fiber* (SMF) and a *Multicore Fiber* (MCF) to calculate the refractive index of the core and cladding of the waveguide. The advantage of the MCF lies in its larger core size compared to the SMF.

The tables 5.23 and 5.24 show the results of the measurement of the RI at the core of the buried waveguide. The interferometric techniques are very reliable for the calculation of the RI, because they need only the alignment of the optical sensor device at the position we want to calculate the value. By calculating the refractive index at the core and at the cladding we can obtain the  $\Delta n$ . Due to poor isotropic change of the RI at  $400\mu\text{m}/\text{s}$ ,  $500\mu\text{m}/\text{s}$  and  $600\mu\text{m}/\text{s}$  it was not possible to place the sensor at the core or cladding position with an interference that could allow us to calculate their  $\Delta n$  value. This also limited the calculations to only  $3\mu\text{J}$  at  $50\mu\text{m}$ .

Scan speed [ $\mu\text{m}/\text{s}$ ]	SMF <sub>core</sub>	MCF <sub>core</sub>
100	1.5191	1.5186
200	1.5184	1.5183
300	1.5183	1.5173
400	-	-
500	-	-
600	-	-

Table 5.23: Refractive index of the core obtained with SMF and MCF for  $50\mu\text{m}$  of depth at  $NA=0.40$  and energy= $3\mu\text{J}$ .

From the tables 5.26 and 5.27, it is possible to identify the minimum and maximum value  $\Delta n$ . We can see that the calculations using the MCF fibre are smaller than

Scan speed [ $\mu\text{m/s}$ ]	SMF <sub>core</sub>	MCF <sub>core</sub>
100	1.5205	1.5201
200	1.5203	1.5204
300	1.5212	1.5211
400	1.5195	1.5172
500	1.5204	1.5199
600	1.5206	1.5198

Table 5.24: Refractive index of the core obtained with SMF and MCF for  $50\mu\text{m}$  of depth at  $NA=0.65$  and energy= $3\mu\text{J}$ .

NA	Position (Depth)	RI
0.40	$30\mu\text{m}$	1.5157
	$40\mu\text{m}$	1.5149
0.65	$30\mu\text{m}$	1.5159
	$40\mu\text{m}$	1.5154

Table 5.25: Average refractive index values of the cladding at different positions measured from the location of the buried waveguide.

Scan speed [ $\mu\text{m/s}$ ]	SMF <sub><math>30\mu\text{m}</math></sub>	SMF <sub><math>40\mu\text{m}</math></sub>	MCF <sub><math>30\mu\text{m}</math></sub>	MCF <sub><math>40\mu\text{m}</math></sub>
100	3.366	4.154	2.853	3.642
200	2.695	3.484	2.616	3.405
300	2.537	3.326	1.551	2.340
400	-	-	-	-
500	-	-	-	-
600	-	-	-	-

Table 5.26: Calculated values of the core-cladding change ( $\Delta n$ ) obtained for  $NA=0.40$  at an energy of  $3\mu\text{J}$  and depth of focus  $50\mu\text{m}$  using the interferometric technique with different values of cladding. The values of  $\Delta n$  are on a scale of  $\times 10^{-3}$ .

Scan speed [ $\mu\text{m/s}$ ]	SMF <sub><math>30\mu\text{m}</math></sub>	SMF <sub><math>40\mu\text{m}</math></sub>	MCF <sub><math>30\mu\text{m}</math></sub>	MCF <sub><math>40\mu\text{m}</math></sub>
100	4.592	5.009	4.204	4.621
200	4.463	4.880	4.506	4.923
300	5.368	5.785	5.282	5.699
400	3.600	4.017	1.358	1.775
500	4.549	4.966	3.988	4.405
600	4.765	5.181	3.902	4.319

Table 5.27: Calculated values of the core-cladding change ( $\Delta n$ ) obtained for  $NA=0.65$  at an energy of  $3\mu\text{J}$  and depth of focus  $50\mu\text{m}$  using the interferometric technique with different values of cladding. The values of  $\Delta n$  are on a scale of  $\times 10^{-3}$ .

those obtained by the calculation with the core value of the SMF fibre. This could be because we obtain more light that interferes with the MCF fibre, so there is more information. Hence the values obtained with the MCF fibre could be more precise than those obtained with the SMF fibre. It makes sense that for a material such as a soda-lime substrate, we have values in the range of  $1.55 \times 10^{-3}$  to  $4.2 \times 10^{-3}$  for both NA values.

In Fig. 5.33 the comparison of values for various cladding measurements is illustrated. Notably, at a cladding depth of  $30 \mu m$ , the observed value is lower than that at  $40 \mu m$ . This trend aligns with the expected behavior, as the refractive index contrast ( $\Delta n$ ) increases the distance from the waveguide's core also increases. Consequently, as the cladding is situated farther from the waveguide's core, the values of the index change naturally increase, yet the overall behavioral pattern is consistent throughout the observations.

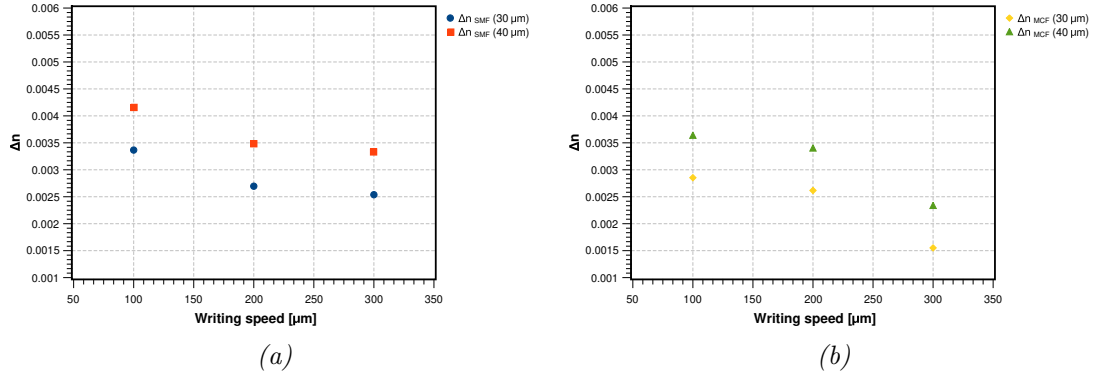


Figure 5.33: Core-cladding index contrast for a  $NA=0.40$  and  $energy=3\mu J$ . Measured by (a) SMF, (b) MCF.

It is worth to note that we have a decreasing behavior for  $NA=0.40$ , but for  $NA=0.65$  it happens only for  $300 - 400 \mu m/s$ , this could be because of the waveguide presented an isotropic change only for those writing speed values.

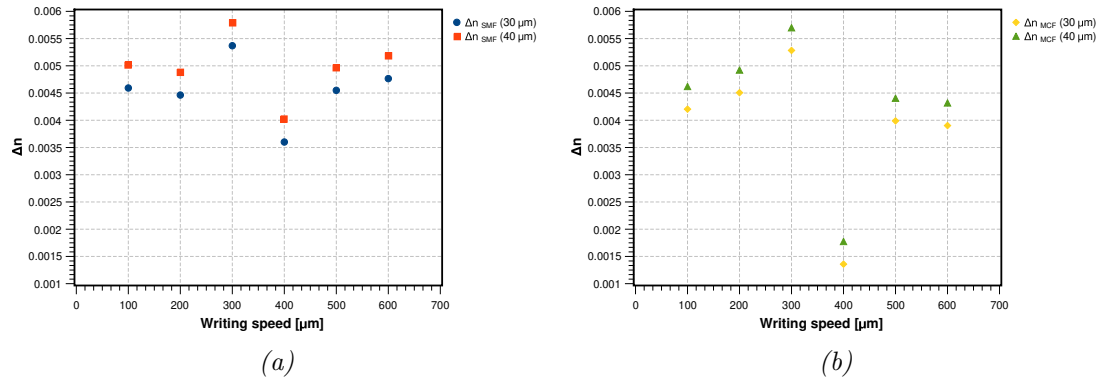


Figure 5.34: Core-cladding index contrast for a  $NA=0.65$  and energy= $3\mu J$ . Measured by (a) SMF, (b) MCF.

## 5.6 Comparing techniques for $\Delta n$ calculation in laser-written waveguides

As we mentioned earlier the calculation of the refractive index determines how light propagates within the waveguide. Accurately knowing the value of  $\Delta n$  is crucial for several reasons:

- *Light confinement and guidance:* Ensures the waveguide supports the desired propagation modes while minimizing losses.
- *Waveguide performance optimization:* Fine-tuning of the optical parameters (NA, mode field diameter, propagation losses) of the waveguide design to optimize performance in photonic devices.
- *Predicting modal behavior:* Guarantees that the waveguide operates under single-mode or multimode conditions, depending on the application requirements.
- *Fabrication quality assessment:* Accurately measuring the refractive index allows for the identification of any deviations or defects in the waveguide structure.
- *Advancing photonic integration:* Precisely characterizing the  $\Delta n$  ensures compatibility and efficiency in optoelectronic integration.

Tables 5.28 and 5.29 show the comparison of the three techniques used for the

calculation of  $\Delta n$  for  $50\mu m$  of depth,  $3\mu J$  with different values of NA (0.40 and 0.65). We can see that the value for the index change increases with the use of a greater NA.

Writing speed [ $\mu m/s$ ]	V parameter	Helmholtz	EFPI
100	4.158	4.147	3.642
200	4.110	1.807	3.405
300	4.077	3.426	2.340
400	4.040	3.054	-
500	3.918	2.604	-
600	3.771	2.084	-

Table 5.28: Comparison of the values of the index contrast ( $\Delta n$ ) for the three techniques at a depth of focus of  $50\mu m$ , with an energy of  $3\mu J$ , and  $NA=0.40$ . Interferometer values for  $MCF_{40\mu m}$ .

Writing speed [ $\mu m/s$ ]	V parameter	Helmholtz	EFPI
100	5.607	5.289	4.621
200	4.831	5.330	4.923
300	5.035	5.534	5.699
400	4.491	5.070	1.775
500	4.379	4.761	4.405
600	5.087	2.366	3.319

Table 5.29: Comparison of the values of the index contrast ( $\Delta n$ ) from three techniques at a depth of focus of  $50\mu m$ , with an energy of  $3\mu J$ , and  $NA=0.65$ . Interferometer values for  $MCF_{40\mu m}$ .

A disadvantage of the Fabry-Pérot technique used to calculate the refractive index of a femtosecond-written waveguide is the punctual value, which depends on where the interferometric sensor is aligned. One advantage of this sensor is the exactitude and sensibility of the measured value.

For the V parameter, we have the disadvantage that the values of the mode field diameter and the core size of the waveguide are needed because we depend on the resolution of the instrument used for these to measure, which is relevant to notice the error that this could introduce into the  $\Delta n$  calculation. An advantage is that we obtain more information during this calculation, and it is faster than the other two techniques because it's a numerical approximation.

Lastly, for the inverse Helmholtz technique, referred here only as Helmholtz, we

have the remarkable outcome of reconstructing the profile. This is essential because, with this, we can have more accurate simulations, enhancing the simulation of the optical device to the actual behavior. A drawback is that we can have less exactitude because of the filter due to the noise.

We can see all the things mentioned above in the tables. Having a closer value for the interferometric technique, then the inverse Helmholtz technique, and finally the V parameter. Even if the normal frequency technique is considered as the one that is far from the value reported for infrared light, it is still correct and can be used for a simulation on an optical device because the change is in  $\times 10^{-3}$  order.

## 5.7 Propagation losses in dielectric waveguides

The propagation loss of a waveguide is defined as the decrease in signal induced by placing the waveguide in the beam path. As light travels down an optical waveguide, energy is lost from the mode through scattering, absorption, and radiation. The spatial properties of the guided modes and core sizes may affect the magnitude of all these processes. Measuring these losses is crucial, as it allows us to analyze the transmission quality of the fabricated buried waveguides and identify optimal configurations based on the analyzed optical factors affecting their performance.

Many waveguide devices created by FDLW are designed to work in conjunction with optical fiber. In this context, it is essential to couple light with minimal losses using similar core sizes, or interestingly, we can match the size of the mode field generated by the optical fiber with the femtosecond generated waveguide by the combination of the refractive index contrast and the core size [5].

Here, we examine the propagation losses of buried waveguides at energy levels of  $2\mu J$  and  $3\mu J$  fabricated at depths of  $50\mu m$ ,  $150\mu m$ , and  $250\mu m$  with different NA=0.40 and NA=0.65.

In Tables 5.30 and 5.31 and Fig. 5.35, for a NA=0.40, we see that the losses increase with the writing speed; this happens because the faster the micromachining platform moves, the less probable it is to create an area with an isotropic RI, so the

best transmission is at  $100\mu m/s$  and the worst at  $600\mu m/s$ . Nevertheless, there are more parameters to consider when defining the optimal fabrication parameters for the optimal waveguide. The loss increases with the depth of the waveguide within the substrate, which means that because of the more elliptical shape-like waveguide, the more losses we had because of the poor confinement of the waveguide, producing a deformed mode. Therefore, we can say that the values of writing speed that generated waveguides with the least losses for a  $NA=0.40$  are at  $50\mu m$  of depth and writing speeds from  $100\mu m/s$  to  $300\mu m/s$ .

Writing speed $\mu m/s$	50 $\mu m$	150 $\mu m$	250 $\mu m$
100	5.482	6.993	9.536
200	5.417	7.442	10.746
300	5.760	9.914	11.557
400	7.731	11.596	14.115
500	7.403	10.317	14.420
600	8.192	12.854	14.025

Table 5.30: Propagation losses ( $\alpha$  [dB/cm]) at an energy level of  $2\mu J$  for a  $NA=0.40$ .

Writing speed $\mu m/s$	50 $\mu m$	150 $\mu m$	250 $\mu m$
100	5.377	6.662	7.168
200	5.287	6.107	8.419
300	5.288	7.136	8.699
400	6.372	8.826	10.217
500	7.450	10.514	11.932
600	10.036	10.801	13.498

Table 5.31: Propagation losses ( $\alpha$  [dB/cm]) at an energy level of  $3\mu J$  for a  $NA=0.40$ .

For Table 5.32 and 5.33 along with the Fig. 5.36, for a  $NA=0.65$ , the behavior of the propagation losses does not follow a path. The highest value occurs at  $200\mu m/s$  and the lowest at  $500\mu m/s$  for  $2\mu J$ , meanwhile for  $3\mu J$  it shows its maximum at  $200\mu m/s$  and the minimum at  $600\mu m/s$ . It is worth considering that the energy focused on the material is higher than the achieved for  $NA=0.40$ , so it is correct to assume that for the slower speed, damage is generated due to the high energy (e.g., microfractures or thermal damage) on the buried waveguides, producing better transmission for the faster speed of fabrication, that is from  $300\mu m/s$  to  $600\mu m/s$  [5].

Writing speed ( $\mu\text{m}/\text{s}$ )	$50 \mu\text{m}$
100	9.561
200	10.161
300	9.821
400	9.096
500	3.329
600	3.689

Table 5.32: Propagation losses ( $\alpha$  [dB/cm]) at  $2\mu\text{J}$  for  $NA=0.65$ .

Writing speed ( $\mu\text{m}/\text{s}$ )	$50 \mu\text{m}$
100	8.150
200	9.501
300	8.140
400	8.031
500	7.903
600	6.553

Table 5.33: Propagation losses ( $\alpha$  [dB/cm]) at  $3\mu\text{J}$  for  $NA=0.65$ .

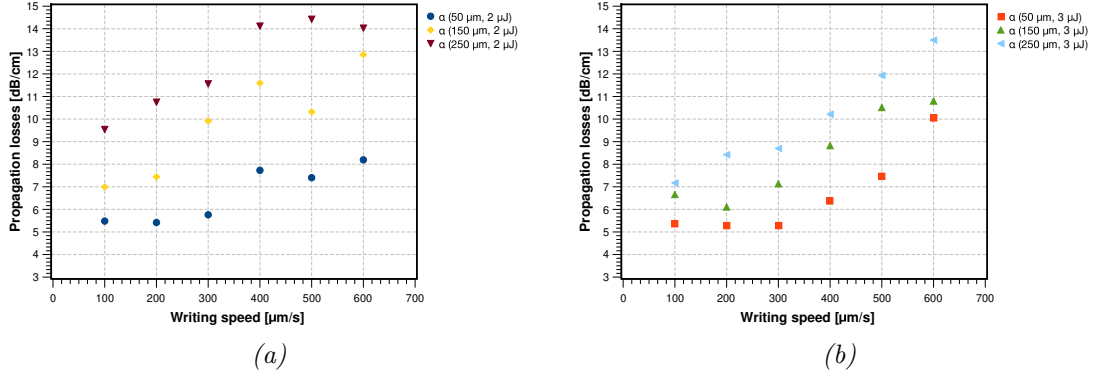


Figure 5.35: Propagation losses ( $\alpha$  [dB/cm]) for different energy levels with  $NA=0.40$ , (a) energy= $2\mu\text{J}$ , (b) energy= $3\mu\text{J}$ .

Based on extensive evaluation of the mode field size, core size, and propagation losses, we can identify the optimal fabrication parameters that result in minimal propagation losses. The following list summarizes the parameters determined for efficient confinement:

- $200\mu\text{m}/\text{s}$  to  $300\mu\text{m}/\text{s}$  at  $2\mu\text{J}$  for  $NA=0.40$ .
- $100\mu\text{m}/\text{s}$  to  $300\mu\text{m}/\text{s}$  at  $3\mu\text{J}$  for  $NA=0.40$ .

## Chapter 5. Results and discussion

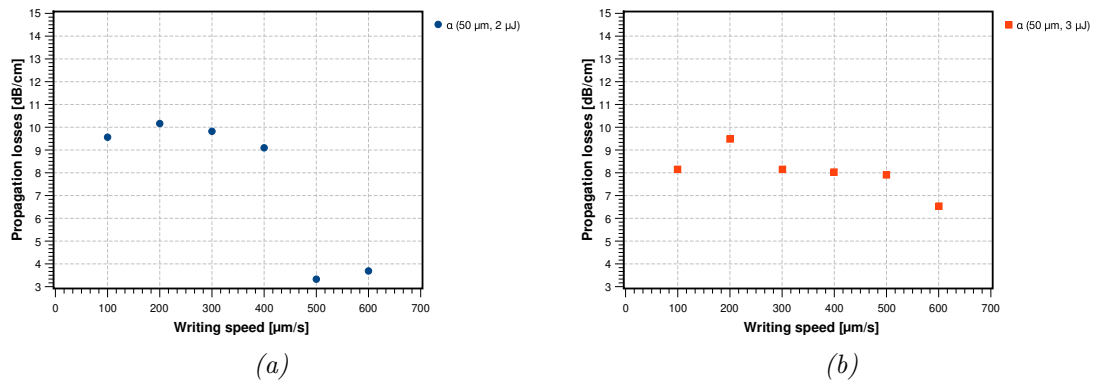


Figure 5.36: Propagation losses ( $\alpha$  [dB/cm]) for different energy levels with  $NA=0.65$ , (a) energy= $2\mu\text{J}$ , (b) energy= $3\mu\text{J}$ .

- $300\mu\text{m/s}$  to  $400\mu\text{m/s}$  at  $2\mu\text{J}$  for  $NA=0.65$ .
- $300\mu\text{m/s}$  at  $3\mu\text{J}$  for  $NA=0.65$ .

*“Scientific knowledge is a body of statements of varying degrees of certainty – some most unsure, some nearly sure, but none absolutely certain.”*

Richard Feynman

# 6

## Conclusions and perspectives

In this concluding chapter, we consolidate the key findings and insights derived from the research conducted in this thesis. The study provides a comprehensive evaluation of calculation techniques for determining the core-cladding refractive index change ( $\Delta n$ ) in buried waveguides fabricated by femtosecond laser techniques on a soda-lime substrate. Additionally, perspectives for future work are proposed.

This work aimed to evaluate and compare three methods for calculating  $\Delta n$  in femtosecond laser-written waveguides. Optimizing the optical parameters of waveguides is critical for enhancing their performance in photonic devices and integrated sensor applications.

The results affirm the effectiveness of the proposed experimental methodology, with calculated  $\Delta n$  values aligning with recent reports in the literature for the infrared region ( $\Delta n = 0.003$  for  $\text{NA} = 0.40$ ). The closest match was obtained using the interferometric

technique with cladding MCF at  $40\ \mu\text{m}$ , highlighting the reliability of the techniques used in this study [8].

The comparative analysis revealed notable differences among the three methods. The inverse Helmholtz method offered the most complete results, reconstructing the refractive index profile with acceptable accuracy. The Fabry-Pérot interferometric technique excelled in providing real-time measurements [47], while the V-parameter method, though less precise, proved to be a practical alternative for rapid estimations.

It is important to emphasize that  $\Delta n$  values are not universally defined but depend on specific setup parameters. The values obtained in this work are consistent with each other, confirming their reliability when compared to previously validated techniques [51].

Each method has unique strengths:

- The V-parameter method can also indicate us whether a waveguide operates in a single-mode regime.
- The inverse Helmholtz technique facilitates visualization of the waveguide profile in two or three dimensions, aiding in understanding index distribution and waveguide homogeneity.
- The Fabry-Pérot interferometric method provides the most precise measurements of  $\Delta n$ .

Ultimately, the choice of technique should align with the specific requirements of the analysis. Employing multiple techniques in tandem could offer a more robust characterization.

Despite the successes achieved, this study faced limitations, including the uniformity of fabricated waveguides, the resolution of instruments for measuring mode field diameter and core diameter, and precise alignment during measurements. Future research should explore hybrid approaches that integrate the strengths of these techniques to address these challenges.

A significant outcome of this work is the generation of  $\Delta n$  data, which can enhance the accuracy of optical device simulations using tools like RSoft software. These find-

ings provide valuable insights into the trade-offs between precision and practicality for  $\Delta n$  characterization, supporting the design of waveguides with tailored properties for sensing and telecommunications applications.

In conclusion, this study contributes to the advancement of waveguide characterization by presenting a detailed evaluation of  $\Delta n$  calculation techniques. The findings pave the way for more efficient and reliable fabrication of photonic devices, marking a significant step forward in the field of integrated optics.

## 6.1 Perspectives

Several key factors are essential for advancing the development and improvement of buried waveguides produced using the FDLW technique:

- Further studies on the optimization of waveguides made by NA=0.65 because of the good quality of the mode field (minimal dispersion).
- Fabricating waveguides closer to the surface to better understand evanescent field interactions and determine the optimal depth of focus.
- Utilizing the data matrix for core-cladding index changes, obtained through the inverse Helmholtz technique, in the simulation of optical devices using RSoft software.
- While this study focused on soda-lime substrates, future research could explore new materials with improved optical properties with higher thermal stability.
- Creation of a friendly-user interface of the code for the V parameter and inverse Helmholtz equation.
- Apply annealing techniques to improve the uniformity of the index change in the waveguides and their geometry.

## Bibliography

- [1] J. X. Zhang and K. Hoshino, *Molecular sensors and nanodevices: principles, designs and applications in biomedical engineering*. Academic Press, 2018.
- [2] K. Sugioka and Y. Cheng, “Femtosecond laser 3d micromachining for microfluidic and optofluidic applications,” 2013.
- [3] M. Beresna, M. Gecevičius, and P. G. Kazansky, “Ultrafast laser direct writing and nanostructuring in transparent materials,” *Advances in Optics and Photonics*, vol. 6, no. 3, pp. 293–339, 2014.
- [4] X. Wang, X. Yu, M. Berg, B. DePaola, H. Shi, P. Chen, L. Xue, X. Chang, and S. Lei, “Nanosecond laser writing of straight and curved waveguides in silicon with shaped beams,” *Journal of Laser Applications*, vol. 32, no. 2, 2020.
- [5] R. R. Gattass and E. Mazur, “Femtosecond laser micromachining in transparent materials,” *Nature photonics*, vol. 2, no. 4, pp. 219–225, 2008.
- [6] Y. Wang, L. Hermann Negri, I. Chiamenti, I. Abe, and H. J. Kalinowski, “Automated system for femtosecond laser writing of photonic structures,” *Journal of Control, Automation and Electrical Systems*, vol. 29, no. 2, pp. 153–162, 2018.
- [7] W.-J. Chen, S. M. Eaton, H. Zhang, and P. R. Herman, “Broadband directional couplers fabricated in bulk glass with high repetition rate femtosecond laser pulses,” *Optics Express*, vol. 16, no. 15, pp. 11 470–11 480, 2008.

## Bibliography

- [8] L. A. Tapia-Licona, J. S. S. Durán-Gómez, E. G. Trejo-Liévano, G. V. Vázquez, R. Ramírez-Alarcón, M. E. Soto-Alcaraz, and R. Castro-Beltrán, “Design and fabrication of Mach–Zehnder interferometers in soda-lime glass for temperature sensing applications,” *Applied Optics*, vol. 62, no. 5, pp. 1214–1220, 2023.
- [9] D. Gailevičius, V. Purlys, L. Maigytė, E. Gaižauskas, M. Peckus, R. Gadonas, and K. Staliūnas, “Femtosecond direct laser writing of photonic spatial filters in soda–lime glass,” *Lithuanian Journal of Physics*, vol. 55, no. 3, 2015.
- [10] S. Xia, S. Huang, C. Yan, N. Ma, and T. Wang, “Refractive index profile measurement of planar optical waveguides based on the near-field technique and digital holography,” *Optical Fiber Technology*, vol. 72, p. 102991, 2022.
- [11] D. Malacara, *Óptica básica*. Fondo de cultura económica, 2015.
- [12] T. Maiman, “Stimulated optical radiation in ruby,” *A Century of Nature: Twenty-One Discoveries that Changed Science and the World*, p. 113, 2010.
- [13] K. M. Davis, K. Miura, N. Sugimoto, and K. Hirao, “Writing waveguides in glass with a femtosecond laser,” *Optics letters*, vol. 21, no. 21, pp. 1729–1731, 1996.
- [14] R. Osellame, G. Cerullo, and R. Ramponi, *Femtosecond laser micromachining: photonic and microfluidic devices in transparent materials*. Springer, 2012, vol. 123.
- [15] “Waveguides,” <https://www.rp-photonics.com/waveguides.html>, accessed: 2023-10-03.
- [16] F. Chen and J. V. de Aldana, “Optical waveguides in crystalline dielectric materials produced by femtosecond-laser micromachining,” *Laser & Photonics Reviews*, vol. 8, no. 2, pp. 251–275, 2014.
- [17] K. Okamoto, *Fundamentals of optical waveguides*. Elsevier, 2021.
- [18] J.-M. Liu, *Photonic devices*. Cambridge University Press, 2009.

## Bibliography

- [19] A. W. Snyder, J. D. Love *et al.*, *Optical waveguide theory*. Chapman and hall London, 1983, vol. 175.
- [20] E. Hecht, *Optics, 5e*. Pearson Education India, 2002.
- [21] G. Lifante, *Integrated photonics: fundamentals*. John Wiley & Sons, 2003.
- [22] E. Snitzer, “Cylindrical dielectric waveguide modes,” *JOSA*, vol. 51, no. 5, pp. 491–498, 1961.
- [23] A. Ghatak and K. Thyagarajan, *An introduction to fiber optics*. Cambridge university press, 1998.
- [24] J. S. S. D. Gómez, “Diseño, fabricación y caracterización de dispositivos integrados para implementación en circuitos fotónicos cuánticos integrados,” 2017.
- [25] J.-F. Bourhis, “Fiber-to-waveguide connection,” in *Glass Integrated Optics and Optical Fiber Devices: A Critical Review*, vol. 10275. SPIE, 1994, pp. 298–329.
- [26] E. M. Segura, “Diseño y fabricación de un dispositivo fotónico integrado para aplicación en comunicaciones,” Master’s thesis, Centro de Investigaciones en Óptica, A.C., 2021.
- [27] E. J. Murphy, “Fiber attachment for guided wave devices,” *Journal of lightwave technology*, vol. 6, no. 6, pp. 862–871, 1988.
- [28] O. G. Ramer, “Single-mode fiber-to-channel waveguide coupling,” *Journal of Optical Communications*, vol. 2, no. 4, pp. 122–127, 1981.
- [29] J. R. Reitz *et al.*, “Fundamentos de la teoría electromagnética,” 1996.
- [30] C. W. Ponader, J. F. Schroeder, and A. M. Streltsov, “Origin of the refractive-index increase in laser-written waveguides in glasses,” *Journal of Applied Physics*, vol. 103, no. 6, p. 063516, 2008.
- [31] D. Nieto García, “Microstructuring of glass by laser irradiation: applications on microoptics and microfluidics.”

## Bibliography

- [32] N. Corporation. (2023) Laser ufab microfabrication workstation. [Online]. Available: [https://www.newport.com/medias/sys\\_master/images/images/h95/h3e/8797295280158/uFAB-Data-Sheet.pdf](https://www.newport.com/medias/sys_master/images/images/h95/h3e/8797295280158/uFAB-Data-Sheet.pdf)
- [33] K. Sugioka and Y. Cheng, “Femtosecond laser three-dimensional micro-and nanofabrication,” *Applied physics reviews*, vol. 1, no. 4, 2014.
- [34] N. Bloembergen, “A brief history of light breakdown,” *Journal of Nonlinear Optical Physics & Materials*, vol. 6, no. 04, pp. 377–385, 1997.
- [35] X. Li, D. R. Ballerini, and W. Shen, “A perspective on paper-based microfluidics: Current status and future trends,” *Biomicrofluidics*, vol. 6, no. 1, 2012.
- [36] P. Banks, B. Stuart, H. Nguyen, and M. Perry, “Femtosecond material processing,” *Commercial and Biomedical Applications of Ultrafast lasers II: 2000*, 2000.
- [37] L. V. Keldysh, “Ionization in the field of a strong electromagnetic wave,” *Zh. Eksperim. i Teor. Fiz.*, vol. 47, 1964.
- [38] A. Shehata, M. Ali, R. Schuch, and T. Mohamed, “Experimental investigations of nonlinear optical properties of soda-lime glasses and theoretical study of self-compression of fs laser pulses,” *Optics & Laser Technology*, vol. 116, pp. 276–283, 2019.
- [39] J. Lonzaga, S. Avanesyan, S. Langford, and J. Dickinson, “Color center formation in soda-lime glass with femtosecond laser pulses,” *Journal of applied physics*, vol. 94, no. 7, pp. 4332–4340, 2003.
- [40] D. Tan, X. Sun, and J. Qiu, “Femtosecond laser writing low-loss waveguides in silica glass: highly symmetrical mode field and mechanism of refractive index change,” *Optical Materials Express*, vol. 11, no. 3, pp. 848–857, 2021.
- [41] Z. Hussain, “Optical band gap, oxidation polarizability, optical basicity and electronegativity measurements of silicate glasses using ellipsometer and abbe refractometer,” *New Journal of Glass and Ceramics*, vol. 11, no. 1, pp. 1–33, 2021.

## Bibliography

- [42] T. P. INC. (2023) Soda lime glass 0215 corning glass slides. [Online]. Available: [https://www.tedpella.com/technote\\_html/0215%20corning%20glass.pdf](https://www.tedpella.com/technote_html/0215%20corning%20glass.pdf)
- [43] edmundoptics. (2023) 20x din achromatic finite intl standard objective. [Online]. Available: <https://www.edmundoptics.eu/p/20x-din-achromactic-finite-intl-standard-objective/3135/>
- [44] D. Marcuse, “Loss analysis of single-mode fiber splices,” *Bell system technical journal*, vol. 56, no. 5, pp. 703–718, 1977.
- [45] I. Mansour and F. Caccavale, “An improved procedure to calculate the refractive index profile from the measured near-field intensity,” *Journal of lightwave technology*, vol. 14, no. 3, pp. 423–428, 1996.
- [46] C. Zhu, H. Zheng, L. Ma, Z. Yao, B. Liu, J. Huang, and Y. Rao, “Advances in fiber-optic extrinsic Fabry-Pérot interferometric physical and mechanical sensors: A review,” *IEEE Sensors Journal*, 2023.
- [47] M. del Carmen Alonso Murias, “Instrumentación de sensores interferométricos de fibra óptica para monitoreo de múltiples parámetros,” 2024.
- [48] Thorlabs, “4-channel fiber-coupled laser source,” 2024, accessed: 2024-11-15. [Online]. Available: <https://www.thorlabs.com/newgrouppage9.cfm?objectgroup-id=3800>
- [49] L. A. Tapia Licona, “Diseño y fabricación de interferómetros Mach-Zehnder mediante la técnica de escritura láser,” Master’s thesis, Centro de Investigaciones en Óptica, A.C., 2021.
- [50] D. Brown. (2023) Tracker video analysis and modeling tool. [Online]. Available: <https://tracker.physlets.org>
- [51] H. Lazcano and G. Vázquez, “Low-repetition rate femtosecond laser writing of optical waveguides in water-white glass slides,” *Applied Optics*, vol. 55, no. 12, pp. 3268–3273, 2016.